Electromagnetic analysis of an ICLPMA with a circular curved iron backplate

Gabrielse, A.J.

Award date:
2007

U/e technische universiteit eindhoven

/ faculteit elektrotechniek

TU/e technische universiteit eindhoven

Capaciteitsgroep Elektrische Energietechniek
Electromechanics & Power Electronics

Master of Science Thesis

Electromagnetic analysis of an ICLPMA with a circular curved iron backplate

A.J. Gabrielse
EPE.2007.A.14

Coaches:

dr. E.A. Lomonova, TU/e
ir. P. Krechting, Tecnotion B.V.

August 20, 2007

/ faculteit elektrotechniek

Electromagnetic analysis of an ICLPMA with a circular curved iron backplate.

Author:	A.J.Gabrielse
Coach TU/e:	Dr. E.A. Lomonova
Coach Tecnotion B.V.:	Ir. P. Krechting

August 20, 2007

Acknowledgements

This thesis concludes the work I have done on the final project to obtain my Master of Science degree. During the final project I have worked at the Technical University of Eindhoven (TU/e) and Tecnotion B.V. in Almelo. The project is performed under authorization of Tecnotion BV. In this acknowledgement I get the chance to thank and describe my appreciation for the effort of all the people who supported me. First of all, I like to thank my direct coach, Dr. E. Lomonova, for her technical support, comments and motivation during the project. Second, I would like to thank my direct coach at Tecnotion B.V., Ir. P. Krechting, for his technical support, comments and introducing me into the world of linear motion. I am very thank-full to him for introducing me to the company Tecnotion B.V. and giving me the chance to become a member of the company.
I am grateful to Prof.Dr.ir. A. Vandenput for his supervision and the opportunity he has given me to graduate at the Electromechanics and Power Electronics group. Further, I would like to thank all the other people who assisted me during this project and supported me mentally and physically. Especially Stephanie for all her love, trust, support and patience during this project and the time when I was too busy writing this thesis. I would like to pay tribute to my parents, who always supported my projects and have encouraged me to keep studying. Their wisdom, understanding and care have enabled me to attain a graduate education. This thesis is dedicated to them.

Contents

1 Introduction **1**
- 1.1 Ironless Actuator . . . 2
- 1.2 Iron core Actuator . . . 2

2 Iron Less Actuator **3**
- 2.1 Commutation . . . 4
- 2.2 Damping . . . 4
- 2.3 Ironless LPMA . . . 5
- 2.4 Analytical Model . . . 6
- 2.5 Magnetic Equivalent Model (MEC). . . . 7
- 2.6 FEM Analysis . . . 13
- 2.7 Conclusion . . . 14

3 Initial ICLPMA-model **17**
- 3.1 Commutation . . . 18
- 3.2 Magnetic Equivalent Circuit . . . 19
  - 3.2.1 Magnetic reluctance . . . 20
  - 3.2.2 Current system . . . 21
  - 3.2.3 Magneto Motive Force (MMF) . . . 22
  - 3.2.4 Solving the MEC model . . . 23
  - 3.2.5 Force calculation . . . 25
  - 3.2.6 Generated emf . . . 26
- 3.3 Conclusion . . . 26

4 FEM Simulations Initial ICLPMA Configuration **27**
- 4.1 FEM calculations . . . 27
- 4.2 Initial cogging force calculation . . . 29
- 4.3 Nominal excitation . . . 32
  - 4.3.1 Nominal Forces . . . 32
  - 4.3.2 Inductances . . . 33
  - 4.3.3 Electro Motive Force (emf) . . . 34
  - 4.3.4 Generated forces . . . 35
  - 4.3.5 Commutation . . . 38
- 4.4 Conclusion . . . 39

5 Geometry Variation of the Stator Back Iron. **41**
5.1 Commutation 41
5.2 Force calculation 42
5.3 Diameter of 7.2 meters 45
5.4 Diameter of 3.6 meters 48
5.5 Diameter of 1.8 meters 50
5.6 Diameter of 0.9 meters 52
5.7 Conclusion 56

6 Analysis of Flux Density Distribution **61**
6.1 Positions of airgap measurements 61
6.2 Flux distribution of the initial model 62
6.3 Flux density distribution of the 7, 2 m diameter model 63
6.4 Flux density distribution of the 3, 6 m diameter model 65
6.5 Flux density distribution of the 1, 8 m diameter model 67
6.6 Flux density distribution of the 0, 9 m diameter model 68
6.7 Conclusion 70

7 Conclusions and recommendations **71**
7.1 Conclusions 71
7.2 Recommendations 72

A Flowchart MEC models. **75**

B ILLPMA Dimensions. **77**

C ICLPMA Dimensions. **79**

D Flux Density Initial Model. **81**
D.1 Initial Model Including End Teeth at Nominal Current. 81
D.2 Initial Model Including End Teeth Without Current. 83
D.3 Initial Model Neglecting End Teeth Without Current. 85

E Flux Density Circular Curved Backplate Models. **87**
E.1 Flux Density 28, 8 m Diameter Model. 87
E.2 Flux Density 7, 2 m Diameter Model. 89
E.3 Flux Density 3, 6 m Diameter Model. 91
E.4 Flux Density 1, 8 m Diameter Model. 93
E.5 Flux Density 0, 9 m Diameter Model. 95

Used Symbols and Abbreviations

Symbols

Quantity	Unit	Description
A	m^2	Surface
b	m	Width
$\overline{B}$, B	T	Magnetic flux density
B_r	T	Remanent magnetic flux density
C_f	deg. electrical/mm	Commutation factor
d	m	Diameter
E	V	Electro motive force
F	N	Force
$\mathcal{F}$	At	Magneto Motive Force, Ampère-turns
g, gap	m	Airgap thickness
h	m	Height
$\overline{H}$, H	A/m	Magnetic field strength
H_c	A/m	Magnet coercivity
I	A	Electric DC current
i	A	Electric AC current
$\overline{J}$, J	A/m^2	Current density
l	m	Length
L	H	Inductance
N	-	Number of turns
r	m	Radius
$\mathcal{R}$	A/(Vs)	Magnetic reluctance
v	m/s	Horizontal speed
V	m^3	Volume
λ	Wb	Coupled flux
τ_{mp}	m	Magnet pitch
τ_{pp}	m	Pole pitch
μ	H/m	Permeability
μ_r	-	Relative permeability
μ_0	$4 \cdot \pi \cdot 10^{-7}$H/m	Permeability of vacuum
Φ	Wb	Flux

Subscripts

Subscript	Description
amp	Peak value of current
Att	Attraction
AV	Average
c	Coil
cu	Copper
emf	Electro motive force
fp	Flux path
g, gap	Airgap
mp	Magnet pitch
pm	Permanent magnet
PP	Peak-Peak
RMS	Root Mean Square
SD	Standard Deviation
x	X-direction
y	Y-direction
z	Z-direction

Acronyms

Acronym	Description
EMF	Electro Motive Force
FEM	Finite Element Method
$ICLPMA$	Iron Core Linear Permanent Magnet Actuator
$ILLPMA$	Iron Less Linear Permanent Magnet Actuator
MEC	Magnetic Equivalent Circuit
MMF	Magneto Motive Force
RMS	Root Mean Square

ILLPMA Dimension Definitions

Name[1]	Definition
bjuk	Width of yoke
bmg	Width of magnet
bsp	Width of coil
dsp	Depth of coil
g	Airgap between magnets
gsp	Airgap between magnet and coil
hjuk	Height of yoke
hmg	Height of magnet
hsp	Height of coil
htnd	Height of teeth
lmg	Length of magnet
lsp	Length of coil
ltnd	Length of teeth

ICLPMA Dimension Definitions

Name[1]	Definition
bgp	Width of backplate
bjuk	Width of yoke
bmg	Width of magnet
btd	Width of teeth
hjuk	Height of yoke
g	Airgap
hgp	Height of backplate
hjuk	Height of yoke
hsp	Height of coil
htnd	Height of teeth
iso	Depth of isolation
ljuk	Length of yoke
slf	Slot width

[1]Names are standard names of Tecnotion B.V.

List of Figures

1.1 Geometry of short stroke ILLPMA 2
1.2 Geometry of long stroke ICLPMA 2

2.1 Exploded view of ILLPMA presented in Fig. 1.1. 5
2.2 BH-curve of the nonlinear steel used in the linear actuators. . . . 5
2.3 Permanent magnet demagnetization curve of the magnets used in the ILLPMA. 6
2.4 Magnetic equivalent model of ILLPMA Fig. 1.1. 7
2.5 Final magnetic equivalent model of ILLPMA (Fig. 1.1). 8
2.6 Area of the airgap reluctance. 9
2.7 Area of the airgap leakage reluctance. 9
2.8 Flux lines in the 2D ILLPMA geometry obtained by 2D FEM . . 10
2.9 Lorentz force over the length of the actuator using the analytical and MEC-model. 12
2.10 Lorentz force over the length of the actuator using the Maxwell 3D FEM software package from Ansoft. Co. 12
2.11 Positions of interest to compare results of the two software packages, 2.11(a) Position 1 and 2.11(b) Position 2 13
2.12 Slice plots of magnetic field density in the ILLPMA at nominal excitation at position 1, obtained by Multiphisics. 14
2.13 Magnetic field density distribution in the ILLPMA at nominal excitation at position 1, obtained by Maxwell 3D. 15

3.1 Disassembled geometry of the initial ICLPMA 17
3.2 Airgap flux change due to the magnets 18
3.3 MEC model ICLPMA 19
3.4 Flux line distribution in the initial ICLPMA obtained by FEM (values are in Weber (Wb)). 19

4.1 Cogging force of initial ICLPMA model, simulated over one period without coil excitation and with discrete steps of 1 mm. . . 29
4.2 Cogging force of initial ICLPMA model, simulated over one period without coil excitation and with discrete steps of 1 mm and 2.5 mm. 30
4.3 Geometry of the initial ICLPMA without end-teeth, used to determine the end effect. 30
4.4 Detent force generated by the initial ICLPMA due to teeth structure of yoke. 31

4.5 Cogging force over one period, considering and neglecting end effects. . . . 32
4.6 Force in direction of travel over one period of the initial ICLPMA model . . . 33
4.7 Coil induction over one period of the initial ICLPMA model . . . 33
4.8 Induced emf over one period of the initial ICLPMA model. . . . 34
4.9 Propulsion force as a function of position and a number of Ampere turns: 4.9(a) 3D plot 4.9(b) 2D plot. . . . 36
4.10 Values of peak-peak force F_{PP} and values of average force ripple F_{SD} at different Ampere turns: 4.10(a) F_{PP} 4.10(b) F_{SD}. . . . 37
4.11 Ratio of propulsion force divided by the current amplitude as a function of current and position. . . . 38
4.12 Propulsion force as a function of φ_c and position. . . . 39

5.1 Starting position and travel direction of the ICLPMA mover. . . 42
5.2 Force directions of the ICLPMA calculated by FEM in cartesian coordinates traveling in a circular motion. . . . 43
5.3 FEM force components and extraction of the force in the direction of travel. . . . 43
5.4 The initial mover on a circular curved backplate with a diameter of $7.2m$, top view. . . . 45
5.5 The initial mover on a circular curved backplate with a diameter of $7.2m$, 3D-view. . . . 45
5.6 Cogging force of the ICLPMA model on a circular curved backplate of 7.2m diameter obtained by FEM. . . . 46
5.7 Nominal force of the ICLPMA model on a circular curved backplate with a diameter of 7.2m obtained by FEM. . . . 47
5.8 Nominal force of the ICLPMA model on a circular curved backplate with a diameter of 28.8m and on the initial backplate obtained by FEM. . . . 47
5.9 The initial mover on a circular curved backplate with a diameter of 3.6m, top view. . . . 48
5.10 The initial mover on a circular curved backplate with a diameter of 3.6m, 3D-view. . . . 48
5.11 Cogging force ICLPMA model on a circular curved backplate of 3.6m diameter obtained by FEM. . . . 49
5.12 Nominal force ICLPMA model on a circular curved backplate of 3.6m diameter. . . . 50
5.13 The initial mover on a circular curved backplate with a diameter of 1.8m, top view. . . . 50
5.14 The initial mover on a circular curved backplate with a diameter of 1.8m, 3D-view. . . . 51
5.15 Cogging force ICLPMA model on a circular curved backplate of 1.8m diameter. . . . 51
5.16 Nominal force ICLPMA model on a circular curved backplate of 1.8m diameter. . . . 52
5.17 The initial mover on a circular curved backplate with a diameter of $0.9m$, top view. . . . 53
5.18 The initial mover on a circular curved backplate with a diameter of $0.9m$, 3D-view. . . . 53

5.19 Cogging force of ICLPMA model on a circular curved backplate of 0.9m diameter. 54
5.20 Nominal force of ICLPMA model on a circular curved backplate of 0.9m diameter. 54
5.21 Cogging force simulation results in function of position and for different diameters of the circular curved backplate and the initial model. 56
5.22 RMS values of the cogging forces for different diameters of the circular curved backplate and the initial model. 57
5.23 Peak-Peak values of the cogging forces for different diameters of the circular curved backplate and the initial model. 57
5.24 Nominal propulsion force as a function of position for different diameters of the circular curved backplate and the initial model in a 2D-view. 58
5.25 Nominal propulsion force as a function of position for different diameters of the circular curved backplate and the initial model in a 3D-view. 59
5.26 Nominal propulsion force as a function of diameter. 59

6.1 Positions of the airgap flux density measurements. 62
6.2 Airgap flux density at both edges of the initial ICLPMA model. . 63
6.3 Airgap flux density at the middle of the initial ICLPMA model. . 63
6.4 Airgap flux density at both edges of the 7, 2 m diameter ICLPMA model. 64
6.5 Airgap flux density at the middle of the mover of the 7, 2 m diameter ICLPMA model. 64
6.6 Airgap flux density at both edges of the 3, 6 m diameter ICLPMA model. 65
6.7 Airgap flux density at the middle of the mover of the 3, 6 m diameter ICLPMA model. 66
6.8 Airgap flux density at both edges of the 1, 8 m diameter ICLPMA model. 67
6.9 Airgap flux density at the middle of the mover of the 1, 8 m diameter ICLPMA model. 67
6.10 Airgap flux density at both edges of the 0, 9 m diameter ICLPMA model. 68
6.11 Airgap flux density at the middle of the mover of the 0, 9 m diameter ICLPMA model. 69
6.12 Airgap flux density at both edges and at the middle of the mover for all diameters and the initial model. 70

A.1 Flowchart of MEC models used to calculate the properties of the ILLPMA and the ICLPMA. 76

B.1 Definition of ILLPMA dimensions, front view. 77
B.2 Definition of ILLPMA dimensions, top view. 78
B.3 Definition of ILLPMA dimensions, side view. 78

C.1 Definition of ICLPMA dimensions, front view. 79
C.2 Definition of ICLPMA dimensions, side view. 80

D.1 Front view of flux density in the initial ICLPMA model at nominal current at starting position. 81
D.2 Side view of flux density in the initial ICLPMA model at nominal current at starting position. 82
D.3 Front view of flux density in the initial ICLPMA model without coil excitation at starting position. 83
D.4 Side view of flux density in the initial ICLPMA model without coil excitation at starting position. 84
D.5 Front view of flux density in the initial ICLPMA model without coil excitation and end teeth at starting position. 85
D.6 Side view of flux density in the initial ICLPMA model without coil excitation and end teeth at starting position. 86

E.1 Front view of flux density in the 28, 8 m diameter ICLPMA model at nominal current at starting position. 87
E.2 Side views of flux density in the 28, 8 m diameter ICLPMA model at nominal current at starting position, Inner edge side E.2(a), Outer edge side E.2(b) 88
E.3 Front view of flux density in the 7, 2 m diameter ICLPMA model at nominal current at starting position. 89
E.4 Side views of flux density in the 7, 2 m diameter ICLPMA model at nominal current at starting position, Inner edge side E.4(a), Outer edge side E.4(b) 90
E.5 Front view of flux density in the 3, 6 m diameter ICLPMA model at nominal current at starting position. 91
E.6 Side views of flux density in the 3, 6 m diameter ICLPMA model at nominal current at starting position, Inner edge side E.6(a), Outer edge side E.6(b) 92
E.7 Front view of flux density in the 1, 8 m diameter ICLPMA model at nominal current at starting position. 93
E.8 Side views of flux density in the 1, 8 m diameter ICLPMA model at nominal current at starting position, Inner edge side E.8(a), Outer edge side E.8(b) 94
E.9 Front view of flux density in the 0, 9 m diameter ICLPMA model at nominal current at starting position. 95
E.10 Side views of flux density in the 0, 9 m diameter ICLPMA model at nominal current at starting position, Inner edge side E.10(a), Outer edge side E.10(b) 96

List of Tables

2.1 Force solution by means of both software packages at different positions 14

4.1 Calculated values for different discrete simulation steps to determine the difference. 30
4.2 Calculated difference between the geometry including end-teeth and the geometry neglecting the end-teeth. 31
4.3 Calculations of generated forces of the initial ICLPMA model at nominal excitation 32
4.4 RMS value of induced emf of the initial ICLPMA model. 35
4.5 Calculated forces of the initial ICLPMA model over one period and for different NI. 35
4.6 F_{RMS} calculation results of propulsion force for different current angles (φ_c) in electrical degrees. 38

5.1 Commutation factors for different diameters of the iron backplate. 41
5.2 Angular position step for the different diameters of the iron backplate 42
5.3 FEM results at different actuator angles for different mover positions, (force values and calculations are in newton (N)). 44
5.4 Comparison of cogging force results of a circular curved backplate with a diameter of $7.2m$ and the backplate of the initial model. . 46
5.5 Comparison of nominal force results of a circular curved backplate with a diameter of $7.2m$ and the backplate of the initial model. . 46
5.6 Comparison of nominal force results of a circular curved backplate with a diameter of 28.8m and the backplate of the initial model. 48
5.7 Comparison of cogging force results of a circular curved backplate with a diameter of 3.6m and the backplate of the initial model. . 49
5.8 Comparison of nominal force results of a circular curved backplate with a diameter of 3.6m and the backplate of the initial model. . 50
5.9 Comparison of cogging force results of a circular curved backplate with a diameter of 1.8m and the backplate of the initial model. . 52
5.10 Comparison of nominal force results of a circular curved backplate with a diameter of 1.8m and the backplate of the initial model. . 52
5.11 Comparison of cogging force results of a circular curved backplate with a diameter of 0.9m and the backplate of the initial model. . 53
5.12 Comparison of nominal force results of a circular curved backplate with a diameter of 0.9m and the backplate of the initial model. . 55

5.13 Comparison of cogging force calculation results for different diameters of the circular curved backplate and the initial model, (values are given in Newton (N)). 56
5.14 Comparison of nominal propulsion force calculation results for different diameters of the circular curved backplate and the initial model, (values are given in Newton (N)). 58

6.1 RMS values of the airgap flux densities of the initial ICLPMA model at starting position. 62
6.2 RMS values of the airgap flux densities of the initial ICLPMA model. 64
6.3 RMS values of the airgap flux densities of the $7,2$ m diameter ICLPMA model. 65
6.4 RMS values of the airgap flux densities of the $3,6$ m diameter ICLPMA model. 66
6.5 RMS values of the airgap flux densities of the $1,8$ m diameter ICLPMA model. 68
6.6 RMS values of the airgap flux densities of the $0,9$ m diameter ICLPMA model. 69

Chapter 1

Introduction

When a conventional or rotary motor is used for a linear movement it requires a mechanical conversion, while a linear actuator directly drives the moving parts. Because of this, the demand for linear actuators increases. Linear actuators can be used without the use of brushes and therefore require less maintenance.

Linear motors can be divided into two types, iron core linear permanent magnet actuator (ICLPMA) and ironless linear permanent magnet actuator (ILLPMA). Both types of actuators usually contain two parts, a moving part-*mover* and a stationary part-*stator*. Where ILLPMAs consist of an air- or epoxy core coils and ICLPMAs consist of coils embedded in iron.
Due to the relatively short presence of the new software package (Multiphysics) for electromagnetic analysis on the market it was necessary to check and identify its applicability in comparison with the well known Maxwell package.
Particularly, the ironless short stroke DC linear actuator is selected as a benchmark for providing the mentioned electromagnetic comparison. There are checked:

- magnetostatic performance,
- position dependent magnetostatic performance.

Afterwards, the main topic of this thesis is discussed, which is dedicated to the research to the physical principles and design aspects of an ICLPMA, which primary involves design changes in the iron backplate of the ICLPMA and the influence of that on the cogging force and nominal force. To compare these influences an initial ICLPMA is analyzed and used as a benchmark for the physical changes that are introduced.

1.1 Ironless Actuator

The ironless actuator used in this chapter consists of an aircore, copper foiled wounded coil inserted in the stator. The geometry of the actuator is presented in Fig. 1.1. Since the stroke of the actuator is limited by the length of the back iron, only one electrical period of the actuator is used for analysis.

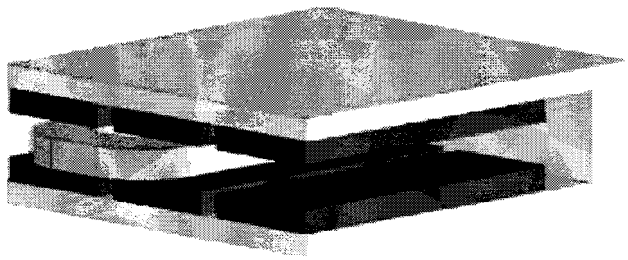

Figure 1.1: Geometry of short stroke ILLPMA

1.2 Iron core Actuator

In this thesis the mover of the iron core actuator consists of a laminated iron yoke with concentrated coils wounded around the teeth. The stationary part consists of an iron backplate (back iron) where magnets are fixed on top of it. The geometry of the ironcore linear permanent magnet actuator (ICLPMA) is presented in Fig. 1.2.

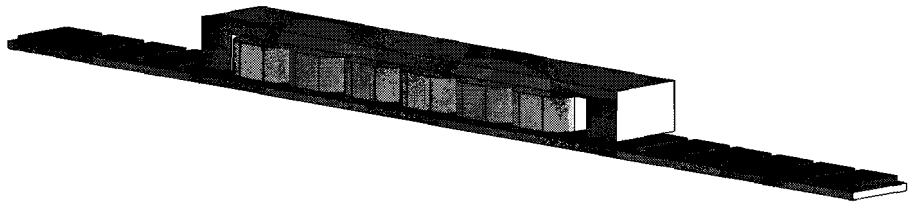

Figure 1.2: Geometry of long stroke ICLPMA

Chapter 2

Iron Less Actuator

Since the Lorentz force generated by the ironless actuators is dependent on the volume of the coil in a magnetic field, high forces demand large volumes. Because no iron is present in the mover part, no non-linear effects are occurring in the actuator (saturation). Fast current changes are therefore possible and high speeds can be reached. Ironless actuators can therefore best be used in processes where low forces and high speeds are necessary. The ILLPMA stand out for their great dynamics and for the fact that they show no cogging or attractive forces between the magnets and the coil. Analyzing the geometry of the ILLPMA to determine its parameters can be done by use of Finite Element Methods (FEM).
There are many different FEM software packages to calculate parameters of a specific model. Two of these software packages are Maxwell (Ansoft Co.) [7] and Multiphysics (Comsol Inc.) [8]. To see the differences between the two mentioned programmes, the 3D model of the introduced ILLPMA is evaluated at different stages and discussed in this chapter. These stages are dedicated to force calculations when the coil is carrying a specific current density at different positions. The material properties and dimensions of the ILLPMA are given by the company, Tecnotion B.V. (See Appendix B).

2.1 Commutation

Because the force in an ironless actuator is determined by the Lorentz force:

$$F(x) = B(x) \cdot I(x) \cdot l, \tag{2.1}$$

and to obtain a maximum constant force along the length of the actuator at all times, the periodic distribution of the magnetic field in the airgap, due to the magnets, is necessary. The Lorentz force is the force which a current conducting coil experiences in a magnetic field. Coupling the magnetic field density to the current as a function of the position of the coil to get the maximum constant force is called the commutation of the actuator. The magnetic field distribution in the airgap is illustrated in Fig. 2.8. According to Lorentz law the current in the coil must be maximum when the magnetic field density is maximum to obtain maximum force, which implies that the current must be shifted by 180 electrical degrees between two magnets and therefore by one magnet pitch (τ_{mp}). If the starting position of the first coil leg is in the middle of a magnet, the current in the coil as a function of the position becomes (2.2):

$$I_{coil} = \pm\hat{I} \cdot \cos\left(\frac{\pi}{\tau_{pp}} \cdot x\right), \tag{2.2}$$

where x is the position and starts at 0 in the middle of a magnet, the $\pm$ sign determines if the coil starting point is between a NS or a SN combination of magnets. We can see that the maximum force is obtained when the distance between the coil legs (w_c) is equal to τ_{mp}, this means an electrical shift of 180 electrical degrees.

2.2 Damping

If the coil moves through the airgap, an electromotive force (emf) is induced according to Faraday's law [10]:

"The electromagnetic induction is the phenomenon of origin of electromotive force (emf) in a conductor or coil by magnetic flux changes and in a conductor by cutting magnetic force lines,"

and is mathematically described by:

$$E_{emf} = -B \cdot l_c \cdot v, \tag{2.3}$$

where l_c is the effective length of the conductor or coil in the flux density field, in this case the length of the magnet, v is the speed at which the conductor or coil travels in the magnetic field. The minus sign is introduced because the sense of the induced emf is always so that it resists the cause of its origin. The generated electromotive force is called back emf. If there are no conducting currents in the coil and the coil is traveling at speed v the induced back emf induces so called eddy currents due to the resistance of the coil windings. These eddy currents will cause a damping force due to the Lorentz law.

2.3 Ironless LPMA

The 3D geometry of the ILLPMA model which is used to determine the differences between the software packages, is presented in Fig. 1.1 and a disassembled view of the ILLPMA is presented in Fig. 2.1 to show the components, of which it consists, more specifically. It consists of an U-shaped armature, or yoke, with

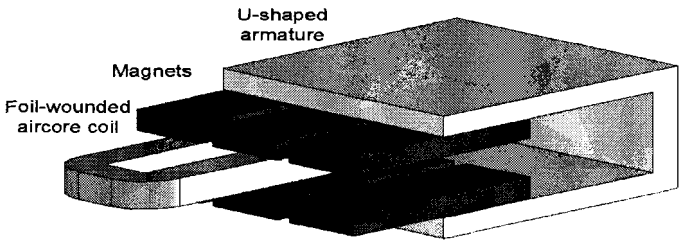

Figure 2.1: Exploded view of ILLPMA presented in Fig. 1.1.

permanent magnets having a remanent flux density of $B_r = 1.4$T, glued on both sides as a stationary part. A copper-aircore foil-wounded coil placed between the double-sided stator presents a moving part.
The non-linear steel yoke where the permanent magnets are glued on, can withstand the attraction forces between two opposite magnets and has a BH-curve as presented in Fig. 2.2.

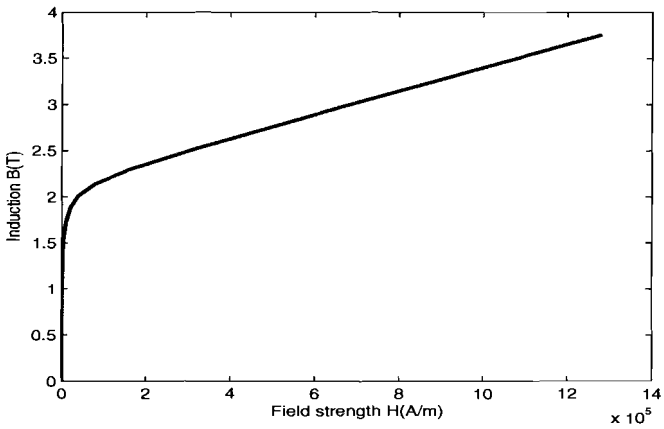

Figure 2.2: BH-curve of the nonlinear steel used in the linear actuators.

2.4 Analytical Model

The demagnetization curve of the magnets, Fig. 2.3, is assumed linear and can be described by:

$$B_m = \left(\frac{H_m}{H_c} + 1\right) \cdot B_r. \tag{2.4}$$

With $H_c = \frac{B_r}{\mu_{pm}}$ where $\mu_{pm} = \mu_0 \cdot \mu_r$, (2.4) becomes:

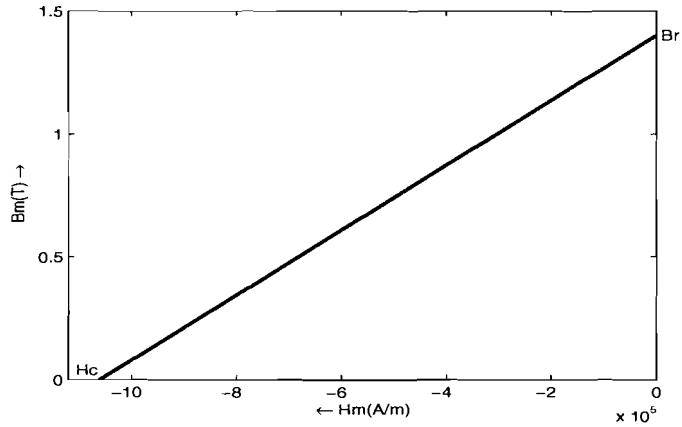

Figure 2.3: Permanent magnet demagnetization curve of the magnets used in the ILLPMA.

$$B_m = B_r + H_m \cdot \mu_0 \cdot \mu_r. \tag{2.5}$$

If there is no flux leakage, then $\phi_m = \phi_g$ and:

$$B_g \cdot A_g = B_m \cdot A_m. \tag{2.6}$$

From Ampère's law:

$$\oint_C \vec{H}\, d\vec{l} = I_{enclosed} = NI, \tag{2.7}$$

can be derived:

$$H_g \cdot g = -H_m \cdot h_m, \tag{2.8}$$

where,

H_g	airgap field strength,
H_m	magnet field strength,
g	airgap,
h_m	magnet height.

Combining (2.5),(2.6) and (2.8) and using $B_g = \mu_0 \cdot H_g$, the flux density in the airgap becomes:

$$\hat{B}_g = \frac{B_r}{\frac{A_g}{A_m} + \frac{\mu_{pm} \cdot g}{h_m}}. \tag{2.9}$$

The flux density in the air gap as a function of position can be described as:

$$B_g = \hat{B}_g \cos\left(\frac{\pi}{\tau_{mp}}\, x\right). \tag{2.10}$$

The forces are produced by Lorentz forces according to (2.1) Combining (2.10) and (2.1) we obtain:

$$F_{coil} = \hat{B}_g\, I_c\, l_c \left(\cos\left(\frac{\pi}{\tau_{mp}}\, (x + w_c)\right) - \cos\left(\frac{\pi}{\tau_{mp}}\, x\right)\right), \tag{2.11}$$

where I_c is the current in the coil and l_c is the effective length of the coil in the flux density field. The force is generated in the two coil legs. The flux density at the position of the second coil leg is described by (2.10), where position x is shifted over the coil width w_c. Calculating the generated Lorentz force (2.11) when the coil is moved with discrete steps of $1mm$ over the length of the actuator results in Fig. 2.9.

2.5 Magnetic Equivalent Model (MEC).

To interpret the ILLPMA analytically, the magnetic circuit is ,,converted" to an electrical circuit. Such a model is called a Magnetic Equivalent Circuit model (MEC-model). The MEC-model of the ILLPMA is shown in Fig. 2.4.

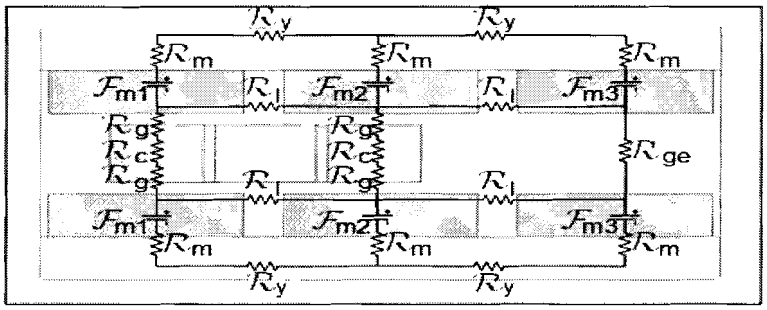

Figure 2.4: Magnetic equivalent model of ILLPMA Fig. 1.1.

The reluctances in the Fig. 2.4 are:

- $\mathcal{R}_m$ - magnet reluctance,
- $\mathcal{R}_y$ - iron reluctance,
- $\mathcal{R}_l$ - leakage reluctance,
- $\mathcal{R}_c$ - coil reluctance,
- $\mathcal{R}_g$ - airgap reluctance between coil and magnet,
- $\mathcal{R}_{ge}$ - airgap reluctance when no coil is present.

The coil is an air-core foil-wounded with a filling factor (K_f) of 0.9. The relative permeability of copper is, $\mu_r = 0.9999$. Since $\mu_r \approx \mu_0$ the flux reluctance in the airgap is treated the same over the entire length of the actuator. The MEC-model from Fig. 2.4 then becomes as illustrated in Fig. 2.5.

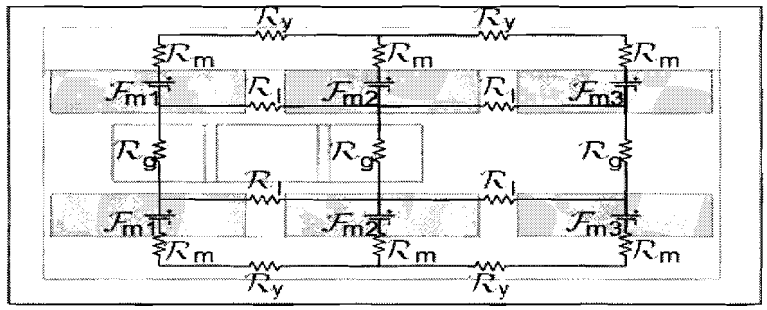

Figure 2.5: Final magnetic equivalent model of ILLPMA (Fig. 1.1).

The general expression for a reluctance of a circuit component is:

$$\mathcal{R} = \frac{l_{fp}}{\mu \cdot A_{fp}}, \tag{2.12}$$

where l_{fp} is the length of the flux path and A_{fp} is the area where the flux is present. The reluctance of the yoke is obtained by (2.12) where l_{fp} is the distance between two magnets and is described by the magnet pitch. A_{fp} is described by the area which conducts the flux and because the most flux will travel between the magnets, the area is described over the length of a magnet and the height of the yoke. μ is calculated by an iterative procedure (See Appendix A) using the interpolated BH-curve. A new value of the permeability is calculated every iteration step and used to recalculate the yoke reluctance. The new permeability of the iron is obtained by:

$$\mu_{new} = \frac{B_{iron}}{\mu_0 \cdot H_{iron}}, \tag{2.13}$$

where B_{iron} is the flux density in the iron and H_{iron} is the magnetic field strength which is obtained from the flux density and the interpolated BH-curve. The reluctance of the iron becomes:

$$\mathcal{R}_y = \frac{\tau_{mp}}{\mu_{new} \cdot y_h \cdot l_m}, \tag{2.14}$$

where y_h is the height of the back iron and l_m is the length of the magnet. The airgap reluctance R_g is obtained by (2.12), where l_{fp} is the airgap length and A_{fp} the area of a magnet. The area used for calculation of the airgap reluctance is illustrated in Fig. 2.6 Although there will be some fringing and leakage of the flux in the airgap (area $A2$ in Fig. 2.6), this is neglected due to the minor influence of it. The airgap reluctance becomes:

$$\mathcal{R}_g = \frac{g}{\mu_0 \cdot w_m \cdot l_m}, \tag{2.15}$$

where w_m is the width of a magnet. The leakage reluctance between two neighboring magnets can be seen in Fig. 2.7. Since the flux will follow a path with the lowest reluctance the maximum leakage path will be the same as the airgap length. The maximum radius (r) will become:

$$r = \frac{g - (\tau_{mp} - w_m)}{\pi}. \tag{2.16}$$

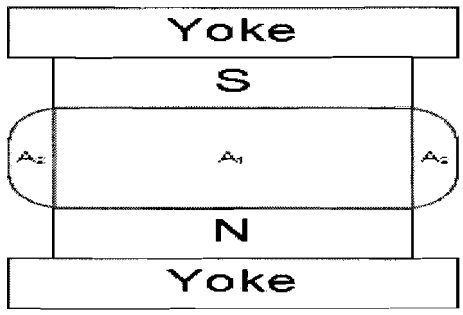

Figure 2.6: Area of the airgap reluctance.

The leakage reluctance becomes:

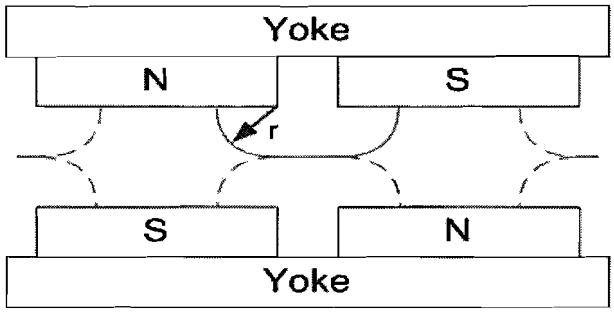

Figure 2.7: Area of the airgap leakage reluctance.

$$\mathcal{R}_l = \left(\frac{\mu_0 \cdot l_m}{\pi} \cdot \ln\left(1 + \frac{\pi \cdot r}{\tau_{mp} - w_m + 2 \cdot r}\right)\right)^{-1}. \tag{2.17}$$

The demagnetization curve Fig. 2.3 and described by (2.5) can be represented as a MMF source F in combination with a reluctance (R_m). The general expression for the source can be described by:

$$\mathcal{F}_m = H_c \cdot h_m, \tag{2.18}$$

where H_c is the magnetic coercivity of the magnet and F_m the MMF over the magnet. The reluctance R_m is described by:

$$\mathcal{R}_m = \frac{h_m}{\mu_m \cdot \mu_0 \cdot w_m \cdot l_m}, \tag{2.19}$$

Since the relation between the MMF source, the reluctance and the flux in a component in the MEC-model can be described as:

$$\mathcal{F}_i = \mathcal{R}_i \cdot \phi_i, \tag{2.20}$$

where R_i is the reluctance of the component, ϕ_i the flux in the component and F_i the MMF over the component. The MMF source over a magnet can then be described as:

$$\mathcal{F}_m = \mathcal{R}_m \cdot \phi_m. \tag{2.21}$$

The MMF sources of the magnets as function of position of the coil in the airgap can be described as:

$$\begin{aligned} \mathcal{F}_{m_1} &= \hat{\Phi}_m \cdot \cos\left(\tfrac{\pi}{\tau_{mp}} \cdot x\right) \cdot \mathcal{R}_m, \\ \mathcal{F}_{m_2} &= \hat{\Phi}_m \cdot \cos\left(\tfrac{\pi}{\tau_{mp}} \cdot (x + \tau_{mp})\right) \cdot \mathcal{R}_m, \\ \mathcal{F}_{m_3} &= \hat{\Phi}_m \cdot \cos\left(\tfrac{\pi}{\tau_{mp}} \cdot x\right) \cdot \mathcal{R}_m. \end{aligned} \tag{2.22}$$

Where $\hat{\Phi}_m$ is the maximum flux calculated by $B_{rm} \cdot A_{magnet}$. To validate these assumptions a 2D-model of the ILLPMA is analyzed by 2D FEM using Maxwell 2D. The flux lines in the geometry of the ILLPMA obtained by FEM are illustrated in Fig. 2.8. It can be seen that the assumptions are correct.

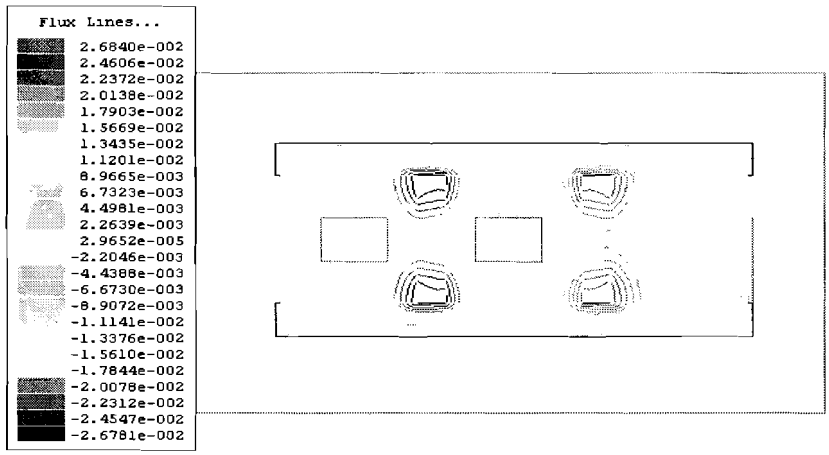

Figure 2.8: Flux lines in the 2D ILLPMA geometry obtained by 2D FEM

The circuit equations can be derived from the model Fig. 2.5 and written in the matrix form [9]:

$$[\mathbf{f}] = [\mathbf{A}] \cdot [\mathbf{\Phi}], \tag{2.23}$$

where,

$$\mathbf{f} = \begin{bmatrix} 0 \\ 0 \\ 0 \\ 0 \\ 0 \\ 0 \\ 0 \\ \mathcal{F}_{m_2}(x) - \mathcal{F}_{m_1}(x) \\ \mathcal{F}_{m_3}(x) - \mathcal{F}_{m_2}(x) \\ 0 \\ 0 \\ \mathcal{F}_{m_2}(x) - \mathcal{F}_{m_1}(x) \\ \mathcal{F}_{m_3}(x) - \mathcal{F}_{m_2}(x) \end{bmatrix} \quad \mathbf{\Phi} = \begin{bmatrix} \Phi_{m_1} \\ \Phi_{m_2} \\ \Phi_{m_3} \\ \Phi_{m_4} \\ \Phi_{m_5} \\ \Phi_{m_6} \\ \Phi_{g_1} \\ \Phi_{g_2} \\ \Phi_{g_3} \\ \Phi_{l_1} \\ \Phi_{l_2} \\ \Phi_{l_3} \\ \Phi_{l_4} \end{bmatrix} \tag{2.24}$$

and,

$$\mathbf{A} = \begin{bmatrix} 1 & 1 & 1 & 0 & 0 & 0 & 0 & 0 & 0 & 0 & 0 & 0 & 0 \\ -1 & 0 & 0 & 0 & 0 & 0 & 1 & 0 & 0 & -1 & 0 & 0 & 0 \\ 0 & -1 & 0 & 0 & 0 & 0 & 0 & 1 & 0 & 1 & 1 & 0 & 0 \\ 0 & 0 & -1 & 0 & 0 & 0 & 0 & 0 & 1 & 0 & -1 & 0 & 0 \\ 0 & 0 & 0 & 1 & 0 & 0 & -1 & 0 & 0 & 0 & 0 & -1 & 0 \\ 0 & 0 & 0 & 0 & 1 & 0 & 0 & -1 & 0 & 0 & 0 & 1 & 1 \\ 0 & 0 & 0 & 0 & 0 & 1 & 0 & 0 & -1 & 0 & 0 & 0 & -1 \\ -\mathcal{R}_y & \mathcal{R}_m & 0 & 0 & 0 & 0 & 0 & 0 & 0 & \mathcal{R}_l & 0 & 0 & 0 \\ 0 & -\mathcal{R}_m & \mathcal{R}_y & 0 & 0 & 0 & 0 & 0 & 0 & 0 & -\mathcal{R}_l & 0 & 0 \\ 0 & 0 & 0 & 0 & 0 & 0 & -\mathcal{R}_g & \mathcal{R}_g & 0 & -\mathcal{R}_l & 0 & \mathcal{R}_l & 0 \\ 0 & 0 & 0 & 0 & 0 & 0 & 0 & -\mathcal{R}_g & \mathcal{R}_g & 0 & \mathcal{R}_l & 0 & -\mathcal{R}_l \\ 0 & 0 & 0 & -\mathcal{R}_y & \mathcal{R}_m & 0 & 0 & 0 & 0 & 0 & 0 & -\mathcal{R}_l & 0 \\ 0 & 0 & 0 & 0 & -\mathcal{R}_m & \mathcal{R}_y & 0 & 0 & 0 & 0 & 0 & 0 & \mathcal{R}_l \end{bmatrix}. \tag{2.25}$$

Solving the equations for $\mathbf{\Phi}$ defines the fluxes in all the components. The flux densities in the coil are derived from the flux in the air gap with:

$$B = \frac{\Phi_{g_n}(x)}{A_m}, \tag{2.26}$$

where Φ_{g_n} is the flux in the airgap at the position of a coil leg and A_m the area of the magnet. The Lorentz force applied on the coil, due to the magnetic field B in the air gap, is calculated by Lorentz law (2.1).
If there is no coil current and the coil is moving at a speed v through the airgap, a force is induced called damping force, and caused by the the generation of eddy currents in the coil and Lorentz law. The damping force is calculated by:

$$F(x) = B^2(x) \cdot \sigma_{copper} \cdot l_c \cdot V_{coil} \cdot K_f, \tag{2.27}$$

where σ_{copper} is the conductivity of copper, V_{coil} the volume of the coil and K_f the filling factor.

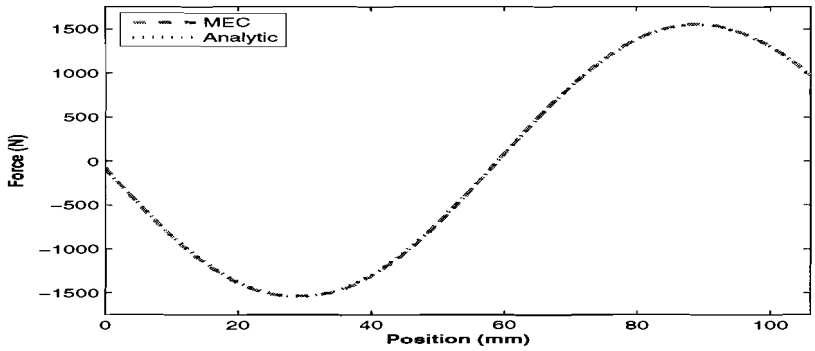

Figure 2.9: Lorentz force over the length of the actuator using the analytical and MEC-model.

Calculating the Lorentz force using the „analytical" and MEC-model over the total length of the actuator with steps of $1mm$ results in Fig. 2.9. It can be concluded that the iron- and magnet reluctance have no influence on the generated force and is caused by the relatively large airgap reluctance in comparison with the magnet and iron reluctance. The model is inserted in the Maxwell 3D FEM software package from Ansoft. Co. and the force on the coil is analyzed over the same length as with the MEC model. The result is depicted in Fig. 2.10. Since

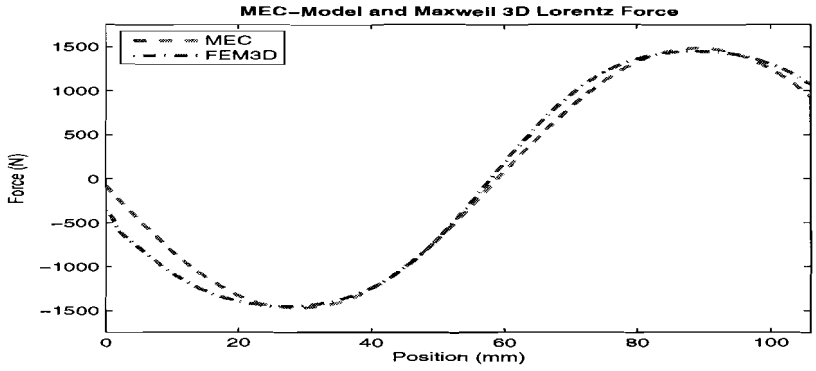

Figure 2.10: Lorentz force over the length of the actuator using the Maxwell 3D FEM software package from Ansoft. Co.

the MEC model calculates the generated Lorentz force at the middle of a coil leg, it doesn't consider the width of the coil and the fact that some windings already cut field lines at certain positions. This causes the difference between the MEC model and the FEM analysis in Fig. 2.10.

2.6 FEM Analysis

The model is again analyzed in the FEM software package Multiphysics from Comsol Inc. This package is the new version of formal software package Femlab. To analyze magnetostatic problems it is often necessary to use a non-linear solver for the non-linear magnetostatic materials used in a model. Comsol Multiphysics includes one non-linear solver which gives problems when the BH-curve is implemented and is caused by the zero initial conditions at the start of the analysis. To avoid this problem it is necessary to obtain a linear solution of the model first. The non-linear solver creates an initial value from this solution. In Maxwell 3D it is easy to analyze the generated force over the length of the actuator using parametric analysis by inserting a variabel for the position of the coil in the airgap and let it increase after each step of analysis. In Comsol Multiphysics it is not possible to introduce dimensions as variables and therefore it is not possible to do the same analysis unless the coil is moved at each position manually and resolve the problem. Since initially there were two positions of interest, the problem is solved at these two positions. The positions of interest are depicted in Fig. 2.11. Comsol Multiphysics calculates the vector quantities

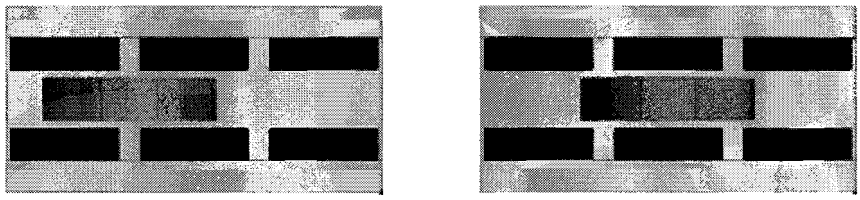

(a) (b)

Figure 2.11: Positions of interest to compare results of the two software packages, 2.11(a) Position 1 and 2.11(b) Position 2

for the magnetic flux density in the entire geometry. This vector matrix can be used in the calculator, in which the force on the coil can be calculated by:

$$F_{coil} = \int_{V_{coil}} \vec{J} \times \vec{B}\, dV \tag{2.28}$$

From the vector matrix the magnetic flux density in the geometry can be generated. In Multiphysics it is possible to display the field in slices, the number of slices can be chosen manually. In this case, two plots of the magnetic flux density are generated with 3 slices in the x-direction and with 3 slices in the y-direction at position 1. These plots are illustrated in Fig. 2.12. The magnetic field density calculated in the ILLPMA model at position 1 by Maxwell 3D is illustrated in Fig. 2.13. Both software packages show a maximum field density of 2 Tesla, which means that the iron is at the end of the linear region according to the BH-curve, presented in Fig. 2.2. This is mainly caused by the high remanent flux density (B_r = 1.4T) of the magnets which are attached to it. Numerical results of the software packages are given in Table. 2.1. The force is calculated in the direction of travel.

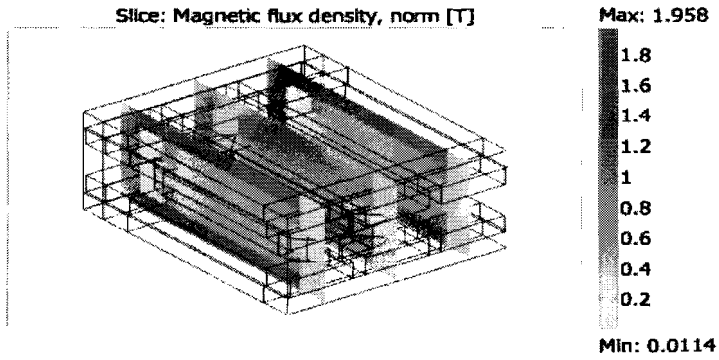

(a) Slices in x-direction

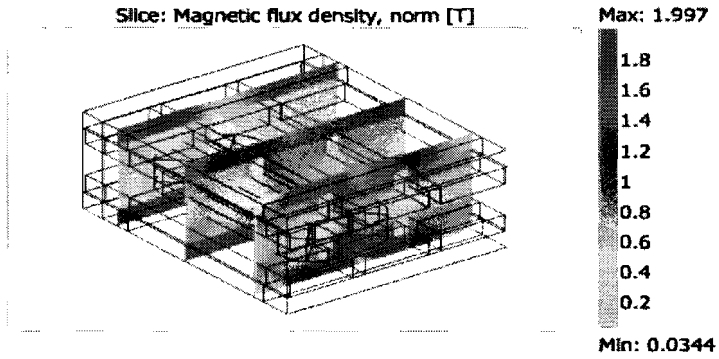

(b) Slices in y-direction

Figure 2.12: Slice plots of magnetic field density in the ILLPMA at nominal excitation at position 1, obtained by Multiphisics.

Table 2.1: Force solution by means of both software packages at different positions

Calculation	Position 1	Position 2
$F_{Maxwell3D}$	-1438 N	$0,28$ N
$F_{Multiphisics}$	-1440 N	0 N

2.7 Conclusion

From the results obtained by the MEC model and the two FEM software packages, it can be concluded that the differences in results are minor. The main difference between the two software packages is the user interface. It can be

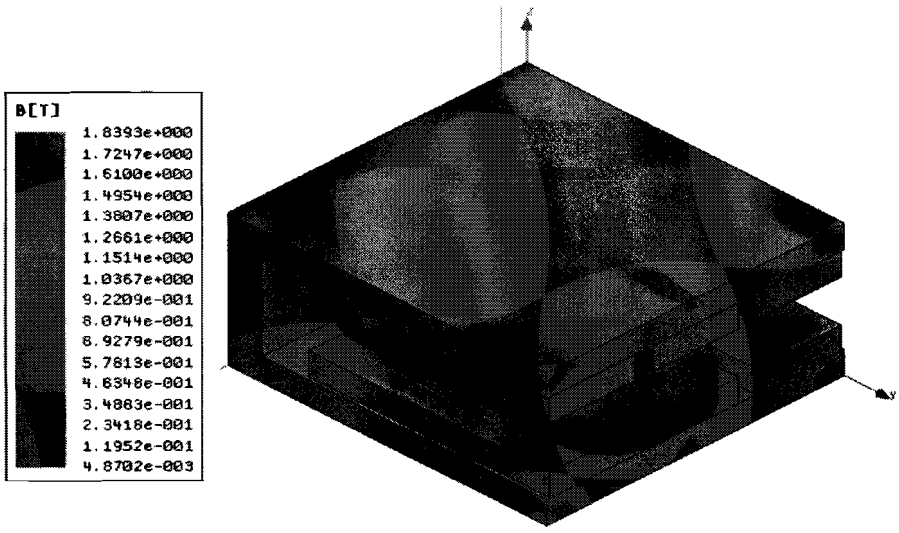

Figure 2.13: Magnetic field density distribution in the ILLPMA at nominal excitation at position 1, obtained by Maxwell 3D.

clearly seen that Maxwell 3D is built only to analyze electromagnetic related problems, where Comsol Multiphysics is build to analyze multiple physical related problems (electrical, chemical, etc.). Due to this it is easier to obtain an electrical solution in Maxwell 3D then in Comsol Multiphysics. During the simulations of the ILLPMA it became clear that the non-linear solver of Maxwell 3D is more powerful than the non-linear solver of Comsol Multiphysics. This due to te fact that Maxwell 3D can generate an initial value and Comsol Multiphysics did not. The conclusion is therefore that it is much easier to analyze a 3D geometry with Maxwell 3D than with Comsol Multiphysics. But, because of the difference in prices, the recommendation for companies with low R&D budget, goes to Comsol Multiphysics.

Chapter 3

Initial ICLPMA-model

Iron core actuators have a higher flux density than the ironless actuators, which results in a higher efficiency and weight. Therefore a higher force can be generated in a smaller volume. A disadvantage of the ICLPMA is the hysteresis effect of the iron. An increase of speed demands higher currents to run the hysteresis loop faster. These high currents will introduce an increase of temperature which can cause damage to the coils. Therefore the ICLPMA can best be used in processes where high forces, low volume and low speeds are necessary. In this chapter an analytical model of the, in this project used, ICLPMA is studied on its properties. These properties are compared with the initial properties which will be obtained by FEM in later chapters, where the mover is analyzed on different geometries of the iron backplate. The geometry of the initially used ICLPMA is presented in Fig. 1.2 and is based on a standard ICLPMA-model of Tecnotion B.V. (See Appendix C). To give a more specific view of the actuator and the components of which it consists, a disassembled view of the actuator components is presented in Fig. 3.1. It consists of an iron backplate where the

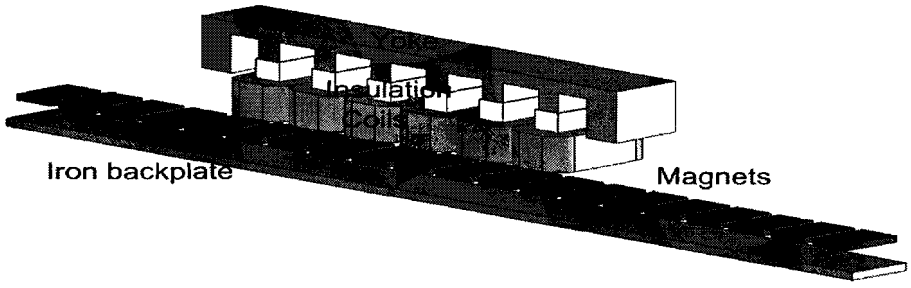

Figure 3.1: Disassembled geometry of the initial ICLPMA

magnets are glued on, with a magnet pitch (τ_{mp}) of 25mm. The yoke consists of six coils which are wound around a teeth covert with an insulation material and a pole pitch (τ_{pp}) of 33,333mm. The six coils are connected to a 3-phase system with on every phase two coils in series. They are attached in the following sequence: $RSTRST$, where R, S and T are the electrical phases. To determine the properties analytically, a MEC model is used to calculate the flux densities

in this geometry. After this, the model is tested using FEM analyses and compared with the MEC model. The exact measurements of the actuator can be found in the Appendix.

3.1 Commutation

To obtain maximum force in the direction of travel, the currents in the coils of the ICLPMA must be excited in a certain manner, called commutation. The definition of the commutation is dependent on the geometry of the actuator and can be defined by the force equation:

$$F = I \cdot \frac{d\phi}{dx}, \tag{3.1}$$

where I is the coil current and $\frac{d\phi}{dx}$ the flux difference in the direction of travel. To obtain maximum force at all times, the current has to be at its peak value when the flux change is maximum. The flux change is maximum between two magnets so the current must be at its peak value at the same point. In Fig. 3.2 one period of the flux change in the airgap due to the magnets is illustrated. Since it is a cosine waveform, the derivative of it will be a sine wave shifted over 180°. Since the current must be at its peak value between two magnets, the

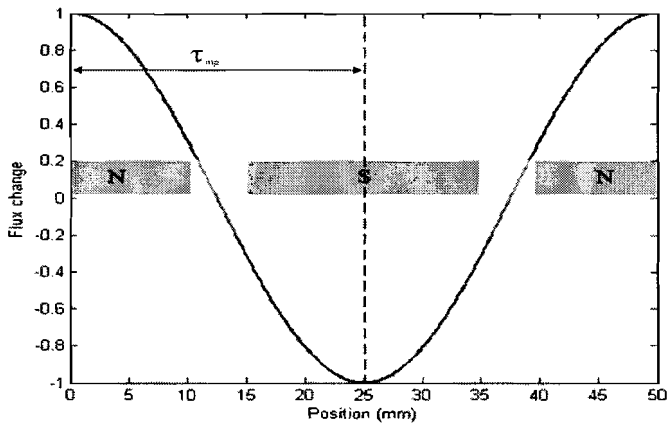

Figure 3.2: Airgap flux change due to the magnets

current must be maximum in opposite direction between the next two magnets to gain maximum force in the same direction. Therefore, the current must be shifted over one magnet pitch by 180 electrical degrees. Since in these case the magnet pitch is $25mm$, the current changes:

$$\frac{\pi}{\tau_{mp}} = 7,2\frac{^{\circ}}{mm}. \tag{3.2}$$

This is called the commutation factor of the ICLPMA and is given in electrical degrees per mm. It must be taken into account that the actual flux change in the airgap is not sinusoidal but more trapezoidal.

3.2 Magnetic Equivalent Circuit

The magnetic circuit is converted to an electric circuit by means of Fig. 3.3. The initial position in these calculations is established while the teeth of the R-phase is at the middle of a south pole magnet.

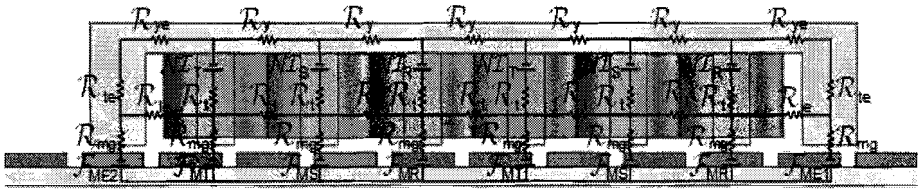

Figure 3.3: MEC model ICLPMA

Where,

$\mathcal{R}_{ye}$	-	Iron reluctance between an end tooth and an active tooth,
$\mathcal{R}_{y}$	-	Iron reluctance between two active teeth,
$\mathcal{R}_{te}$	-	Iron reluctance of an end tooth,
$\mathcal{R}_{t}$	-	Iron reluctance of an active tooth,
$\mathcal{R}_{le}$	-	Leakage reluctance between an end tooth and an active tooth,
$\mathcal{R}_{l}$	-	Leakage reluctance between two active teeth,
$\mathcal{R}_{g}$	-	Reluctance between a active tooth and the iron backplate,
$\mathcal{R}_{ge}$	-	Reluctance between a end tooth and the iron backplate,
$\mathcal{NI}_{n}$	-	Magneto motive force of active tooth n,
$\mathcal{F}_{ME_n}$	-	Magneto motive force of a magnet at position of end tooth n,
$\mathcal{F}_{M_n}$	-	Magneto motive force of a magnet at position of active tooth n.

The flux path distribution at the starting position is obtained by FEM and illustrated in Fig. 3.4.

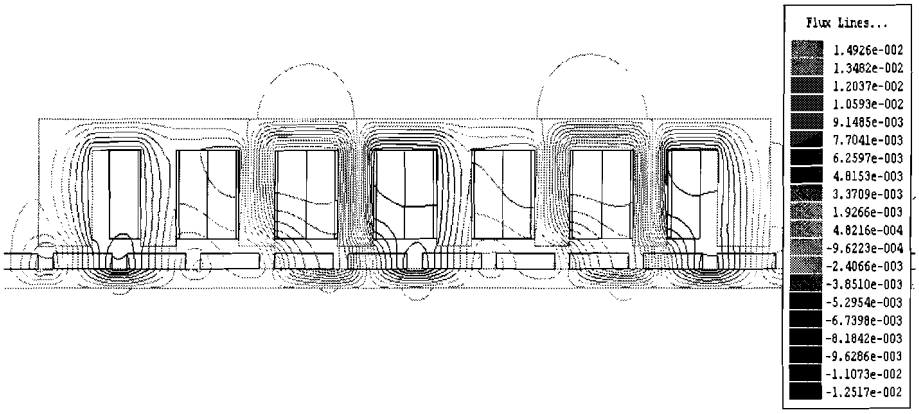

Figure 3.4: Flux line distribution in the initial ICLPMA obtained by FEM (values are in Weber (Wb)).

3.2.1 Magnetic reluctance

The magnetic reluctances in the electrical circuit in Fig. 3.3 are calculated by the general expression [1]:

$$\mathcal{R} = \frac{l_{fp}}{\mu_r \cdot A_{fp}}, \tag{3.3}$$

where l_{fp} is the length of the flux path and A_{fp} is the area where the flux is present. μ_r is the remanent permeability of the used material.
The airgap reluctance between a tooth (R_g) and the iron backplate can be expressed, by use of (3.3), as:

$$\mathcal{R}_g = \frac{KC \cdot \left(g + \frac{h_{mg}}{\mu_{rm}}\right)}{\mu_0 \cdot l_{mg} \cdot btd}, \tag{3.4}$$

where,

KC	Carter's factor,
g	airgap height,
h_{mg}	height of the magnets,
μ_{rm}	relative permeability of the magnets,
μ_0	magnetic permeability of vacuum,
l_{mg}	length of the magnets,
btd	tooth width.

The Carter's factor in this equation takes into account that the average flux path over the airgap is longer caused by the variable airgap shape. The variable airgap shape is caused by the slotted structure of the yoke. The leakage resistances in the circuit are obtained by:

$$\mathcal{R}_l = \frac{2 \cdot (2 \cdot slf)}{\mu_0 \cdot \mu_{cu} htnd \cdot bjuk}, \tag{3.5}$$

where,

slf	slot width,
μ_{cu}	relative permeability of copper,
$htnd$	height of the tooth,
$bjuk$	Yoke depth (stack length).

The magnetic reluctance is multiplied by 2 to take into account that the flux leakage will increase from zero at the yoke to maximum at the airgap. Since the tooth reluctance is variable in a function of position, due to the non-linear iron, the relative permeability of the iron is obtained by iterations, recalculating and with use of the BH-curve of the iron. The BH-curve of the non-linear iron is presented in Fig. 2.2. The new μ_{rm} is obtained by calculating the flux density in the tooth. The flux density in the tooth will introduce a field strength which is obtained by the interpolated BH-curve. The new permeability becomes:

$$\mu_{fe_{new}} = \frac{B_{tooth}}{\mu_0 \cdot H_{tooth}}, \tag{3.6}$$

A number of iterations provides a regular actual relative permeability of the iron at a certain position. The algorithm used to calculate the new permeability is

presented in the Appendix. The tooth reluctance is calculated by:

$$\mathcal{R}_t = \frac{2 \cdot htnd}{3 \cdot \mu_0 \cdot \mu_{fe} \dot{b}td \cdot bjuk}, \tag{3.7}$$

where the $\frac{2}{3}$ factor takes into account that the lower part of the tooth is not saturated due to leakage fluxes that enter the tooth over the hole height. The reluctance of the yoke iron is calculated in the same manner as the tooth reluctance and becomes:

$$\mathcal{R}_y = \frac{2 \cdot slf}{(hjuk - htnd) \cdot \mu_{fe} \cdot bjuk}, \tag{3.8}$$

where $hjuk$ is the height of the yoke. The two reluctances in series in the end teeth becomes:

$$\mathcal{R}_v = \mathcal{R}_t + \mathcal{R}_y. \tag{3.9}$$

3.2.2 Current system

The currents in a function of position can be described in the same manner as (3.11) with the difference that instead of τ_{pp} the position variable x (mm) is used. The 3-phase current system in a function of a position x then becomes:

$$\begin{aligned} i_R &= \hat{i} \cdot \sin\left(\tfrac{\pi}{\tau_{mp}} \cdot x\right), \\ i_S &= \hat{i} \cdot \sin\left(\left(\tfrac{\pi}{\tau_{mp}} \cdot x\right) - 240\right), \\ i_T &= \hat{i} \cdot \sin\left(\left(\tfrac{\pi}{\tau_{mp}} \cdot x\right) - 120\right), \end{aligned} \tag{3.10}$$

where $\hat{i}$ is the maximum value of the current and described by $\hat{i} = \sqrt{2} \cdot i$. The phase shift of 240 electrical degrees is calculated using the pole pitch (τ_{pp}) and (5.1) and becomes:

$$\varphi = \tau_{pp} \cdot \frac{\pi}{\tau_{mp}}, \tag{3.11}$$

Because the „coil" sources in the MEC model can be described by the Ampere turns of each coil due to (2.7), each source is described by the product of the current and the number of turns of the coil. The 3-phase Ampere turns system in function of position x then becomes,

$$\begin{aligned} \mathcal{NI}_R &= N \cdot \hat{i} \cdot \sin\left(\tfrac{\pi}{\tau_{mp}} \cdot x\right), \\ \mathcal{NI}_S &= N \cdot \hat{i} \cdot \sin\left(\left(\tfrac{\pi}{\tau_{mp}} \cdot x\right) - 240\right), \\ \mathcal{NI}_T &= N \cdot \hat{i} \cdot \sin\left(\left(\tfrac{\pi}{\tau_{mp}} \cdot x\right) - 120\right), \end{aligned} \tag{3.12}$$

where N is the number of turns of a coil.

3.2.3 Magneto Motive Force (MMF)

The Magneto Motive Force (MMF) of the magnets can be described in the same manner as used by the ILLPMA. Therefore, the MMF in a function of position x can be described by a sinusoidal function. Because it is necessary to obtain the MMF value at the position on the teeth of the yoke, the MMF system for the active teeth can be described with the same phase shifts as the currents. The end teeth also conducts the MMF of the magnet below it. The phase shift for these teeth is described by the distance between the R-phase tooth and the end teeth. The MMF source system for the MEC model in a function of position becomes:

$$\begin{aligned}
\mathcal{F}_{M_R} &= -\hat{\Phi}_{pm} \cdot \cos\left(\tfrac{\pi}{\tau_{mp}} \cdot x\right) \cdot \mathcal{R}_{mg}, \\
\mathcal{F}_{M_S} &= -\hat{\Phi}_{pm} \cdot \cos\left(\left(\tfrac{\pi}{\tau_{mp}} \cdot x\right) - 240\right) \cdot \mathcal{R}_{mg}, \\
\mathcal{F}_{M_T} &= -\hat{\Phi}_{pm} \cdot \cos\left(\left(\tfrac{\pi}{\tau_{mp}} \cdot x\right) - 120\right) \cdot \mathcal{R}_{mg}, \\
\mathcal{F}_{M_{E1}} &= -\hat{\Phi}_{pm} \cdot \cos\left(\left(\tfrac{\pi}{\tau_{mp}} \cdot x\right) - 228\right) \cdot \mathcal{R}_{mg}, \\
\mathcal{F}_{M_{E2}} &= -\hat{\Phi}_{pm} \cdot \cos\left(\left(\tfrac{\pi}{\tau_{mp}} \cdot x\right) - 708\right) \cdot \mathcal{R}_{mg},
\end{aligned} \tag{3.13}$$

where $\hat{\Phi}_{pm}$ is the maximum flux the magnet can supply and is calculated with,

$$\hat{\Phi}_{pm} = B_r \cdot \frac{lmg \cdot btd \cdot hmg}{hmg + \mu_r \cdot g}. \tag{3.14}$$

The phase shift of the MMF at position of the end teeth is calculated using (3.11) where τ_{pp} is replaced by the distance between the middle of the first R-phase tooth and the middle of the end tooth. The $(-)$ sign takes into account that the starting position is above a S-pole magnet.

3.2.4 Solving the MEC model

To calculate the flux densities in the actuator, the circuit of the MEC model (Fig. 3.3) has to be solved for each value of x. In this case, the actuator is analyzed over one period. This means a 50 mm shift and it is done by 50 positions shifted by 1 mm. The circuit can be be described by the matrix function [9]:

$$[\mathbf{f}] = [\mathbf{A}] \cdot [\mathbf{\Phi}], \tag{3.15}$$

where $[\mathbf{f}]$ and $[\mathbf{\Phi}]$ is described by:

$$[\mathbf{f}] = \begin{bmatrix} 0 \\ 0 \\ 0 \\ 0 \\ 0 \\ 0 \\ 0 \\ 0 \\ 0 \\ 0 \\ 0 \\ 0 \\ 0 \\ -\mathcal{NI}_R \\ \mathcal{NI}_S - \mathcal{NI}_R \\ \mathcal{NI}_T - \mathcal{NI}_S \\ \mathcal{NI}_R - \mathcal{NI}_T \\ \mathcal{NI}_S - \mathcal{NI}_R \\ \mathcal{NI}_T - \mathcal{NI}_S \\ -\mathcal{NI}_T \\ \mathcal{F}_{M_R} - \mathcal{F}_{M_{E1}} \\ \mathcal{F}_{M_S} - \mathcal{F}_{M_R} \\ \mathcal{F}_{M_T} - \mathcal{F}_{M_S} \\ \mathcal{F}_{M_R} - \mathcal{F}_{M_T} \\ \mathcal{F}_{M_S} - \mathcal{F}_{M_R} \\ \mathcal{F}_{M_T} - \mathcal{F}_{M_S} \\ \mathcal{F}_{M_{E2}} - \mathcal{F}_{M_T} \end{bmatrix} \quad [\mathbf{\Phi}] = \begin{bmatrix} \Phi_{R1} \\ \Phi_{S1} \\ \Phi_{T1} \\ \Phi_{R2} \\ \Phi_{S2} \\ \Phi_{T2} \\ \Phi_{E1} \\ \Phi_{E2} \\ \Phi_{m_{R1}} \\ \Phi_{m_{S1}} \\ \Phi_{m_{T1}} \\ \Phi_{m_{R2}} \\ \Phi_{m_{S2}} \\ \Phi_{m_{T2}} \\ \Phi_{m_{E1}} \\ \Phi_{m_{E2}} \\ \Phi_{y_1} \\ \Phi_{y_2} \\ \Phi_{y_3} \\ \Phi_{y_4} \\ \Phi_{y_5} \\ \Phi_{l_1} \\ \Phi_{l_2} \\ \Phi_{l_3} \\ \Phi_{l_4} \\ \Phi_{l_5} \\ \Phi_{l_6} \\ \Phi_{l_7} \end{bmatrix}, \tag{3.16}$$

and the matrix **A** contains the variables of the Kirchhoff's equations,

$$[\mathbf{A}] = \begin{bmatrix}
1 & 0 & 0 & 0 & 0 & 0 & 1 & 0 & 0 & 0 & 0 & 0 & 0 & 0 & 0 & 0 & -1 & 0 & 0 & 0 & 0 & 0 & 0 & 0 & 0 & 0 & 0 & 0 \\
0 & 1 & 0 & 0 & 0 & 0 & 0 & 0 & 0 & 0 & 0 & 0 & 0 & 0 & 0 & 0 & 1 & -1 & 0 & 0 & 0 & 0 & 0 & 0 & 0 & 0 & 0 & 0 \\
0 & 0 & 1 & 0 & 0 & 0 & 0 & 0 & 0 & 0 & 0 & 0 & 0 & 0 & 0 & 0 & 0 & 1 & -1 & 0 & 0 & 0 & 0 & 0 & 0 & 0 & 0 & 0 \\
0 & 0 & 0 & 1 & 0 & 0 & 0 & 0 & 0 & 0 & 0 & 0 & 0 & 0 & 0 & 0 & 0 & 0 & 1 & -1 & 0 & 0 & 0 & 0 & 0 & 0 & 0 & 0 \\
0 & 0 & 0 & 0 & 1 & 0 & 0 & 0 & 0 & 0 & 0 & 0 & 0 & 0 & 0 & 0 & 0 & 0 & 0 & 1 & -1 & 0 & 0 & 0 & 0 & 0 & 0 & 0 \\
0 & 0 & 0 & 0 & 0 & 1 & 0 & 1 & 0 & 0 & 0 & 0 & 0 & 0 & 0 & 0 & 0 & 0 & 0 & 0 & 1 & 0 & 0 & 0 & 0 & 0 & 0 & 0 \\
0 & 0 & 0 & 0 & 0 & 0 & 1 & 0 & 0 & 0 & 0 & 0 & 0 & 0 & 1 & 0 & 0 & 0 & 0 & 0 & 0 & 1 & 0 & 0 & 0 & 0 & 0 & 0 \\
-1 & 0 & 0 & 0 & 0 & 0 & 0 & 0 & 1 & 0 & 0 & 0 & 0 & 0 & 0 & 0 & 0 & 0 & 0 & 0 & 0 & -1 & -1 & 0 & 0 & 0 & 0 & 0 \\
0 & -1 & 0 & 0 & 0 & 0 & 0 & 0 & 0 & 1 & 0 & 0 & 0 & 0 & 0 & 0 & 0 & 0 & 0 & 0 & 0 & 0 & 1 & -1 & 0 & 0 & 0 & 0 \\
0 & 0 & -1 & 0 & 0 & 0 & 0 & 0 & 0 & 0 & 1 & 0 & 0 & 0 & 0 & 0 & 0 & 0 & 0 & 0 & 0 & 0 & 0 & 1 & -1 & 0 & 0 & 0 \\
0 & 0 & 0 & -1 & 0 & 0 & 0 & 0 & 0 & 0 & 0 & 1 & 0 & 0 & 0 & 0 & 0 & 0 & 0 & 0 & 0 & 0 & 0 & 0 & 1 & -1 & 0 & 0 \\
0 & 0 & 0 & 0 & -1 & 0 & 0 & 0 & 0 & 0 & 0 & 0 & 1 & 0 & 0 & 0 & 0 & 0 & 0 & 0 & 0 & 0 & 0 & 0 & 0 & 1 & -1 & 0 \\
0 & 0 & 0 & 0 & 0 & -1 & 0 & 0 & 0 & 0 & 0 & 0 & 0 & 1 & 0 & 0 & 0 & 0 & 0 & 0 & 0 & 0 & 0 & 0 & 0 & 0 & 1 & -1 \\
0 & 0 & 0 & 0 & 0 & 0 & 0 & 1 & 0 & 0 & 0 & 0 & 0 & 0 & 0 & 1 & 0 & 0 & 0 & 0 & 0 & 0 & 0 & 0 & 0 & 0 & 0 & 1 \\
\mathcal{R}_t & 0 & 0 & 0 & 0 & 0 & \mathcal{R}_v & 0 & 0 & 0 & 0 & 0 & 0 & 0 & 0 & 0 & 0 & 0 & 0 & 0 & 0 & -\mathcal{R}_l & 0 & 0 & 0 & 0 & 0 & 0 \\
-\mathcal{R}_t & \mathcal{R}_t & 0 & 0 & 0 & 0 & 0 & 0 & 0 & 0 & 0 & 0 & 0 & 0 & 0 & 0 & -\mathcal{R}_y & 0 & 0 & 0 & 0 & 0 & \mathcal{R}_l & 0 & 0 & 0 & 0 & 0 \\
0 & -\mathcal{R}_t & \mathcal{R}_t & 0 & 0 & 0 & 0 & 0 & 0 & 0 & 0 & 0 & 0 & 0 & 0 & 0 & 0 & -\mathcal{R}_y & 0 & 0 & 0 & 0 & 0 & \mathcal{R}_l & 0 & 0 & 0 & 0 \\
0 & 0 & -\mathcal{R}_t & \mathcal{R}_t & 0 & 0 & 0 & 0 & 0 & 0 & 0 & 0 & 0 & 0 & 0 & 0 & 0 & 0 & -\mathcal{R}_y & 0 & 0 & 0 & 0 & 0 & \mathcal{R}_l & 0 & 0 & 0 \\
0 & 0 & 0 & -\mathcal{R}_t & \mathcal{R}_t & 0 & 0 & 0 & 0 & 0 & 0 & 0 & 0 & 0 & 0 & 0 & 0 & 0 & 0 & -\mathcal{R}_y & 0 & 0 & 0 & 0 & 0 & \mathcal{R}_l & 0 & 0 \\
0 & 0 & 0 & 0 & -\mathcal{R}_t & \mathcal{R}_t & 0 & 0 & 0 & 0 & 0 & 0 & 0 & 0 & 0 & 0 & 0 & 0 & 0 & 0 & -\mathcal{R}_y & 0 & 0 & 0 & 0 & 0 & \mathcal{R}_l & 0 \\
0 & 0 & 0 & 0 & 0 & -\mathcal{R}_t & 0 & -\mathcal{R}_v & 0 & 0 & 0 & 0 & 0 & 0 & 0 & 0 & 0 & 0 & 0 & 0 & 0 & 0 & 0 & 0 & 0 & 0 & 0 & \mathcal{R}_l \\
0 & 0 & 0 & 0 & 0 & 0 & 0 & 0 & \mathcal{R}_g & 0 & 0 & 0 & 0 & 0 & -\mathcal{R}_g & 0 & 0 & 0 & 0 & 0 & 0 & \mathcal{R}_l & 0 & 0 & 0 & 0 & 0 & 0 \\
0 & 0 & 0 & 0 & 0 & 0 & 0 & 0 & -\mathcal{R}_g & \mathcal{R}_g & 0 & 0 & 0 & 0 & 0 & 0 & 0 & 0 & 0 & 0 & 0 & 0 & -\mathcal{R}_l & 0 & 0 & 0 & 0 & 0 \\
0 & 0 & 0 & 0 & 0 & 0 & 0 & 0 & 0 & -\mathcal{R}_g & \mathcal{R}_g & 0 & 0 & 0 & 0 & 0 & 0 & 0 & 0 & 0 & 0 & 0 & 0 & -\mathcal{R}_l & 0 & 0 & 0 & 0 \\
0 & 0 & 0 & 0 & 0 & 0 & 0 & 0 & 0 & 0 & -\mathcal{R}_g & \mathcal{R}_g & 0 & 0 & 0 & 0 & 0 & 0 & 0 & 0 & 0 & 0 & 0 & 0 & -\mathcal{R}_l & 0 & 0 & 0 \\
0 & 0 & 0 & 0 & 0 & 0 & 0 & 0 & 0 & 0 & 0 & -\mathcal{R}_g & \mathcal{R}_g & 0 & 0 & 0 & 0 & 0 & 0 & 0 & 0 & 0 & 0 & 0 & 0 & -\mathcal{R}_l & 0 & 0 \\
0 & 0 & 0 & 0 & 0 & 0 & 0 & 0 & 0 & 0 & 0 & 0 & -\mathcal{R}_g & \mathcal{R}_g & 0 & 0 & 0 & 0 & 0 & 0 & 0 & 0 & 0 & 0 & 0 & 0 & -\mathcal{R}_l & 0 \\
0 & 0 & 0 & 0 & 0 & 0 & 0 & 0 & 0 & 0 & 0 & 0 & 0 & -\mathcal{R}_g & 0 & \mathcal{R}_g & 0 & 0 & 0 & 0 & 0 & 0 & 0 & 0 & 0 & 0 & 0 & -\mathcal{R}_l
\end{bmatrix}. \quad (3.17)$$

From the two known matrices, [**f**] and [**A**], the flux matrix [**Φ**] can be derived and used to define the flux densities in all the components of the actuator. When the flux is known, the flux density inside a certain material is derived by:

$$B_{mat} = \frac{\phi_{mat}}{A_{mat}}, \tag{3.18}$$

where ϕ_{mat} is the flux through the certain material and A_{mat} the area of the material where the flux is traveling through. When the flux densities in the different parts of the iron are known, the field strengths are derived by means of the interpolated BH-curve and used to calculate the new permeability of the iron. This procedure repeated several iterations to obtain a stable permeability. The algorithm used is the same as used with the ILLPMA and is presented in the Appendix.

3.2.5 Force calculation

The force generated by the actuator in the direction of travel (x-direction) is calculated using (3.1), where $d\phi$ is the flux linkage change inside an active tooth and I the coil current at the moment of the flux change. The total force generated by the actuator can be described by:

$$\begin{aligned} F_R(x) &= i_R(x) \cdot \left(\frac{d\phi_{R_a}}{dx} + \frac{d\phi_{R_b}}{dx} \right), \\ F_S(x) &= i_S(x) \cdot \left(\frac{d\phi_{S_a}}{dx} + \frac{d\phi_{S_b}}{dx} \right), \\ F_T(x) &= i_T(x) \cdot \left(\frac{d\phi_{T_a}}{dx} + \frac{d\phi_{T_b}}{dx} \right), \end{aligned} \tag{3.19}$$

where the subscripts a and b describe the two coils of one phase. Since the currents and the flux change are in a function of position x. The total propulsion force (F_x) in a function of position x becomes:

$$F_x(x) = F_R(x) + F_S(x) + F_T(x). \tag{3.20}$$

The propulsion force obtained by the MEC model becomes:

Force	Value
F_x	464, 28 N

3.2.6 Generated emf

The mover will introduce an emf when it travels. The emf is calculated by the general expression:

$$E_i = -\frac{d\lambda_i}{dt}. \tag{3.21}$$

The 3-phase emf is calculated by:

$$\begin{aligned} E_R &= -\left(\frac{d\lambda_{R_a}}{dt} + \frac{d\lambda_{R_b}}{dt}\right), \\ E_S &= -\left(\frac{d\lambda_{S_a}}{dt} + \frac{d\lambda_{S_b}}{dt}\right), \\ E_T &= -\left(\frac{d\lambda_{T_a}}{dt} + \frac{d\lambda_{T_b}}{dt}\right), \end{aligned} \tag{3.22}$$

where λ_i is the flux linkage of coil i and calculated by the general expression:

$$\lambda_i = N \cdot \phi_i \tag{3.23}$$

The emf obtained by the MEC model becomes:

emf	Value
E_R	$23,68$ V
E_S	$22,52$ V
E_T	$20,12$ V

3.3 Conclusion

This MEC model is capable in fast calculations of the properties of the ICLPMA taking into account the non-linearity of the used iron and the end effects of the mover. It must be taken into account that the MEC model defines the flux path in the middle of each teeth, where the actual flux path changes over the width of the teeth as the mover changes position. The airgap reluctance is treated the same over the entire period of the actuator and does not take into account that it changes as the teeth move from one magnet to the next. Therefore, a recommendation for future investigation will be a more precise description for the airgap reluctances.

Chapter 4

FEM Simulations Initial ICLPMA Configuration

The initial model, described in the introduction and chapter 3, is analyzed with FEM for different values of the coil currents, varying from the linear region to saturation of the yoke. Including zero current to gain the cogging force of the actuator. The FEM analysis is done using the Maxwell 3D software package from Ansoft Co. From the results of these simulations different parameters of the initial model will be calculated and discussed. This chapter concludes the fundamental issues of this research because it provides the benchmark for the electromagnetic analysis. All simulations are analyzed over one period of the actuator. This period is a distance of $50mm$ and starts with the R-phase tooth exactly above the middle of a S-pole magnet. From this point, discrete steps of $2,5mm$ are taken until the R-phase tooth is exactly above the next S-pole magnet.

4.1 FEM calculations

Since FEM analysis is a numerical calculation, it will introduce numerical errors in the results. These errors must be taken into account when the results are evaluated. The first question that rises is how accurate the results are. Since the results contain numerical values, some calculations are done to reveil the accuracy of the result. For the cogging force this is done by calculating the average over one period. Since, theoretically, the average has to be zero, calculation of the average value will give a good estimation of the accuracy. The average value of the results is calculated by:

$$\bar{F_x} = \frac{1}{n}\sum_{i=1}^{n} F_{x_i}. \tag{4.1}$$

To give a good estimation of the nominal force another approach has to be taken. When the actuator is shifted by one period, it covers one N-pole magnet and one S-pole magnet. Since the geometry is not changing during this shift, the force generated over the N-pole magnet has to be the same as generated over the S-pole magnet. The only difference is that the force ripples are in opposite directions. It can also be concluded that the force can be described as a

periodic function with a starting point and an end point of the period. In this case the starting point will be in the middle of a S-pole magnet and the end point in the middle of the next S-pole magnet. Because these points must have the same result from the analysis, this gives some indication of the accuracy. The next thing that is done is to subtract the value of the starting point and end point from all the results gained by FEM. This results in the force ripple of the actuator. Since this ripple has to be zero over one period, the average is calculated by (4.1).

All the gained FEM results will be plotted in graphs and compared with each other. To make a good comparison between the results more calculations have to be done. To gain the effective value of the cogging force and nominal force, the RMS value is calculated by:

$$F_{x_{RMS}} = \sqrt{\frac{1}{n}\sum_{i=1}^{n}(F_{x_i})^2} \tag{4.2}$$

As the iron core of the mover becomes saturated, the force ripple will increase. To give a good estimation of this the peak-peak value, the force (F_{PP}) and the standard deviation of the force ripple (F_{SD}) are calculated. This is done by means of (4.3) and (4.4):

$$F_{x_{PP}} = MAX\,(F_X) - MIN\,(F_X) \tag{4.3}$$

$$Fx_{SD} = \sqrt{\frac{1}{n}\sum_{i=1}^{n}\left(F_{x_i} - \bar{F_{x_i}}\right)^2} \tag{4.4}$$

4.2 Initial cogging force calculation

Analyzing the initial model with the FEM software package is done by a parametric analysis. In the parametric analysis the position of the mover is given as a variable that is increased with 1mm until the mover is shifted over one period. First, the cogging force of the model is analyzed. Since the cogging force is generated by the difference in airgap reluctance caused by the teeth of the actuator, the cogging force is analyzed when no current is applied to the coils.
Result gained by the FEM simulation is shown in Fig. 4.1 The accuracy of the

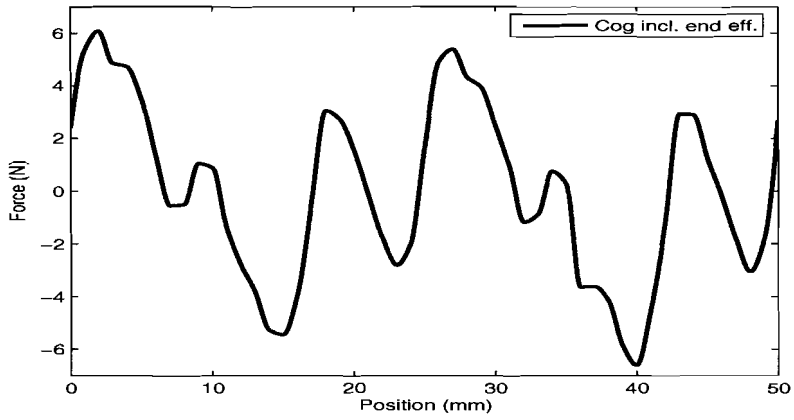

Figure 4.1: Cogging force of initial ICLPMA model, simulated over one period without coil excitation and with discrete steps of 1 mm.

result is calculated by (4.1) and the effective cogging force of the initial model is calculated by (4.2). Between the mover and the backplate an attraction force (F_{Att}) is generated. Therefore, bearings are installed to keep a uniform airgap over the entire length of the back plate. The attraction force is analyzed because the bearings have to withstand the attraction force between the mover and the back plate.
Because the parametric analysis over one period with steps of 1mm requires hours of simulation time, the actuator is again analyzed with steps of 2, 5 mm. In Fig. 4.2 the results of the parametric analysis with discrete steps of 1 mm and 2, 5 mm are shown. Since the step size is increased it is expected that the accuracy of the simulation will decrease. Table 4.1 gives the calculated difference between the two discrete step sizes and therefore the decrease of accuracy. The expectation was right, the accuracy is decreased but still high. This is caused by the low average cogging force and the small differences in effective- and peak force. Because the small difference in accuracy, a discrete step size of 2, 5 mm is chosen as a standard step size. The cogging force presented in Fig 4.1 is build up out of two forces. The major force (detent force) is generated due to the change in airgap reluctance caused by the slotted structure of the actuator, the second force is generated at the ends of the actuator due to its finite length. The detent force can be determined by analyzing the initial ICLPMA without the two end

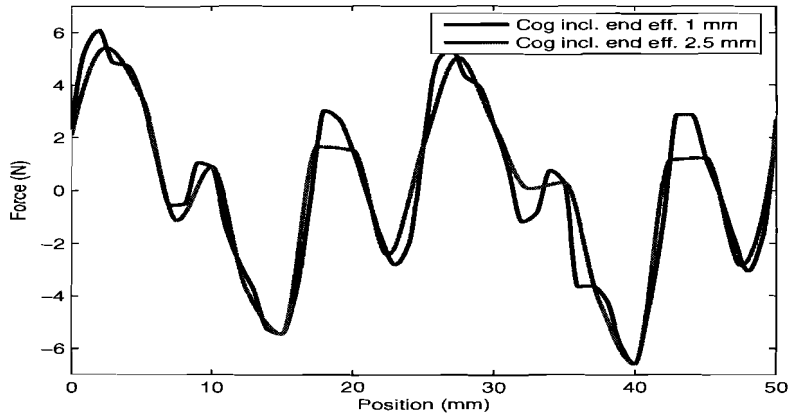

Figure 4.2: Cogging force of initial ICLPMA model, simulated over one period without coil excitation and with discrete steps of 1 mm and 2.5 mm.

Table 4.1: Calculated values for different discrete simulation steps to determine the difference.

Calculation	Simulation 1mm steps (N)	Simulation 2.5mm steps (N)
$F_{AV_{Cogging}}$	−0.0034	0.0266
$F_{RMS_{Cogging}}$	3.3282	3.3296
$F_{PP_{Cogging}}$	12.66	12

teeth. The difference between the cogging force including the end-teeth and the cogging neglecting the end-teeth will determine the end effect. The geometry used to determine the detent force and end effect is shown in Fig. 4.3.

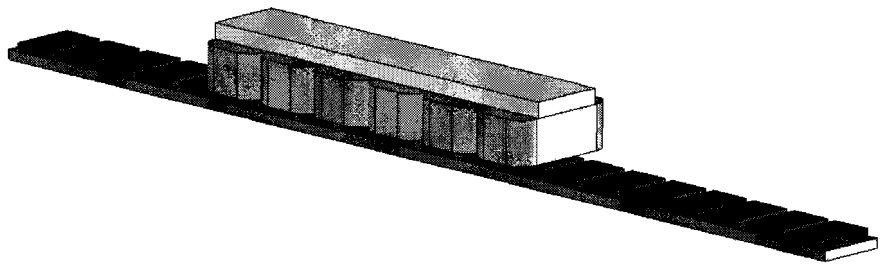

Figure 4.3: Geometry of the initial ICLPMA without end-teeth, used to determine the end effect.

In the FEM software package master/slave boundaries are set so that the flux coming out of the master boundary is inserted into the slave boundary. These boundaries are at the end parts of the mover iron. This will give the mover a infinite length thereby exclude the end effect. The force generated over one period and with a discrete step size of 2,5 mm and without the end-teeth is presented in Fig. 4.4. The calculations made to determine the difference between

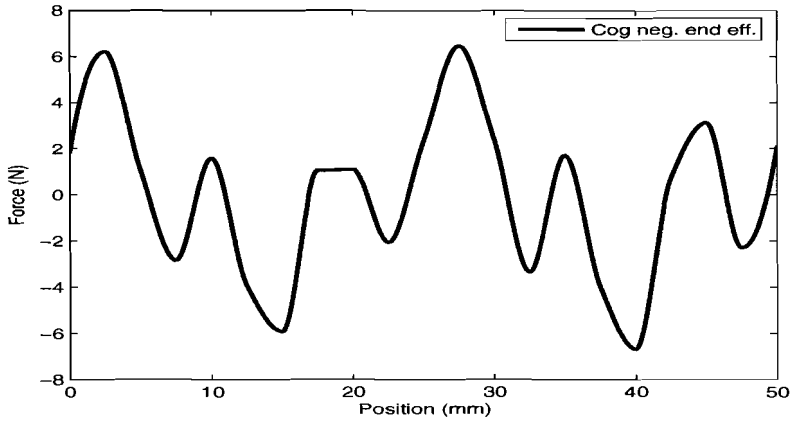

Figure 4.4: Detent force generated by the initial ICLPMA due to teeth structure of yoke.

the detent force and the total cogging force of the initial ICLPMA model are given in Table 4.2, where the calculations for the initial model are described

Table 4.2: Calculated difference between the geometry including end-teeth and the geometry neglecting the end-teeth.

Calculation	Value (N)
$F_{AV_{Neg.\ end\ teeth}}$	0.031
$F_{AV_{Incl.\ end\ teeth}}$	0.027
$F_{RMS_{Neg.\ end\ teeth}}$	3.59
$F_{RMS_{Incl.\ end\ teeth}}$	3.32
$F_{PP_{Neg.\ end\ teeth}}$	13.14
$F_{PP_{Incl.\ end\ teeth}}$	12

by the subscript "Incl. end teeth" and the geometry without the end-teeth by "Neg. end teeth". From the calculations of the effective force and the peak force, can be concluded that the detent force of the geometry without the end teeth is higher than the total cogging force of the initial model. In Fig. 4.5 the forces of both models are depicted to show this phenomenon more clearly.

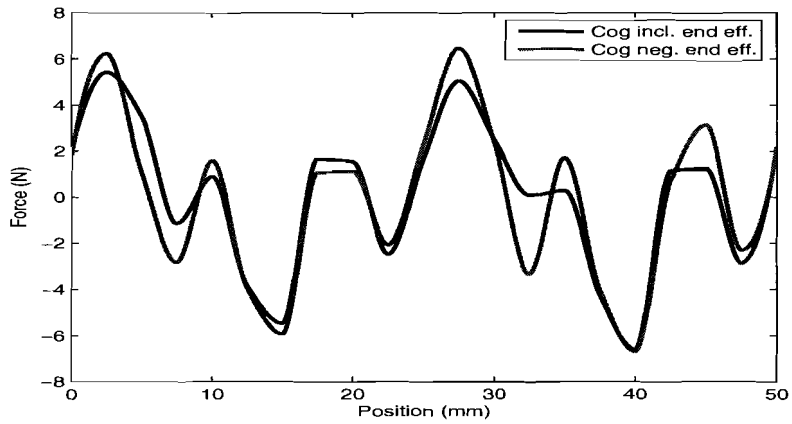

Figure 4.5: Cogging force over one period, considering and neglecting end effects.

4.3 Nominal excitation

At nominal excitation the actuator will be excited with 3600 Ampere turns (NI), with an average of 290 turns per coil. Since the two coils of one phase are in series, this becomes $12,4A$ per phase. The NI is set as default variable due to the fact that the coil turns can differ because they are manually wound. The nominal NI of 3600 Ampere turns can than easily be reached by increasing or decreasing the phase current. The initial ICLPMA model (Fig. 1.2) is analyzed by the FEM and the force, inductances and flux linkage at nominal excitation are defined.

4.3.1 Nominal Forces

The propulsion force (F_x), which is in the model present in the x-direction, and the attraction force (F_{Att}), which is present in the z-direction, is analyzed by the FEM. The variation of Fx over one period of the actuator with discrete steps is shown in Fig. 4.6. From the results of the FEM analyses, the RMS force generated over one period is calculated together with the peak-peak value to validate the amount of the force ripple later on. The values are given in Table 4.3.

Table 4.3: Calculations of generated forces of the initial ICLPMA model at nominal excitation

Calculation	Value (N)
$F_{RMS_{Nominal}}$	$455,86$
$F_{PP_{Nominal}}$	$51,63$
$F_{Att_{Nominal}}$	$1247,5$

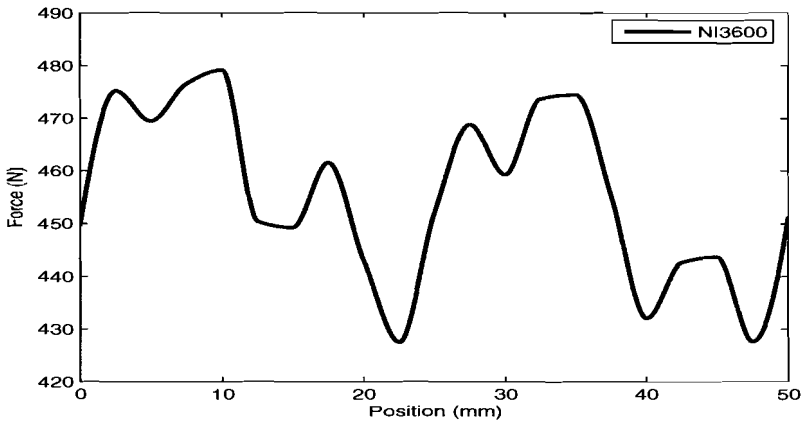

Figure 4.6: Force in direction of travel over one period of the initial ICLPMA model

4.3.2 Inductances

Calculated inductances of the three phases of the actuator, varying over one period, are shown in Fig. 4.7. The variation is small and to determine an average inductance for every phase, the average value (4.1) is calculated for every phase inductance and, if analyses is correct, must be the same. The FEM

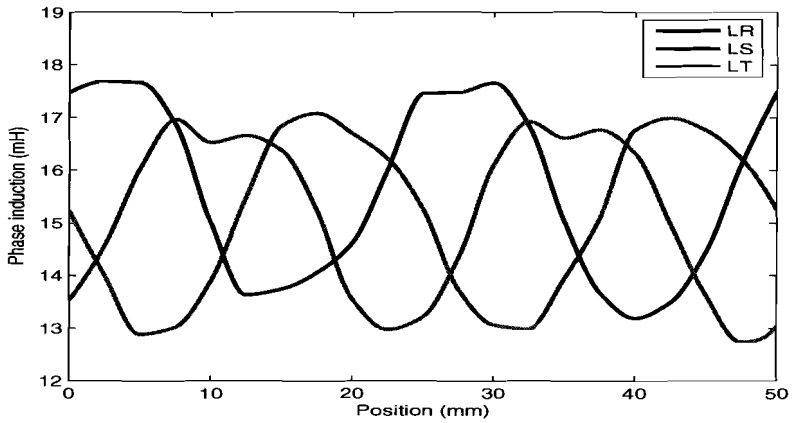

Figure 4.7: Coil induction over one period of the initial ICLPMA model

analysis also includes the mutual inductances between the coils. Combining average mutual inductances with the phase inductances in a matrix gives the

inductance matrix of the actuator (4.5):

$$\mathbf{L_m} = \begin{bmatrix} L_R & L_{SR} & L_{TR} \\ L_{RS} & L_S & L_{TS} \\ L_{RT} & L_{ST} & L_T \end{bmatrix} \tag{4.5}$$

The calculated values are given in (4.6), values are given in mH:

$$\mathbf{L_m} = \begin{bmatrix} 15.7 & -0.34 & -1.14 \\ -0.34 & 15.1 & -1.27 \\ -1.14 & -1.27 & 15.1 \end{bmatrix}, \tag{4.6}$$

where the difference in the average inductance value is caused by the numerical error of the FEM package and the different flux densities caused by the end teeth.

4.3.3 Electro Motive Force (emf)

In the coils of the actuator an emf will be generated dependent on the speed of the mover and the change of magnetic flux (ϕ_t) in the teeth surrounded by a coil according to:

$$E_{Phase} = N_{coil} \cdot \frac{d\phi_t}{dt}. \tag{4.7}$$

Moving along x-direction an induced emf will be expressed as:

$$E_{Phase} = N_{coil} \cdot \frac{d\phi}{dx} \cdot \frac{dx}{dt}. \tag{4.8}$$

The emf of the three phases is calculated by the FEM and shown in Fig. 4.8. From the induced emf the RMS-value is calculated and is given in Table 4.4

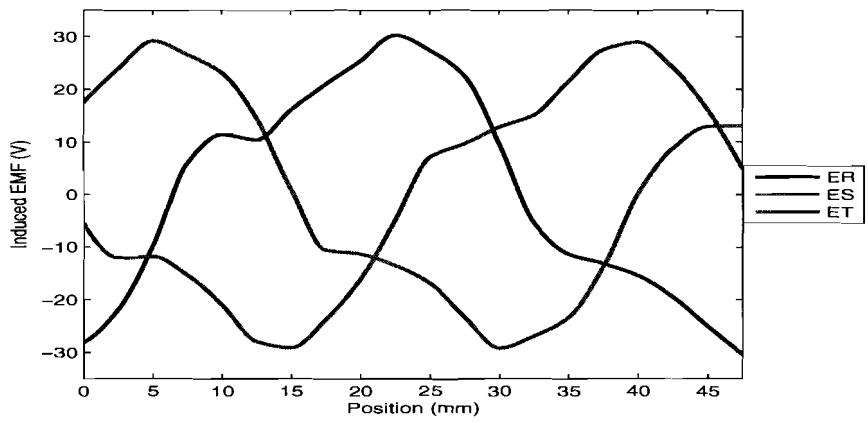

Figure 4.8: Induced emf over one period of the initial ICLPMA model.

Table 4.4: RMS value of induced emf of the initial ICLPMA model.

Calculation	Value (V)
E_R	20.2
E_S	19.4
E_T	19.1

4.3.4 Generated forces

The actuator presented in Fig. 4.3, is analyzed for a variation of NI starting in the linear region and ending at the saturated region. For the different values of NI the peak-peak value (F_{PP}) over one period is calculated. It follows that the force ripple will increase as the yoke of the mover becomes saturated. The RMS force is calculated to see how the actuator force will act as a function of the current. The attraction force of the actuator is also calculated, this is done with the aim to define which force the bearings have to withstand to keep a constant airgap between the mover and the back plate. Since the forces to the sides of the mover cancel out due to the symmetric geometry, these values are not analyzed. The forces to the sides of the mover are for this model in y-direction. The RMS force F_{RMS}, peak peak force F_{PP} and attraction force F_{ATT} are given in Table 4.5.

Table 4.5: Calculated forces of the initial ICLPMA model over one period and for different NI.

$NI\,(A)$	$F_{RMS}\,(N)$	$F_{PP}\,(N)$	$F_{ATT}\,(N)$
1500	292.75	13.36	817.5
2100	310.4	27.75	929.8
3000	405.26	44.76	1117.9
3600	455.86	51.63	1247.5
3900	473.69	62.62	1291.9
4500	507.94	75.91	1401
4800	519.37	68.68	1443.3

The influence of Ampere-turns on the force values is plotted in Fig. 4.9(a) which clearly shows the linear and saturated regions where the force ripple increase as the yoke of the actuator starts to be saturated as the number of Ampere-turns increases. In Fig. 4.9(b) a 2D plot of Fig. 4.9(a) is illustrated to show the increase of the force ripple more clearly. As the yoke starts to be saturated it can be

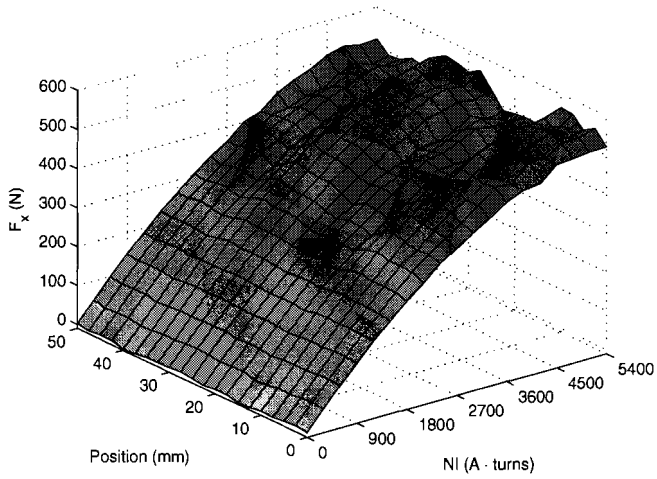

(a)

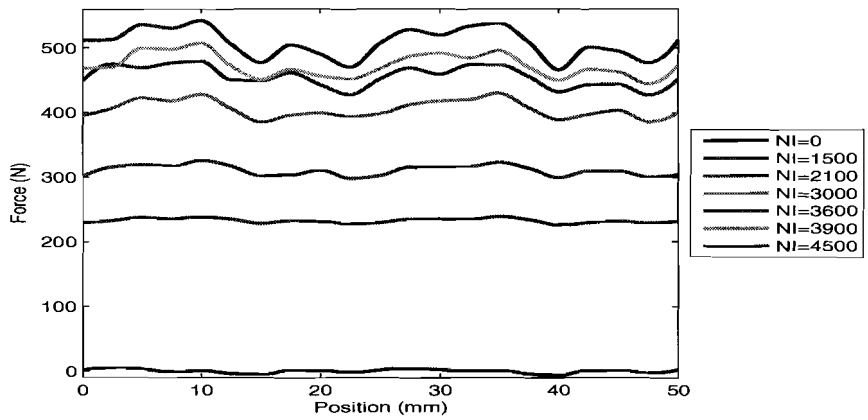

(b)

Figure 4.9: Propulsion force as a function of position and a number of Ampere turns: 4.9(a) 3D plot 4.9(b) 2D plot.

concluded that the motor constant (K) decreases. In Fig. 4.10 the increase of the peak-peak force F_{PP} (4.10(a)) and average force ripple F_{SD} (4.10(b)) are present to verify the saturation level. It can be seen that at $NI = 4800$ Ampere-turns the yoke is fully saturated as the peak-peak value decreases but the average value of force ripple increases.

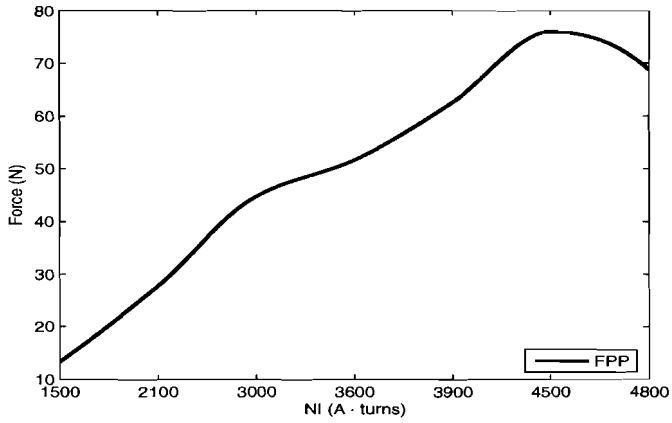

(a)

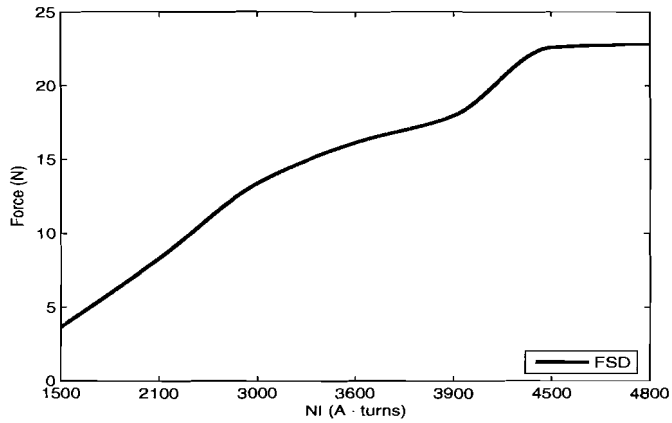

(b)

Figure 4.10: Values of peak-peak force F_{PP} and values of average force ripple F_{SD} at different Ampere turns: 4.10(a) F_{PP} 4.10(b) F_{SD}.

From the propulsion force results for different NI, Fig. 4.9(a), it is possible to determine the relation between the propulsion force and the current in the coils. This relation shows the ratio of propulsion force divided by the current amplitude and is calculated by:

$$\frac{F}{i} = \frac{F_{x_{NI}}}{\hat{i_{NI}}}. \tag{4.9}$$

The result is presented in Fig 4.11.

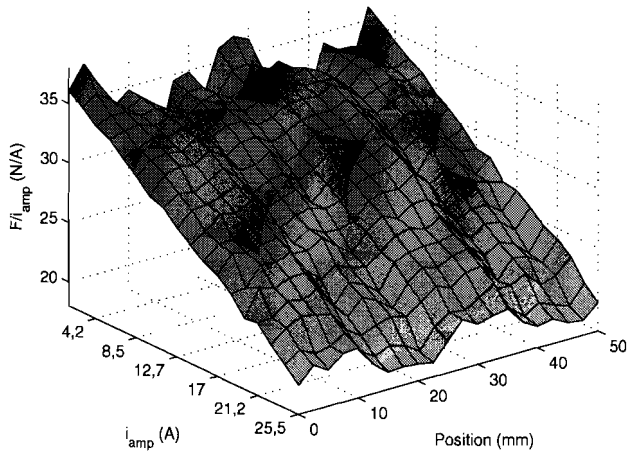

Figure 4.11: Ratio of propulsion force divided by the current amplitude as a function of current and position.

Table 4.6: F_{RMS} calculation results of propulsion force for different current angles (φ_c) in electrical degrees.

φ_c	$F_{RMS}\,(N)$	φ_c	$F_{RMS}\,(N)$
-40	327,15	10	453,52
-30	376,31	20	442,79
-20	411,57	30	412,49
-10	439,52	40	369,20
0	455,86		

4.3.5 Commutation

To determine the accuracy of the commutation of the initial ICLPMA model, a current angle shift (φ_c) is introduced in the current system described by (3.10). Changing the current angle will introduce a decrease of propulsion force since the commutation is designed to obtain maximum propulsion force. The currents are shifted by φ_c from -40 electrical degrees to $+40$ electrical degrees with discrete steps of 10 electrical degrees. This shift is analogous to a displacement of $-5,55$ mm to $+5,55$ mm where a positive shift is in the direction of travel and a negative shift is opposite to the direction of travel. The propulsion force for each discrete step of φ_c is analyzed by the FEM over one period of the initial ICLPMA with discrete steps of $2,5$ mm. The results obtained by FEM are presented in Fig. 4.12. For each discrete step of φ_c, the RMS value over one period is calculated and given in Table. 4.6. From the calculation results in Table. 4.6 and Fig. 4.12 it can be concluded that the maximum force is obtained when the $\varphi_c = 0$ electrical degrees.

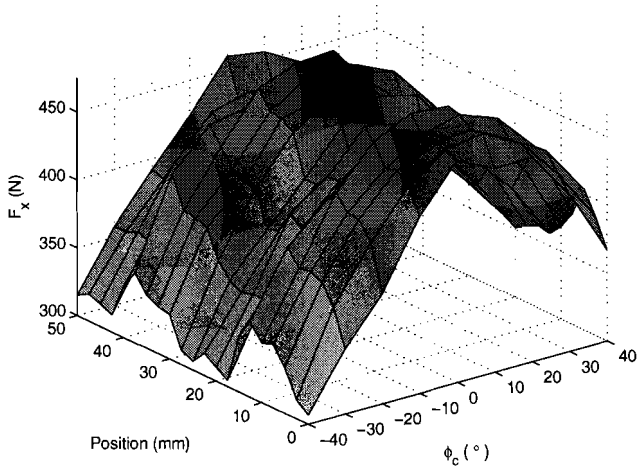

Figure 4.12: Propulsion force as a function of φ_c and position.

4.4 Conclusion

The results obtained in this chapter show that the initial ICLPMA of Tecnotion B.V. has a low cogging force and almost a linear force to current ratio over a wide range of current. The calculated commutation (5.1) is correct due to the results gained by the FEM analysis with different current shifts. In comparison with the MEC model there is a difference of 2% in calculated nominal propulsion force. The values of the cogging forces and nominal forces are used to compare the cogging forces and nominal forces obtained by FEM in the next chapter. By FEM analysis it is possible to give a qualitative estimation for the different force components and it must be taken into account that the qualitative analysis and treatment of the physical phenomena request a creation of extended analytical tools which is beyond the scope of this thesis.

Chapter 5

Geometry Variation of the Stator Back Iron.

The main topic of this project is to revise the influence of the shape of the iron backplate on the force level. Because there can be made many changes in the geometry of the backplate, this project is focusing on the behavior of the mover on a curved iron backplate. Analyzes will be done on the different curves of the backplate which will be specified in diameters, varying from 7.2 meters to 90 centimeters.

5.1 Commutation

When a curved iron back plate is used the commutation of the initial actuator changes because the traveled distance is now described by an angle instead of a distance. The commutation factor (Cf) is different for every diameter caused by the increase of the angle compared with the traveled distance on a specific diameter. To find the commutation factor, the angle belonging to a distance of one magnet pitch, τ_{mp}, on diameter d is calculated by (5.1). The commutation factors for the different diameters are given in Table 5.1. These values are calculated for angles given in mechanical degrees:

$$Cf = \frac{\pi}{\frac{2 \cdot \pi}{\pi \cdot d} \cdot \frac{1}{2} \cdot \tau_{mp}} = \frac{\pi}{\frac{1}{d} \cdot \tau_{mp}} \tag{5.1}$$

Since the simulations are done the same as with the initial model, discrete

Table 5.1: Commutation factors for different diameters of the iron backplate.

Diameter (mm)	Commutation factor
7200	452, 39
3600	226, 19
1800	113, 10
900	56, 55

linear steps of 2.5mm are converted to the angular position, φ belonging to

the specific diameter. The angular position values of the discrete steps for the different diameters are given in Table 5.2. It must be taken into account that how lager the number of decimals how accurate the position over a large distance from the origin and because of this there will be lower commutation errors.

Table 5.2: Angular position step for the different diameters of the iron backplate

Diameter (mm)	Angular position step φ
7200	0,039
3600	0,079
1800	0,159
900	0,318

5.2 Force calculation

By means of FEM the force in a Cartesian coordinate system is calculated. The force generated by the actuator is defined in the direction of travel of the mover. Since the direction of travel of the initial model is in the x-direction of the coordinate system, the force in this direction can be defined as a cogging force (without currents), or, when excited by the nominal current, as a nominal force. When the iron backplate is curved the cogging force and actuator force must be defined on the curved path instead of the Cartesian components used with the initial model. First, a starting position for the mover on the iron backplate is defined and illustrated in Fig. 5.1, where φ is the angle between the starting position and the actual position of the mover. If the mover is analyzed over a

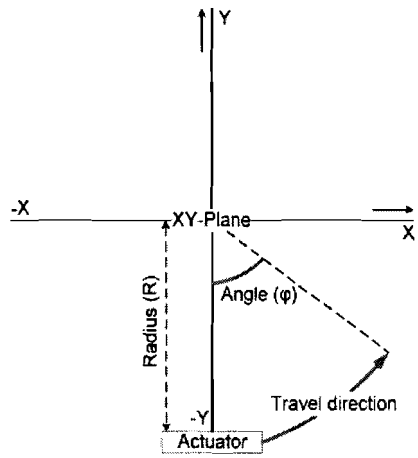

Figure 5.1: Starting position and travel direction of the ICLPMA mover.

circle, calculated force components in $x-$ and y-directions will be distributed as depicted in Fig. 5.2, where 1 to 8 are steps of 45° in the direction of travel. The actual force on the path is defined by the vector sum product components

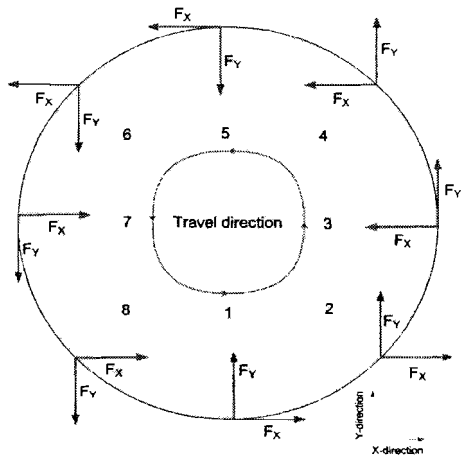

Figure 5.2: Force directions of the ICLPMA calculated by FEM in cartesian coordinates traveling in a circular motion.

of F_X and F_Y tangent to the analyzed point. Fig. 5.3 illustrates the calculated components of F_X and F_Y from which the actual force in the direction of travel is calculated and are defined as, F_{XT} and F_{YT} as the tangent components of F_X and F_Y, respectively. F_{XY} is the combined force of F_X and F_Y and gives the total force and direction acting on the mover in the XY-plane. The sum of

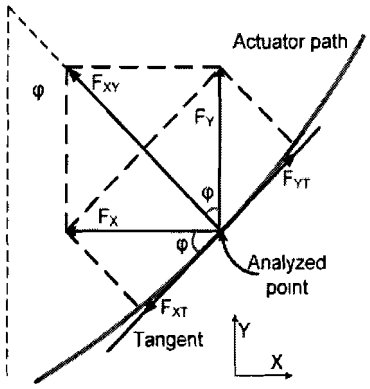

Figure 5.3: FEM force components and extraction of the force in the direction of travel.

the tangent components describes the actual force generated by the mover on the curved path and is calculated by:

$$\begin{aligned} F_{XT} &= F_X \cdot \cos(\varphi), \\ F_{YT} &= F_Y \cdot \sin(\varphi). \end{aligned} \tag{5.2}$$

Because they are aligned the sum becomes:

$$F_{Path} = F_X \cdot \cos(\varphi) + F_Y \cdot \sin(\varphi). \tag{5.3}$$

To verify this, the FEM analyzes are done at 45°, 90°, 135° and 180° (step 2 to 5 in Fig. 5.2) from the starting position (Fig. 5.1) on a curve with a diameter of $1.8m$ and at mover positions of $0mm$, $25mm$. Results are mentioned in Table 5.3, where the actual force in direction of travel (F_{Act}) along the circular curve is calculated for every angular position at the nominal current.

Table 5.3: FEM results at different actuator angles for different mover positions, (force values and calculations are in newton (N)).

		Mover position					
		$0mm$			$25mm$		
Angle (φ)	NI (A)	F_X	F_Y	F_{Act}	F_X	F_Y	F_{Act}
45°	3600	326,91	321,8	458,52	319,06	329,81	458,73
90°	3600	1,97	457,67	457,43	-15,56	459,14	458,98
135°	3600	-321,24	325,73	457,28	-328,3	318,51	457,27
180°	3600	-458,17	-1,76	457,8	-457,9	-10,03	457,79

5.3 Diameter of 7.2 meters

A diameter of 7.2 meters is chosen because the circular curve of this diameter is approximated to the straight iron backplate of the initial model in comparison with the small length of the mover (248mm). The top view of the geometry is presented in Fig. 5.4 and a 3D-view of the geometry is shown in Fig. 5.5. Notice that the both ends of the mover deflect from the curved backplate and that the deflection will increase as the diameter of the circular curved backplate decreases as described in later sections of this chapter.

The position of the curve and the actuator in the xy-plane starts at negative

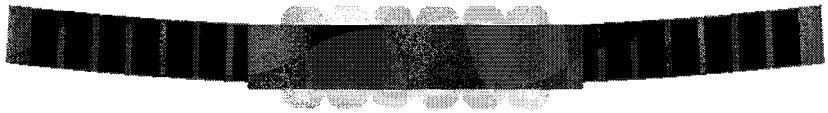

Figure 5.4: The initial mover on a circular curved backplate with a diameter of $7.2m$, top view.

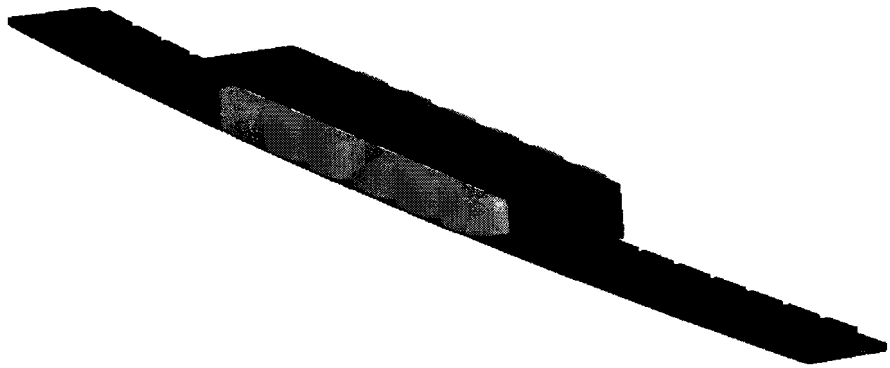

Figure 5.5: The initial mover on a circular curved backplate with a diameter of $7.2m$, 3D-view.

y-axis ($x = 0$) at radius distance from the origin and turning towards the positive x-axis, as illustrated in Fig. 5.1. The geometry is analyzed with angular position steps of $0,039°$, as mentioned in Table 5.2. Over one period of the actuator the analyzes are done for cogging force and nominal force, defined by zero current and nominal current, respectively. The analyzed actual cogging force on the path of the actuator is presented in Fig. 5.6.

From these results the average force ripple, F_{SD}, the RMS force, F_{RMS}, and peak-peak force, F_{PP}, are calculated and given in Table 5.4. To verify these results with the initial model, cogging force results of the initial model are included at the same Table 5.4.

From these results it can be concluded that the cogging force decreases because the RMS value is decreasing. The smoothness of the cogging force over one pe-

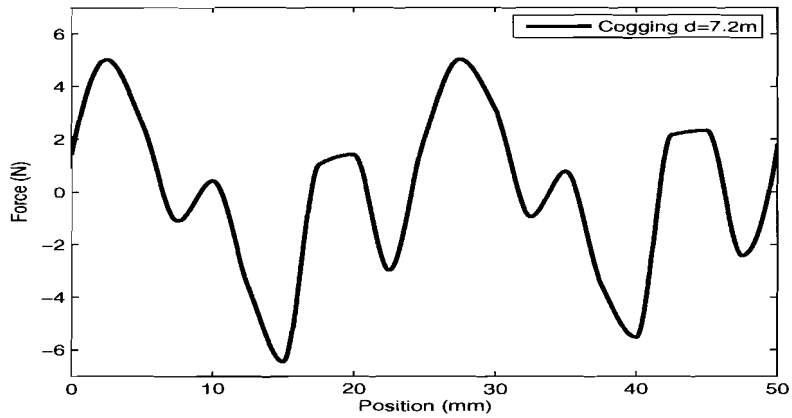

Figure 5.6: Cogging force of the ICLPMA model on a circular curved backplate of 7.2m diameter obtained by FEM.

Table 5.4: Comparison of cogging force results of a circular curved backplate with a diameter of $7.2m$ and the backplate of the initial model.

Calculation	For $d = 7.2$m model (N)	For initial model (N)
F_{AV}	0,0479	-0,0034
F_{SD}	3,254	3,328
F_{RMS}	3,172	3,295
F_{PP}	11,483	12,666

riod is increasing, because the peak value is decreasing in comparison with the initial model. As mentioned before, the model is, besides cogging force, analyzed at nominal current to calculate the nominal force. Results are presented in Fig. 5.7 and calculations of these results are given in Table 5.5. From the

Table 5.5: Comparison of nominal force results of a circular curved backplate with a diameter of $7.2m$ and the backplate of the initial model.

Calculation	For $d = 7.2$m model (N)	For initial model (N)
F_{AV}	474,853	455,573
F_{SD}	13,386	16,52
F_{RMS}	475,032	455,857
F_{PP}	43,643	51,626

results in Table 5.5 it can be concluded that the nominal force is increased and the peak force is decreased in comparison with the initial model. Because this was initially not expected, another geometry is analyzed. Since the initial model can be described as a circular curve where the diameter (D) approaching infin-

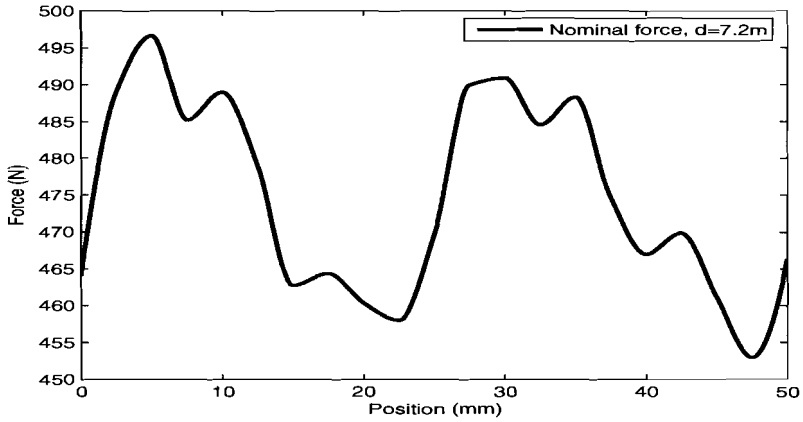

Figure 5.7: Nominal force of the ICLPMA model on a circular curved backplate with a diameter of 7.2m obtained by FEM.

ity ($D \rightarrow \infty$). Increasing the diameter must satisfy the same force as the initial model. This is done by increasing the diameter up to 28.8 meters and analyzed for nominal current. Results from the FEM analysis of the 28.8m diameter and of the initial model are presented in Fig 5.8. The calculated forces are given in Table 5.6.

The nominal force is decreased to the nominal force of the initial model. From

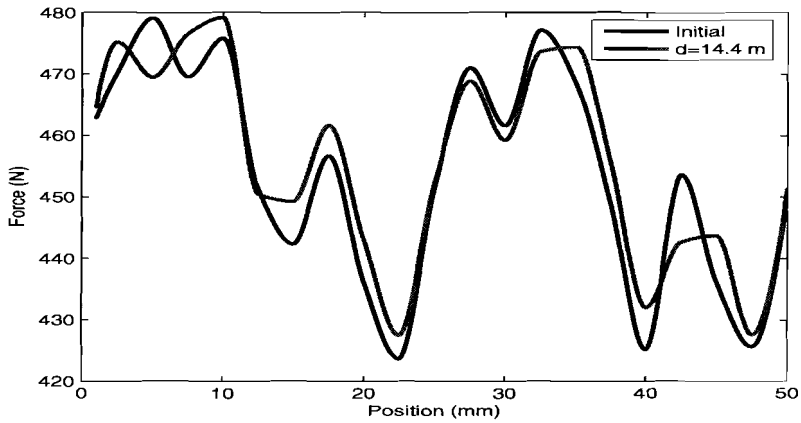

Figure 5.8: Nominal force of the ICLPMA model on a circular curved backplate with a diameter of 28.8m and on the initial backplate obtained by FEM.

this it can be concluded that the circular curved backplate with a diameter of 7.2m introduces an increase of nominal force in comparison with the initial model.

Table 5.6: Comparison of nominal force results of a circular curved backplate with a diameter of 28.8m and the backplate of the initial model.

Calculation	For $d = 28.8m$ model (N)	For initial model (N)
F_{AV}	454,034	455,573
F_{SD}	17,906	16,52
F_{RMS}	454,369	455,857
F_{PP}	55,467	51,626

5.4 Diameter of 3.6 meters

After the simulations of the $7.2m$ diameter model, the mover is analyzed on a circular curved backplate with a diameter of $3.6m$. Because this is a half of the diameter of $7.2m$ it can be said that the curve, over which the mover is moved, is twice as sharp as before. The deflection of the end teeth is therefore twice as much. The top view of the geometry is depicted in Fig. 5.9 and a 3D view of the geometry is presented in Fig. 5.10.

With this model the same analyses are done as before, starting with the cogging

Figure 5.9: The initial mover on a circular curved backplate with a diameter of 3.6m, top view.

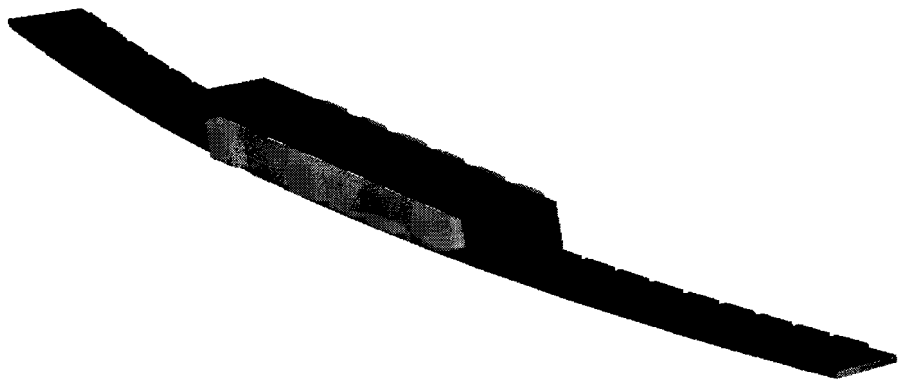

Figure 5.10: The initial mover on a circular curved backplate with a diameter of 3.6m, 3D-view.

force and followed by the nominal force at nominal current and over one period of the actuator. The starting position is still the same as depicted in Fig. 5.1.

The angular position step for this diameter is $0,079°$ as mentioned in Table 5.2. The result of the actual cogging force on the path of the actuator is presented in Fig. 5.11. Calculated values to verify the results with the initial model are given in Table 5.7. It can be seen that the RMS value of the cogging is still decreasing and the smoothness of the cogging force increases again because the peak value is still decreasing.

The result of the nominal force for this model is presented in Fig. 5.12, the

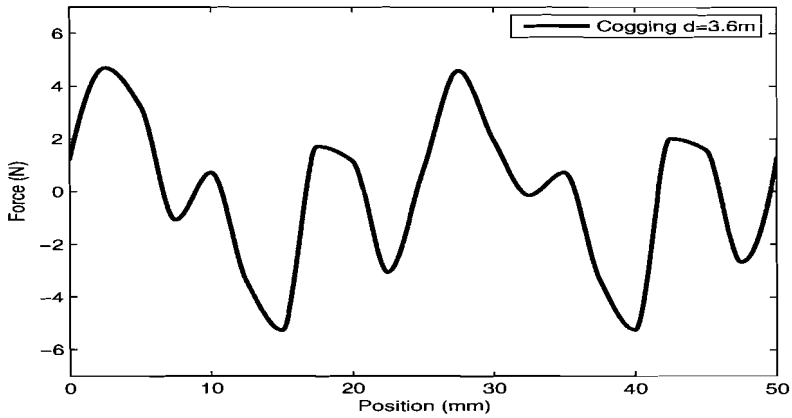

Figure 5.11: Cogging force ICLPMA model on a circular curved backplate of 3.6m diameter obtained by FEM.

Table 5.7: Comparison of cogging force results of a circular curved backplate with a diameter of 3.6m and the backplate of the initial model.

Calculation	For $d = 3.6$m model (N)	For initial model (N)
F_{AV}	0,0150	-0,0034
F_{SD}	2,962	3,328
F_{RMS}	2,887	3,295
F_{PP}	9,946	12,666

calculated values to verify the results with the initial model, are given in Table 5.8.

The RMS value shows a decrease of $0,4\%$ in comparison to the 7.2m diameter model, from which can be concluded that the nominal force stays the same. The peak force shows an increase of $4,1\%$ which causes a larger force ripple in comparison with the 7.2m diameter model.

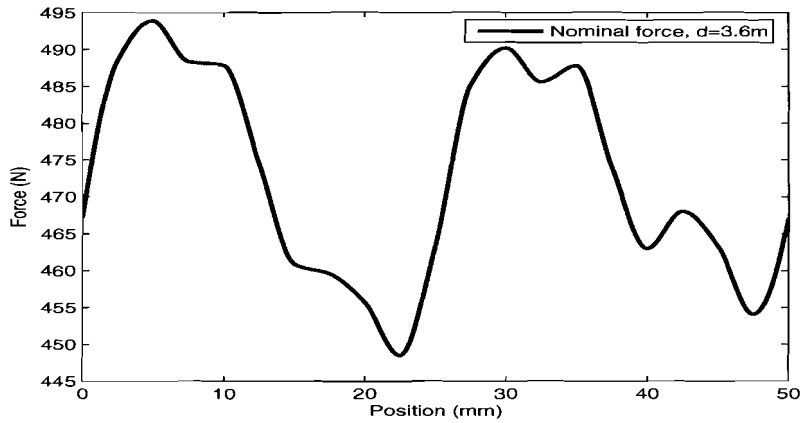

Figure 5.12: Nominal force ICLPMA model on a circular curved backplate of 3.6m diameter.

Table 5.8: Comparison of nominal force results of a circular curved backplate with a diameter of 3.6m and the backplate of the initial model.

Calculation	For $d = 3.6$m model (N)	For initial model (N)
F_{AV}	472,960	455,573
F_{SD}	14,302	16,52
F_{RMS}	473,166	455,857
F_{PP}	45,424	51,626

5.5 Diameter of 1.8 meters

The diameter of the circular curve in the backplate is again decreased to the half of the diameter before and analyzed by FEM for cogging force and nominal force. The top view of the geometry is shown in Fig. 5.13 and a 3D-view of the geometry is shown in Fig. 5.14.

The cogging force obtained by FEM is presented in Fig. 5.15. The calculations

Figure 5.13: The initial mover on a circular curved backplate with a diameter of 1.8m, top view.

from these results and the calculated results from the initial model are given in Table 5.9.

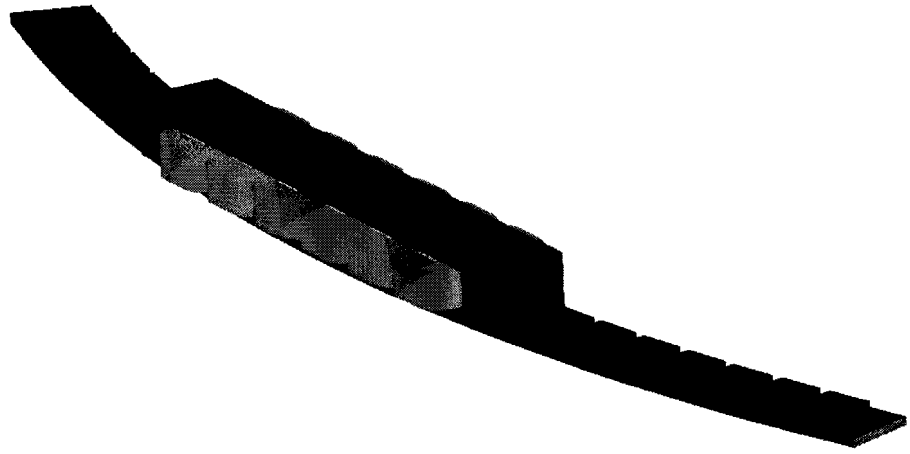

Figure 5.14: The initial mover on a circular curved backplate with a diameter of 1.8m, 3D-view.

The RMS value of the cogging force still decreases and the peak-peak force is

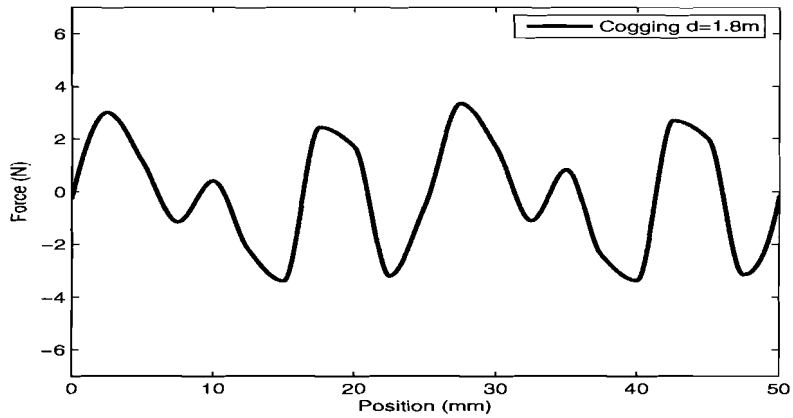

Figure 5.15: Cogging force ICLPMA model on a circular curved backplate of 1.8m diameter.

almost a half of the size of the initial model. This results in an even smoother cogging force as before. To investigate if the RMS and peak value of the nominal force is also decreased, the nominal force is analyzed and presented in Fig. 5.16 and the calculated values are given in Table 5.10.

From these results it can be concluded that the peak value is decreased with $3,28\%$ in comparison to the 3,6m diameter model. In comparison to the 7.2m diameter it shows an increase of $0,66\%$. The RMS value shows a decrease of $1,64\%$ in comparison to the 3,6m diameter model. This decrease shows that the nominal force „returns" to the value of the initial model.

Table 5.9: Comparison of cogging force results of a circular curved backplate with a diameter of 1.8m and the backplate of the initial model.

Calculation	For $d = 1.8$m model (N)	For initial model (N)
F_{AV}	-0,0716	-0,0034
F_{SD}	2,314	3,328
F_{RMS}	2,257	3,295
F_{PP}	6,747	12,666

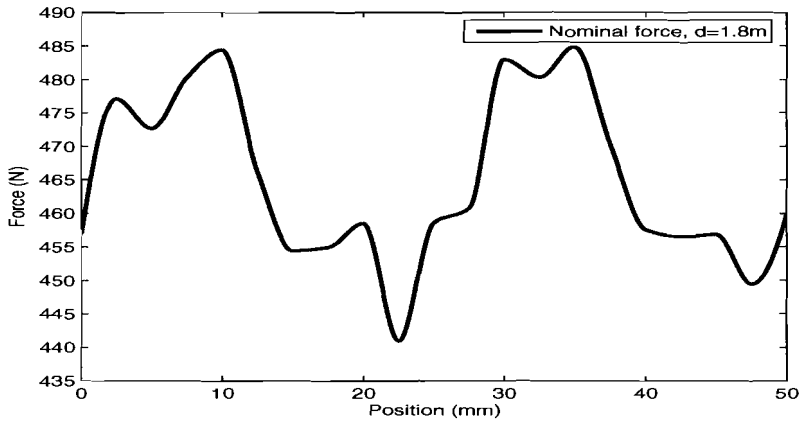

Figure 5.16: Nominal force ICLPMA model on a circular curved backplate of 1.8m diameter.

Table 5.10: Comparison of nominal force results of a circular curved backplate with a diameter of 1.8m and the backplate of the initial model.

Calculation	For $d = 1.8$m model (N)	For initial model (N)
F_{AV}	465,217	455,573
F_{SD}	12,949	16,52
F_{RMS}	465,389	455,857
F_{PP}	43,932	51,626

5.6 Diameter of 0.9 meters

The diameter of the circular curve in the backplate is again decreased to the half of the diameter before and analyzed by FEM. The top view of the geometry is shown in Fig. 5.18 and a 3D-view of the geometry is shown in Fig. 5.18.

The analyzed cogging force is presented in Fig. 5.19 and the calculated values of these results are given in Table. 5.11.

It can be seen that the cogging force has changed in a shape. Where the other diameters have the same values for the peak forces, the $0.9m$ diameter model

Figure 5.17: The initial mover on a circular curved backplate with a diameter of $0.9m$, top view.

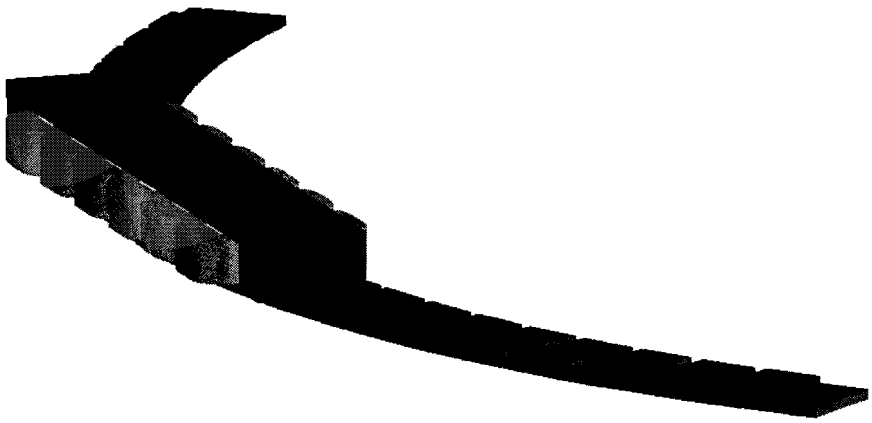

Figure 5.18: The initial mover on a circular curved backplate with a diameter of $0.9m$, 3D-view.

shows a relative smooth force with two main peaks.

The values of the two peaks in the cogging force introduce an increase of the

Table 5.11: Comparison of cogging force results of a circular curved backplate with a diameter of 0.9m and the backplate of the initial model.

Calculation	For $d = 0.9$m model (N)	For initial model (N)
F_{AV}	-0,0818	-0,0034
F_{SD}	2,836	3,328
F_{RMS}	2,766	3,295
F_{PP}	10,298	12,666

peak value. In Table. 5.11 it can be seen that the peak force increases towards the peak force of the initial model. The RMS value of the force is also increasing.

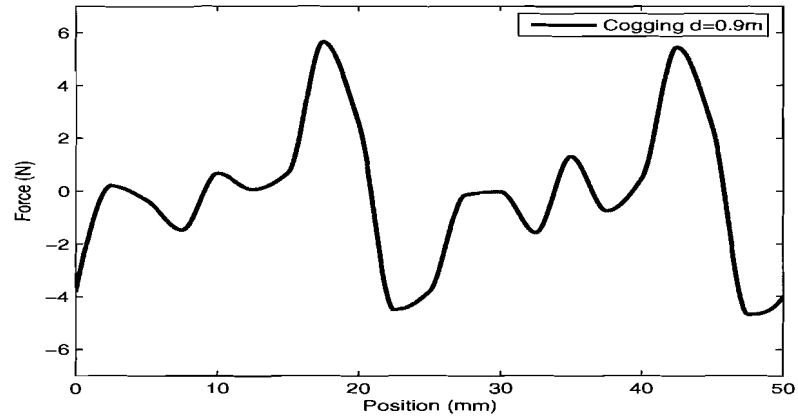

Figure 5.19: Cogging force of ICLPMA model on a circular curved backplate of 0.9m diameter.

The expectation is that the increase of the cogging force will continue as the diameter of the circular curve decreases further. The nominal force is analyzed and results are presented in Fig. 5.20.

Compared to the nominal forces of the other diameters also shows a change

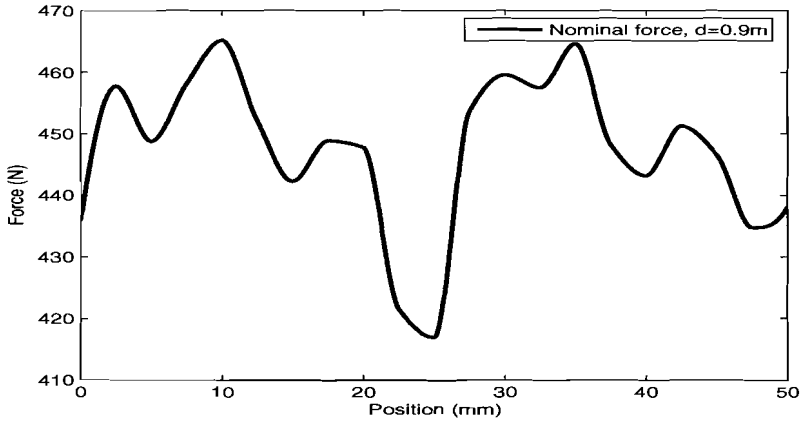

Figure 5.20: Nominal force of ICLPMA model on a circular curved backplate of 0.9m diameter.

in shape. Where the other diameters consist of two major positive peaks. The 0,9m diameter model consists of a relative even force with one major negative peak. The results of the calculations are mentioned in Table 5.12.

These results show that the RMS force is smaller than the RMS force of the initial model. The major negative peak in the nominal force introduces an increase in the calculated peak-peak force. Because this is only one peak,

Table 5.12: Comparison of nominal force results of a circular curved backplate with a diameter of 0.9m and the backplate of the initial model.

Calculation	For $d = 0.9$m model (N)	For initial model (N)
F_{AV}	447,719	455,573
F_{SD}	12,782	16,52
F_{RMS}	447,892	455,857
F_{PP}	48,273	51,626

the average force ripple is still smaller than that of the initial model. The expectation is that the force will continue to decrease as the diameter decreases. But because of the time window for this project it was not possible to analyze an further decrease of the diameter.

5.7 Conclusion

The results of the analysis gained in previous sections of this chapter and the results from the initial model show that the force properties change as the geometry of the backplate changes. First, the results of the cogging force will be discussed and followed by the nominal force results. The results of the cogging force calculations for all diameters and the initial model are summarized in Table 5.13 and the simulation results are presented in Fig. 5.21. From these

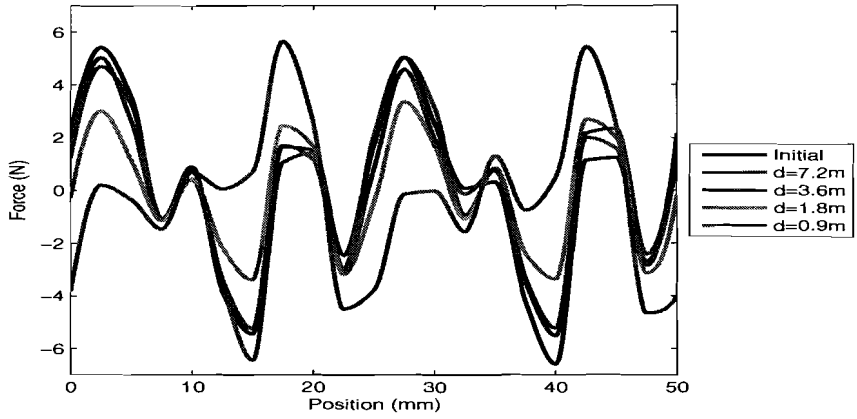

Figure 5.21: Cogging force simulation results in function of position and for different diameters of the circular curved backplate and the initial model.

Table 5.13: Comparison of cogging force calculation results for different diameters of the circular curved backplate and the initial model, (values are given in Newton (N)).

Calc	Initial	$d = 7.2$ m	$d = 3.6$ m	$d = 1.8$ m	$d = 0.9$ m
F_{AV}	-0,0034	0,047	0,0150	-0,071	-0,081
F_{SD}	3,328	3,253	2,9618	2,314	2,836
F_{RMS}	3,294	3,171	2,8869	2,256	2,765
F_{PP}	12,665	11,487	9,9463	6,747	10,298

results it can be concluded that the cogging force decreases as the diameter decreases. Except for the 0.9m diameter where the RMS is increased close to the initial value. This is the same for the peak values. To show this more clearly the RMS values of the cogging forces are presented in Fig. 5.22, and the peak value of the cogging is presented in Fig. 5.23. The decrease of the cogging force can be related to the effective area of the end teeth that are above the backplate. As the diameter decreases the effective area decreases because the backplate deflection increases.

Another cause of the decrease can be related to the fact that the magnets shift

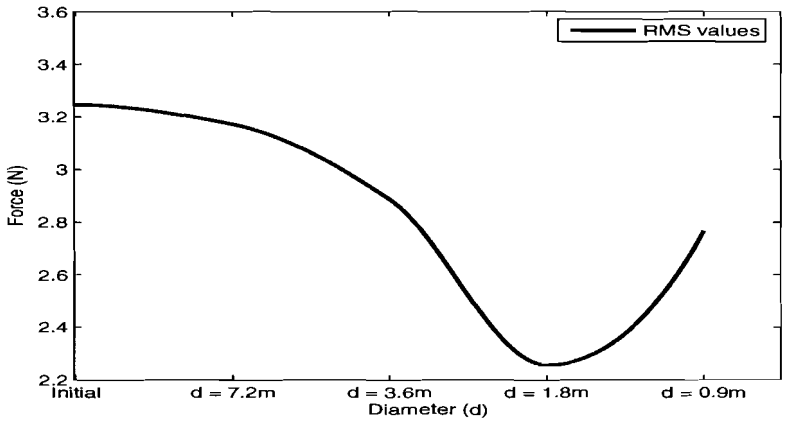

Figure 5.22: RMS values of the cogging forces for different diameters of the circular curved backplate and the initial model.

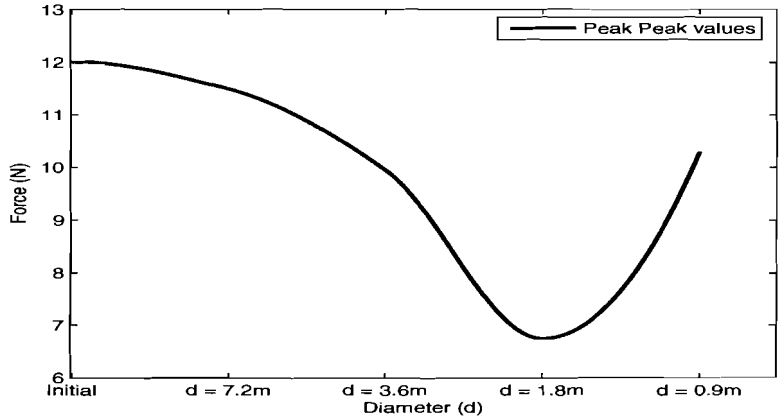

Figure 5.23: Peak-Peak values of the cogging forces for different diameters of the circular curved backplate and the initial model.

as the deflection increases. This can be seen as skewing of the magnets with the differences that the skew angle is different for every tooth. Which proportion causes the main decrease in cogging force is not investigated in this report.
The most interesting fact gained by the results of the cogging force is that the geometry of the initial model can be adjusted to reduce the cogging force. After the adjustment the cogging can be further reduced by skewing the magnets. The nominal force shows also a decrease in propulsion force as the diameter decreases, except that the forces on the circular curved iron backplate are higher than the propulsion force of the initial model until the diameter becomes smaller than 1.8m. The calculated forces are summarized in Table 5.14 where this can be verified. The diameter that generates the same nominal propulsion force as

the initial model is not investigated due to the time window of the project. Future investigation will be necessary to reveil this diameter. It is expected that the diameter that generates the same nominal propulsion force as the initial model also will introduce the turning point in the cogging force.

The nominal propulsion forces of all diameters and the initial model are pre-

Table 5.14: Comparison of nominal propulsion force calculation results for different diameters of the circular curved backplate and the initial model, (values are given in Newton (N)).

Calc.	Initial	$d = 7.2$ m	$d = 3.6$ m	$d = 1.8$ m	$d = 0.9$ m
F_{AV}	455,573	474,853	472,960	465,217	447,719
F_{SD}	16,520	13,386	14,302	12,949	12,782
F_{RMS}	455,857	475,032	473,166	465,389	447,892
F_{PP}	51,626	43,643	45,424	43,932	48,273

sented in Fig. 5.24 and a 3D-view of these forces are depicted in Fig. 5.25 to show this more clearly. From all these results it can be concluded that the

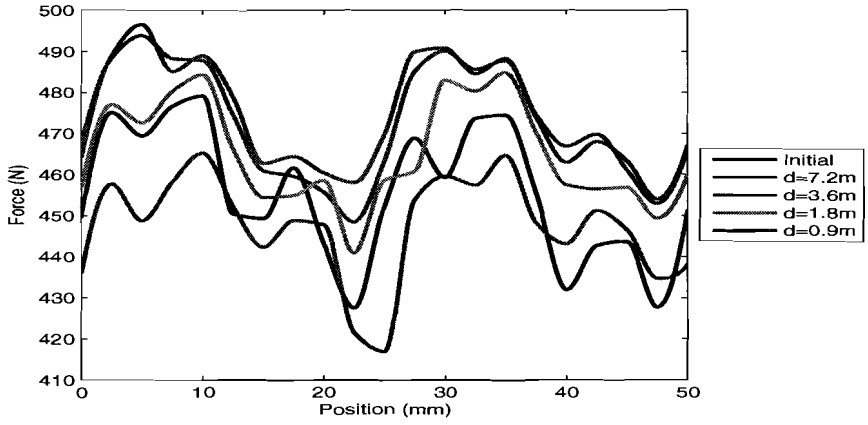

Figure 5.24: Nominal propulsion force as a function of position for different diameters of the circular curved backplate and the initial model in a 2D-view.

change in the iron backplate has no negative effect on the performance of the actuator. It can even be said that the performance increases as the diameter of the backplate decreases until a certain value. This can be seen in Fig. 5.26, where the RMS values of the nominal propulsion force as function of diameter is illustrated.

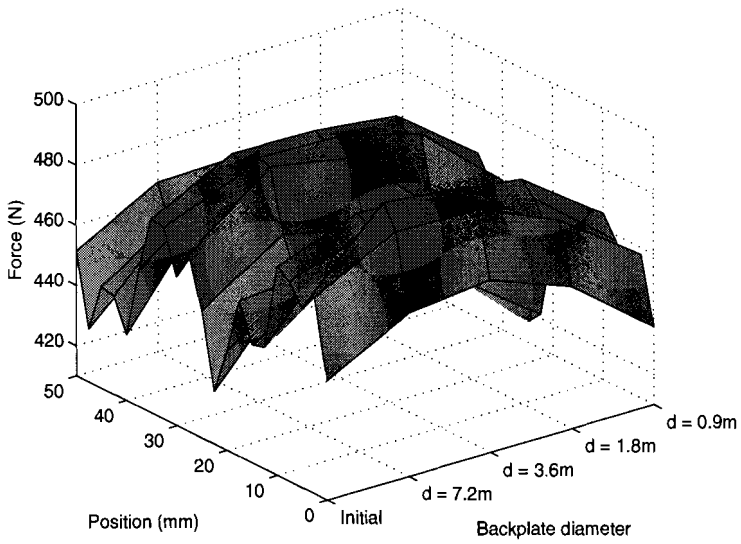

Figure 5.25: Nominal propulsion force as a function of position for different diameters of the circular curved backplate and the initial model in a 3D-view.

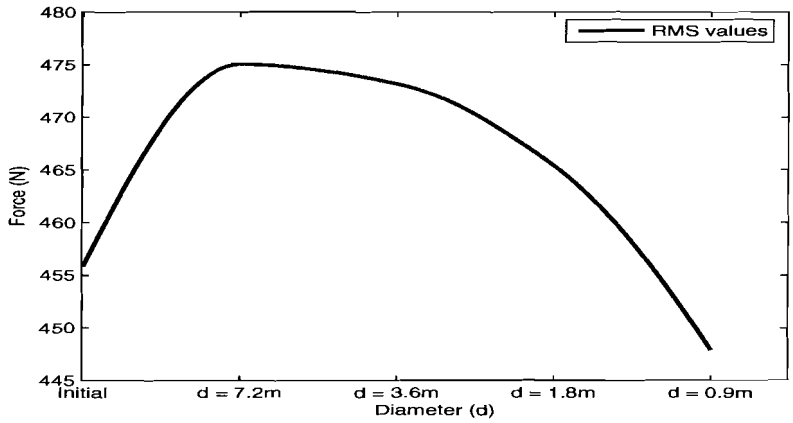

Figure 5.26: Nominal propulsion force as a function of diameter.

Chapter 6

Analysis of Flux Density Distribution

The most reasonable explanation to revise the increase of the propulsion force for the 7,2 m, 3,6 m and 1,8 m diameter model and the decrease for the 0,9 m diameter model, discussed in Chapter 5, in comparison with the initial model is to compare the airgap flux density distribution for all the used models. The results of the airgap flux densities and the comparison between them are discussed in this chapter.

6.1 Positions of airgap measurements

Because it is necessary to know the distribution of the flux density over the entire length of the mover and over the depth (or stack length) of the mover, different places in the airgap are chosen to obtain a good measurement. The actuator consists of a 2 mm airgap, where the measurement is taken in the middle of it and over the entire length of the mover. This measurement is done at three different places in the depth of the airgap. These positions are illustrated for the 0,9 m diameter model in Fig. 6.1 where the „*Inner Edge*" is at the inside of the circular curved diameter and the „*Outer Edge*" at the outside of the circular curved diameter. These positions are the same for all the circular curved diameters and the initial model.

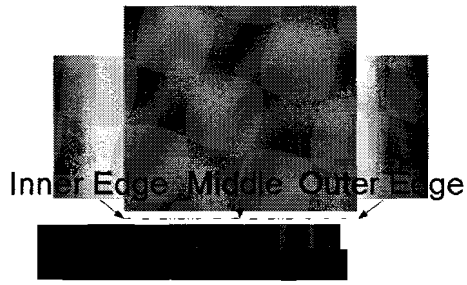

Figure 6.1: Positions of the airgap flux density measurements.

Table 6.1: RMS values of the airgap flux densities of the initial ICLPMA model at starting position.

	Initial	$d = 7.2$ m	$d = 3.6$ m	$d = 1.8$ m	$d = 0.9$ m
Fx	449,56 N	464,07 N	467,20 N	456,99 N	435,88 N

The flux densities are measured at the initial position of the mover, with the R-phase directly above a S-pole magnet and the current system described in (3.10), where x is zero and $\hat{i}$ the peak value of the nominal current. The positions of the phase teeth of the mover are illustrated in Fig. 6.2. These positions are the same for all models discussed in this chapter.
To compare the flux densities in the airgap with the generated force of the actuator, the force generated at the starting position is necessary. The forces generated at the starting position are given in Table. 6.1.

6.2 Flux distribution of the initial model

Since the geometry of the initial model presented in Fig. 1.2 is symmetric, the flux density at the inner edge and the outer edge are the same. The result of the flux density distribution at both edges of the mover obtained by FEM is presented in Fig. 6.2. The flux density at the middle of the mover will be higher then at the edges of the mover and is presented in Fig. 6.3. To evaluate the flux densities in the airgap, the effective value (RMS) of the flux densities is calculated over the entire length of the mover. The RMS values give an idea of the changes in the airgap flux densities when the geometry is changed and are used to find the cause of the force changes. The RMS values of the flux densities are given in Table. 6.2. The difference between the inner and the outer edge is caused by the numerical error of the FEM. The flux density in the ICLPMA can be seen in Appendix E

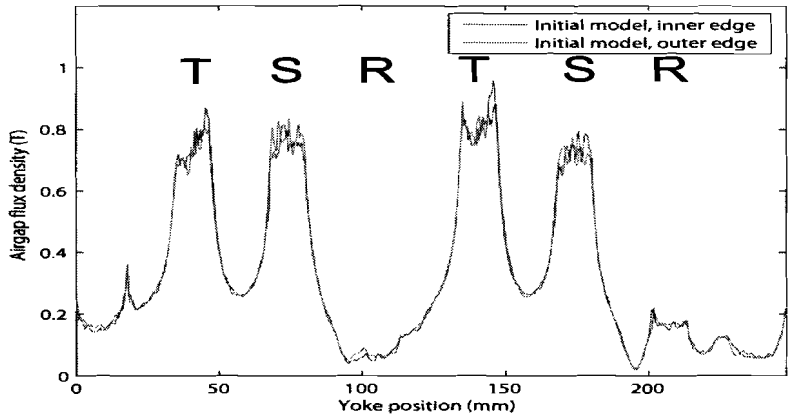

Figure 6.2: Airgap flux density at both edges of the initial ICLPMA model.

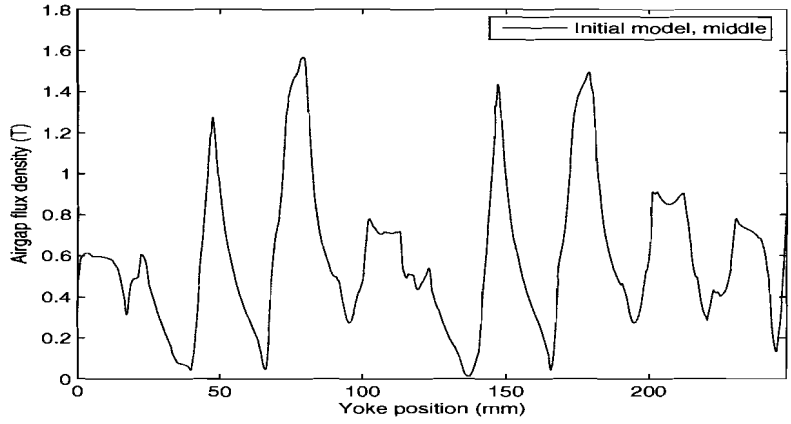

Figure 6.3: Airgap flux density at the middle of the initial ICLPMA model.

6.3 Flux density distribution of the 7,2 m diameter model

The same analysis for the initial model is done for the 7,2 m diameter model. The distribution of the flux density over the length of the yoke at the two edges and at the starting position are presented in Fig. 6.4. It can be seen that the flux density at the inner edge is increased in comparison with the flux density of the initial model. The increase of flux density is caused by the deflection of the mover and the circular curved backplate. The flux density in the airgap at the middle of the mover of the 7,2 m diameter model is presented in Fig. 6.5. The RMS values over the length of the mover are calculated and given in Table. 6.3. The RMS value at the inner edge and in the middle of

Table 6.2: RMS values of the airgap flux densities of the initial ICLPMA model.

Airgap position	RMS value (T)
Inner edge	0,1960
Middle	0,7979
Outer edge	0,2233

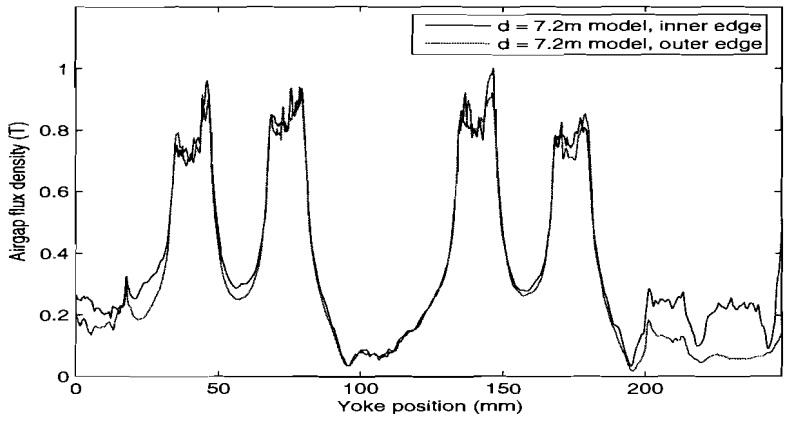

Figure 6.4: Airgap flux density at both edges of the 7,2 m diameter ICLPMA model.

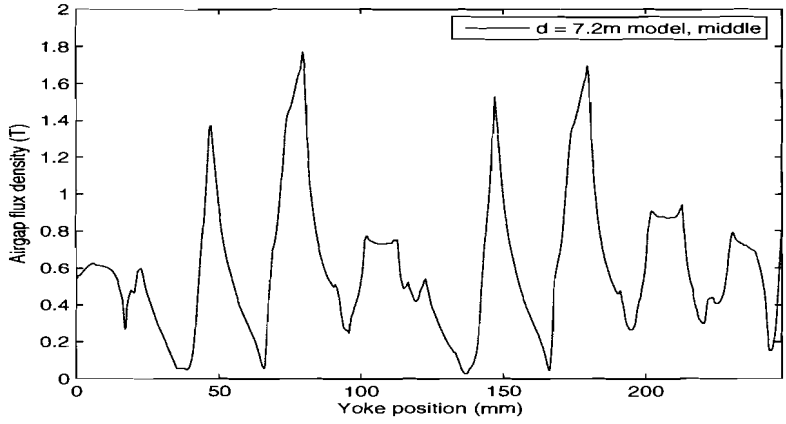

Figure 6.5: Airgap flux density at the middle of the mover of the 7,2 m diameter ICLPMA model.

the mover are increased in comparison with the initial model. The RMS value at the outer edge is decreased, which is caused by the deflection of the mover and the curved backplate. As expected, the flux density concentrates more to

Table 6.3: RMS values of the airgap flux densities of the 7,2 m diameter ICLPMA model.

Airgap position	RMS value (T)
Inner edge	0,4830
Middle	0,8270
Outer edge	0,1397

the inside of the circular curved backplate. The flux density at the inner edge shows a higher increase then the decrease of the outer edge. The flux density in the ICLPMA can be seen in Appendix E. This increase and the increase at the middle of the airgap will cause an overall increase of the flux density in the airgap. This increase of flux density will cause the increase of force in comparison with the initial model.

6.4 Flux density distribution of the 3,6 m diameter model

After the 7,2 m diameter model the 3,6 m diameter model is analyzed with the FEM. The flux densities in the airgap at the edges of the mover of the 3,6 m diameter model obtained by the FEM are presented in Fig. 6.6. It can be seen

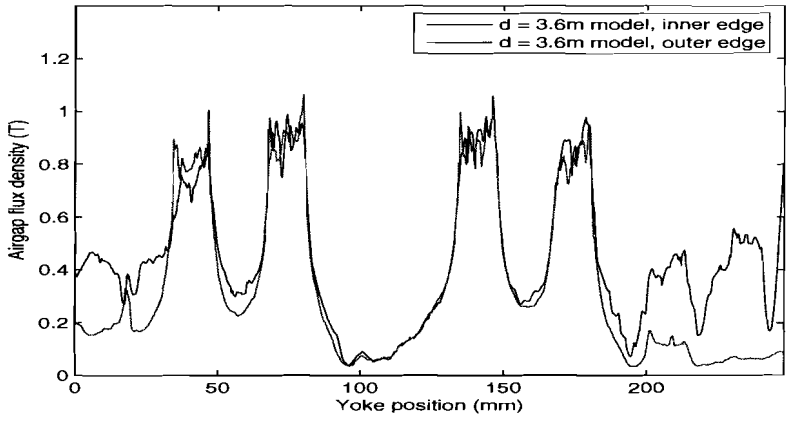

Figure 6.6: Airgap flux density at both edges of the 3,6 m diameter ICLPMA model.

that the flux density at the outer edge is decreased at the ends of the mover and will cause a decrease in RMS value. The flux density in the airgap at the middle of the mover of the 3,6 m diameter model is presented in Fig. 6.7. The calculations of the RMS values of the flux densities in the airgap over the length of the mover are given in Table. 6.4. The RMS values show an increase at the inner edge and in the middle, when compared with the initial model and the

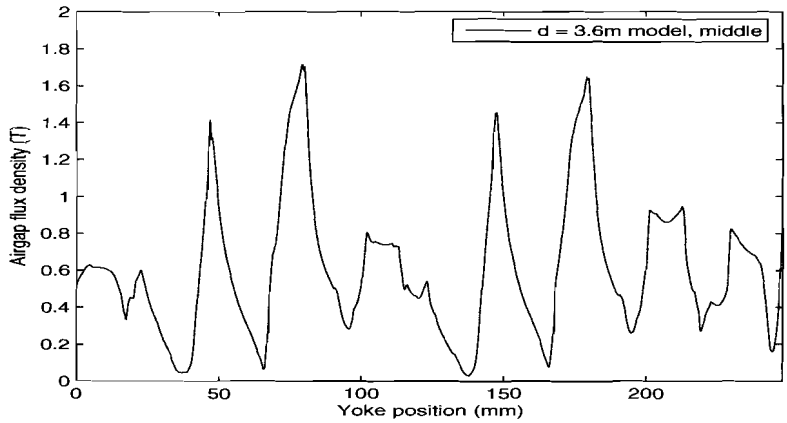

Figure 6.7: Airgap flux density at the middle of the mover of the 3,6 m diameter ICLPMA model.

Table 6.4: RMS values of the airgap flux densities of the 3,6 m diameter ICLPMA model.

Airgap position	RMS value (T)
Inner edge	0,8327
Middle	0,8456
Outer edge	0,0802

7,2 m diameter model. The outer edge is also decreased in comparison with the previous models. Since the increase at the inner edge and at the middle of the airgap still cause an overall increase of flux density in the airgap in comparison with the initial model, it will cause the increase of force in comparison with the initial model and the 7,2 m diameter model. The flux density in the ICLPMA can be seen in Appendix E.

6.5 Flux density distribution of the 1,8 m diameter model

After the 7,2 m diameter model and the 3,6 m diameter model the 1,8 m diameter model is analyzed with the FEM. The flux densities in the airgap at the edges of the mover of the 1,8 m diameter model obtained by analysis are presented in Fig. 6.8. The flux density in the airgap at the middle of the mover of

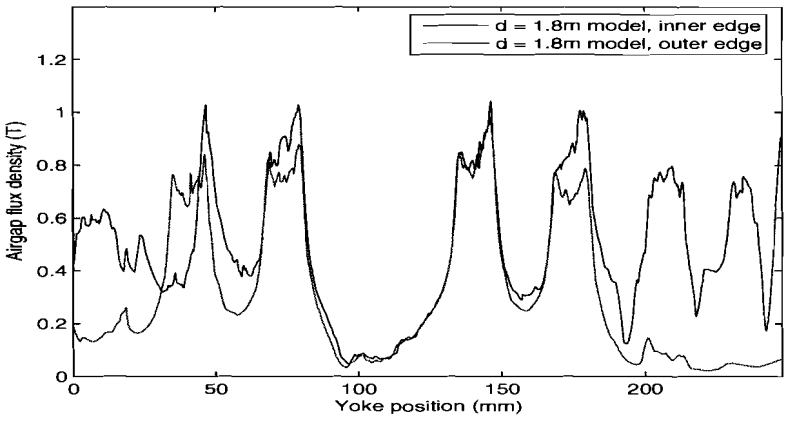

Figure 6.8: Airgap flux density at both edges of the 1,8 m diameter ICLPMA model.

the 1,8 m diameter model is presented in Fig. 6.9. The calculations of the RMS

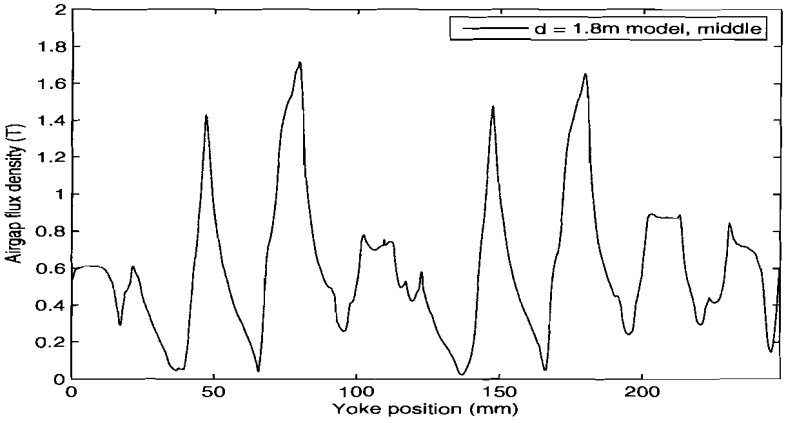

Figure 6.9: Airgap flux density at the middle of the mover of the 1,8 m diameter ICLPMA model.

values of the flux densities in the airgap over the length of the mover are given in Table. 6.5. It can be seen that the flux density in the middle of the airgap

Table 6.5: RMS values of the airgap flux densities of the 1,8 m diameter ICLPMA model.

Airgap position	RMS value (T)
Inner edge	0,8874
Middle	0,6322
Outer edge	0,0647

and at the outer edge of the airgap are decreased, the flux density at the inner edge is still increasing in comparison with the previous models. The decrease of the flux density at the middle is caused by the increase of the deflection between the backplate and the mover. The decrease of the flux density at the middle of the mover will cause an overall decrease of the flux density in the airgap, in comparison with the previous curved diameters but still an increase in comparison with the initial model. This will cause the decrease of force in comparison with the previous curved diameter models but still an increase of force in comparison with the initial model. The flux density in the ICLPMA can be seen in Appendix E.

6.6 Flux density distribution of the 0,9 m diameter model

The 0,9 m diameter model is analyzed the same as the previous models. The flux densities in the airgap at the edges of the mover obtained by FEM is presented in Fig. 6.10. The flux density in the airgap at the middle of the mover of the

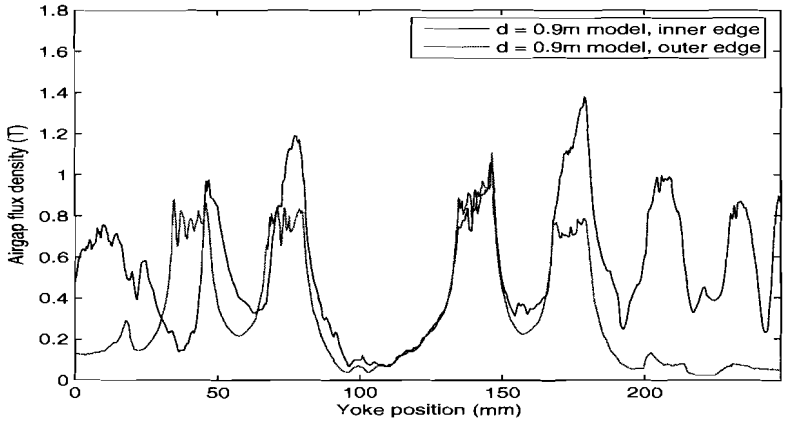

Figure 6.10: Airgap flux density at both edges of the 0,9 m diameter ICLPMA model.

0,9 m diameter model is presented in Fig. 6.11. The calculations of the RMS values of the flux densities in the airgap over the length of the mover are given in

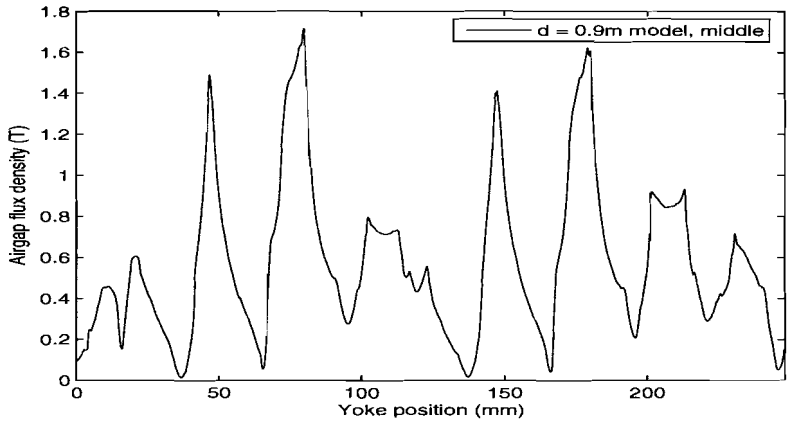

Figure 6.11: Airgap flux density at the middle of the mover of the 0,9 m diameter ICLPMA model.

Table 6.6: RMS values of the airgap flux densities of the 0,9 m diameter ICLPMA model.

Airgap position	RMS value (T)
Inner edge	0,8663
Middle	0,1487
Outer edge	0,0520

Table. 6.6. It can be seen that the large decrease of the flux density in the airgap at the middle of the mover, the overall flux density in the airgap is decreased in comparison with all the previous models and therefore the decrease in force in comparison with the previous models. The flux density in the ICLPMA can be seen in Appendix E.

6.7 Conclusion

When the diameter of the circular curved iron backplate decreases, the distance between the magnets at the inside of the circular curved backplate will decrease and increase at the outside. This will cause an increase of flux density at the inside of the circular curved backplate and therefore an increase of flux density at the inner edge of the mover, which can be seen at the 7, 2 m diameter and 3, 6 m diameter model. When the diameter is decreased until the middle of the mover is deflected so far that it reaches the area where the flux density is decreases, the force will start to decrease. This can be seen with the 1, 8 m diameter model Fig. 5.13, where the middle of the mover at both ends of the yoke are deflected enough to reach over the middle line of the circular curved backplate. The 0, 9 m diameter model shows an even more deflection, (Fig. 5.17), where the middle of the mover at both ends of the yoke reach the outer edge of the circular curved backplate. The RMS values of the flux density results confirm this and therefore give a good indication of the changes in the airgap flux densities. Fig. 6.12 illustrates the flux densities at both edges and in the middle of the mover as function of diameter. It can be seen that the flux density in the middle begins to decrease at the same point as the force begins to degrease. The high increase at the inner edge, for the first two diameters, and the increase at the middle of the mover describe the force increase of these diameters. The flux densities are

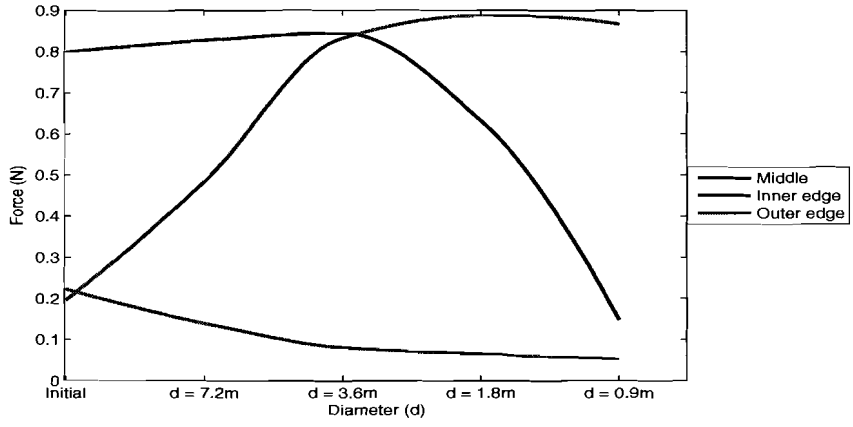

Figure 6.12: Airgap flux density at both edges and at the middle of the mover for all diameters and the initial model.

presented in Appendix E, the iron at the inner edge of the mover becomes more and more saturated as the diameter decreases and the flux density at the outer edge of the mover decreases. Further investigation of the flux density change in the yoke of the mover and the harmonic spectrum of the airgap flux density could explain this more accurate. This is not investigated because of the time limit for this project.

Chapter 7

Conclusions and recommendations

7.1 Conclusions

This thesis describes the result of a research of the influence of geometry variations in the iron backplate of an iron core linear permanent magnet actuator on the electromagnetic performance and a comparison of the two FEM software packages. The ILLPMA discussed in Chapter 2 is used to compare the two FEM software packages, Maxwell 3D from Ansoft Co. and Multiphysics from Comsol Inc. The difference between the calculations of the two packages are described and a recommendation for the software users is made.
Maxwell 3D (Ansoft Co.) is used in this project due to the specific electromagnetic problems originated in the project and the fact that the University of Technology Eindhoven uses this FEM software package. A 3D representation of a standard ICLPMA from Tecnotion B.V. is introduced as initial model and analyzed by the FEM for nominal propulsion force, cogging force, back-emf and inductance. The propulsion force is also analyzed for a range of different currents and different phase shifts of the current. The cogging force is separated into two components by the analysis of the initial model without the end teeth. The results obtained by the FEM analysis in Chapter 4 are used as a benchmark for further analysis of the geometry of the ICLPMA. A MEC model of the ICLPMA is used to verify the results obtained by the FEM. Four different circular curved iron backplates with the same mover as the initial model are introduced and analyzed with the FEM for propulsion force at nominal current and for cogging force. The results are compared with the propulsion force and cogging force of the initial model. By FEM analysis it is possible to give a quantified estimation for the different force components. Meanwhile, the qualitative analysis and treatment of the physical phenomena request a creation of the extended analytical tools with intermediate steps of estimation of different electromagnetic variables which are greatly influencing the performance characteristics of the ICLPMA.

Particularly, during design procedure of any electrical machine it is of highest importance to get the extended information about distribution of the flux density in the airgap. The flux density distribution in the airgap is analyzed and a good agreement is been found between the force change and the flux density change in the airgap.

7.2 Recommendations

- By designing an extended MEC model which considers the curved iron backplate it is possible to investigate the various magnetic quantities which are influencing the performance characteristics of the ICLPMA.
- All FEM analyses in this thesis are static, which means that dynamic properties are not investigated. These dynamic properties must be investigated by means of transient analysis.
- The flux density distribution in the airgap is built up out of a harmonic spectrum. This spectrum is mainly caused by the slotted structure of the mover and additionally influenced by the introduction of the circular curved geometry of the iron backplate. Selection of proper number of slots per pole per phase could be an additional topic for the research.

References

[1] H., Polinder and J.G., Slootweg, M.J., Hoeijmakers, J.C., Compter MODELING OF LINEAR PM MACHINE INCLUDING MAGNETIC SATURATION AND END EFFECTS: MAXIMUM FORCE-TO-CURRENT RATIO, *IEEE Trans. Magn.*, Vol. 39, No. 6, pp. 1681-1688, Nov./Dec. 2003.

[2] S. Vaez-Zadeh and A.H. Isfahani. ENHANCED MODELING OF LINEAR PERMANENT-MAGNET SYNCHRONOUS MOTOR, *IEEE Trans. Magn.*, Vol. 43, No. 1, pp. 33-39, Jan. 2007.

[3] Y.M. Chen and S.Y. Fan, W.S Lu. PERFORMANCE ANALYSIS OF LINEAR PERMANENT MAGNET MOTORS FOR OPTIMAL DESIGN CONSIDERATIONS, *Applied Power Electronics Conference and Exposition, 2004. APEC '04. Nineteenth Annual IEEE*, Vol. 3, pp. 1584-1589, 2004.

[4] G.H. Kang and J.P. Hong, G.T Kim. A NOVEL DESIGN OF AN AIR-CORE TYPE PERMANENT MAGNET LINEAR BRUSLESS MOTOR BY SPACE HARMONICS FIELD ANALYSIS, *IEEE Trans. Magn.*, Vol. 37, No. 5, pp. 3732-3736, Sep. 2001.

[5] J. Cale and S.D. Sudhoff, L.Q Tan. ACCURATELY MODELING EI CORE INDUCTORS USING A HIGH-FIDELITY MAGNETIC EQUIVALENT CIRCUIT APPROACH, *IEEE Trans. Magn.*, Vol. 42, No. 1, pp. 40-46, Jan. 2006.

[6] O. Ustun and R.N. Tuncay. DESIGN, ANALYSIS AND CONTROL OF A NOVEL LINEAR ACTUATOR, *IEEE Trans. Ind. Applicat.*, Vol. 42, No. 4, pp. 1007-1013, Jul./Aug. 2006.

[7] Ansoft, Co. Maxwell 2D and 3D. *http://www.ansoft.com.* n.a. Pittsburgh, PA 15219, USA.

[8] Comsol, Inc. Multiphysics. *http://www.comsol.com.* n.a. Burlington, MA 01803, New England.

[9] C.A.R., Eijnden v.d. and C.J.G., Spoorenberg. ELEKTRISCHE NETWERKEN. Nijgh & Van Ditmar, 1999. ISBN 90-236-4041-1.

[10] M.A.J., Op 'tRoodt. ELEKTRICITEIT, ELEKTRISCHE MACHINES. 1992. ISBN 90-306-2022-6.

[11] J. Gieras and M.Wing. PERMANENT MAGNET ACTUATOR TECHNOLOGY. Marcel Dekker, second edition, 2002. ISBN 0-8247-0739-7.

[12] J.F. Gieras and Z.J. Piech. LINEAR SYNCHRONOUS MOTORS, TRANSPORTATION AND AUTOMATION SYSTEMS, volume 1. CRC Press, 2000. ISBN 0-8493-1859-9.

[13] F.B.M. Hork v. A TREATISE ON MAGNETICS & POWER ELECTRONICS. (Syllabus), TU/e Eindhoven, 2005.

Appendix A

Flowchart MEC models.

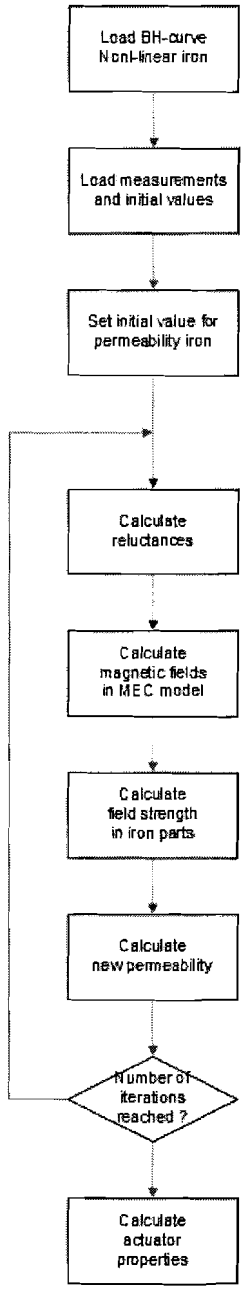

Figure A.1: Flowchart of MEC models used to calculate the properties of the ILLPMA and the ICLPMA.

Appendix B

ILLPMA Dimensions.

The values are for the alignment of the coil and the magnets, values are in (mm).

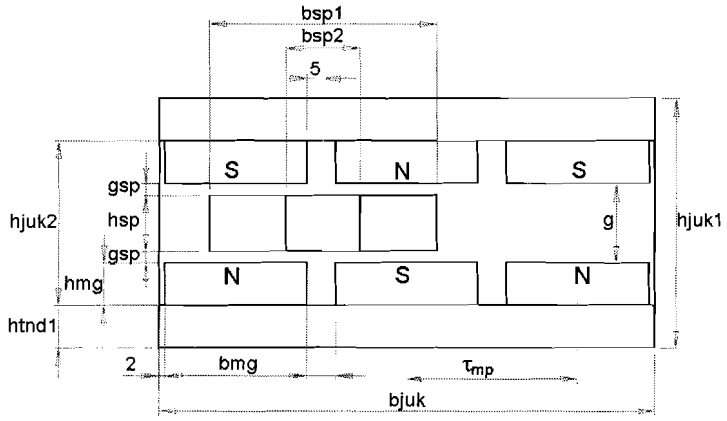

Figure B.1: Definition of ILLPMA dimensions, front view.

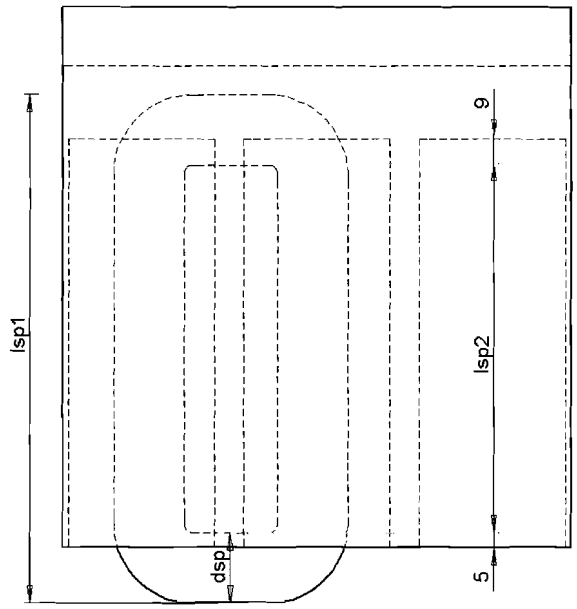

Figure B.2: Definition of ILLPMA dimensions, top view.

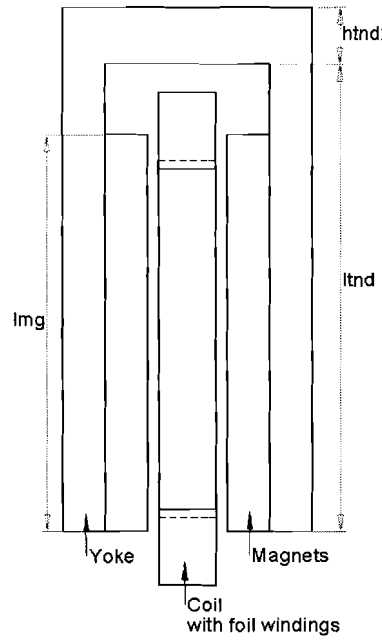

Figure B.3: Definition of ILLPMA dimensions, side view.

Appendix C

ICLPMA Dimensions.

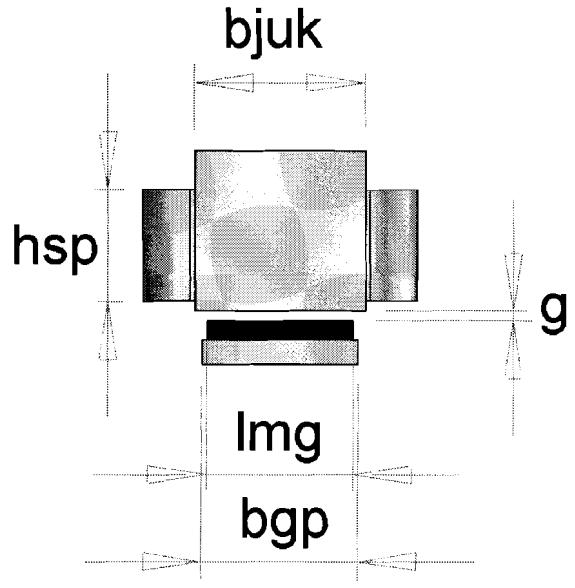

Figure C.1: Definition of ICLPMA dimensions, front view.

Dimension	Value	Dimension	Value
bgp	32 mm	*hjuk*	33 mm
bjuk	35 mm	*hsp*	23 mm
bmg	30 mm	*htnd*	25 mm
*btd*1	18 mm	*iso*	1 mm
*btd*2	12 mm	*ljuk*	248 mm
g	2 mm	*slf*1	6 mm
hgp	5 mm	*slf*2	10.6666 mm

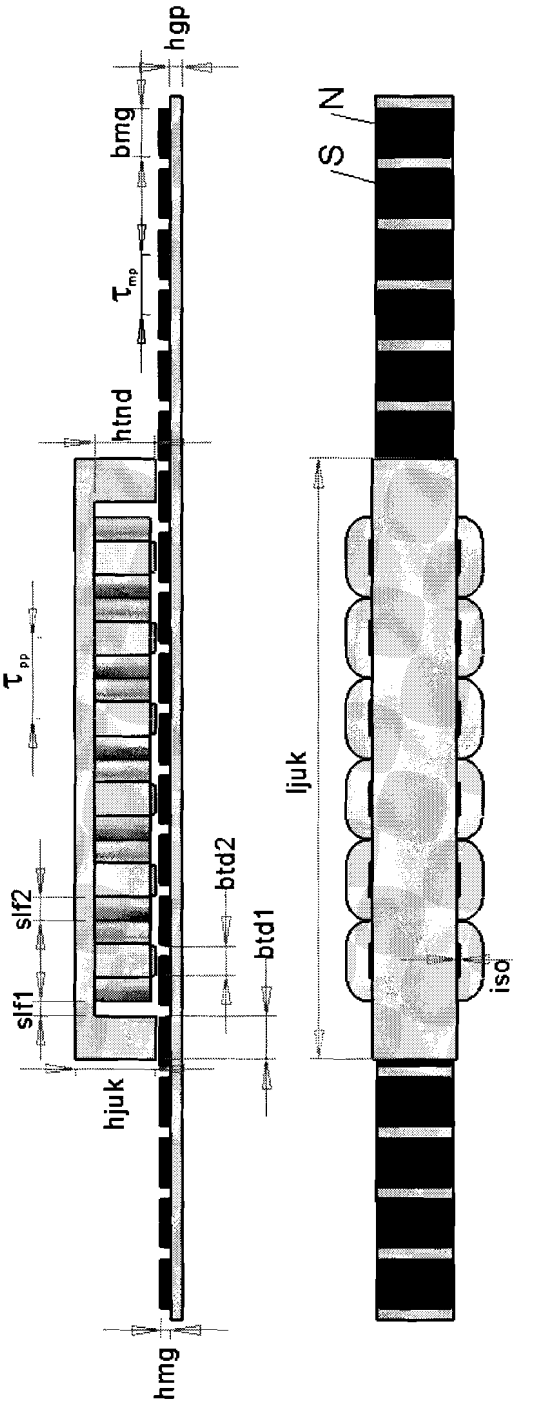

Figure C.2: Definition of ICLPMA dimensions, side view.

Appendix D

Flux Density Initial Model.

D.1 Initial Model Including End Teeth at Nominal Current.

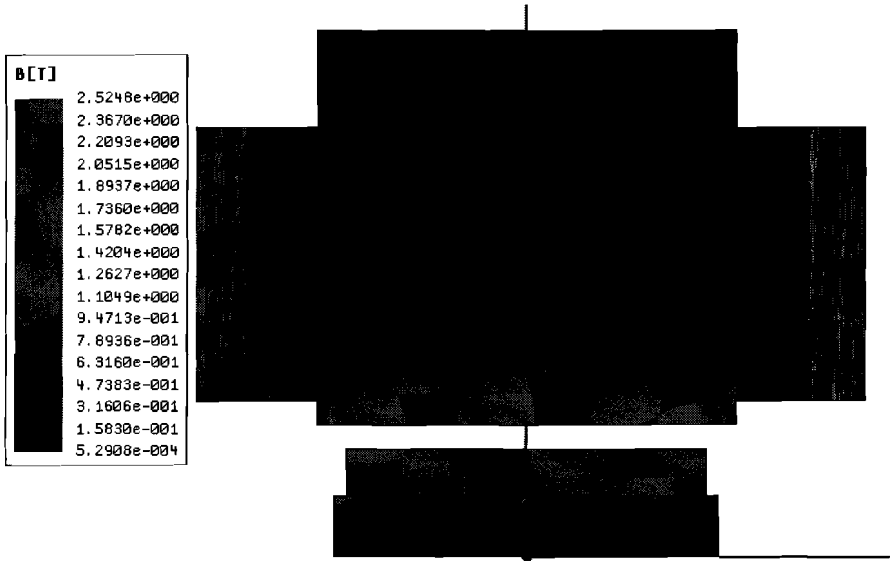

Figure D.1: Front view of flux density in the initial ICLPMA model at nominal current at starting position.

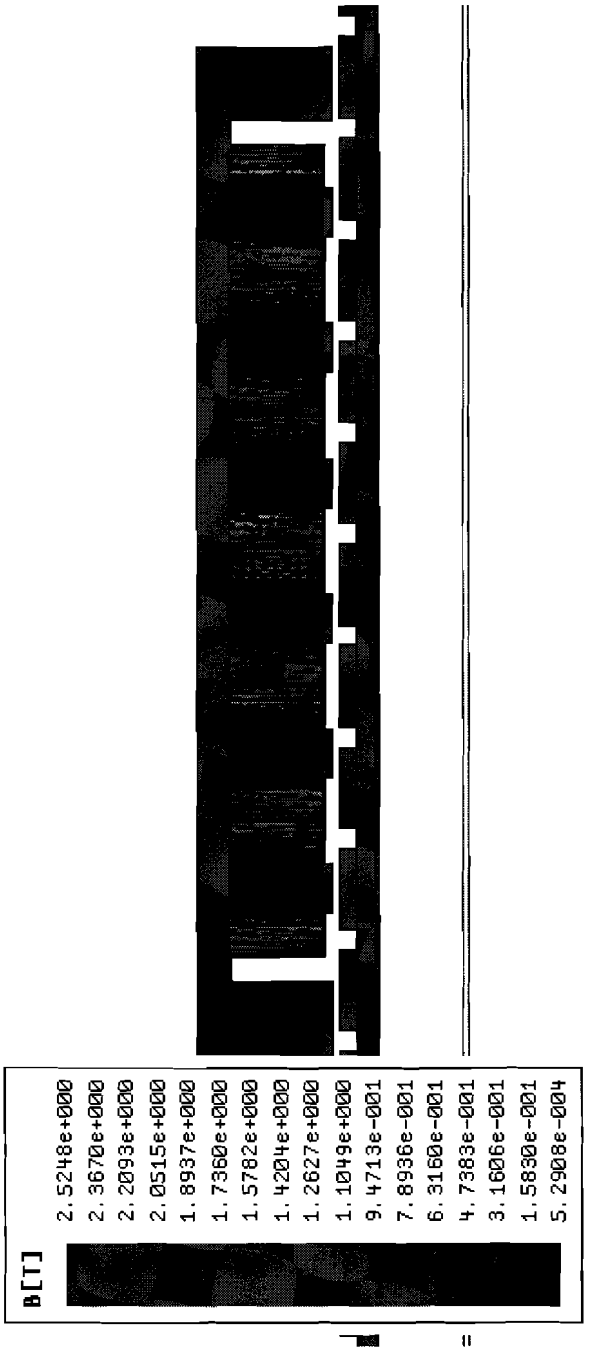

Figure D.2: Side view of flux density in the initial ICLPMA model at nominal current at starting position.

D.2 Initial Model Including End Teeth Without Current.

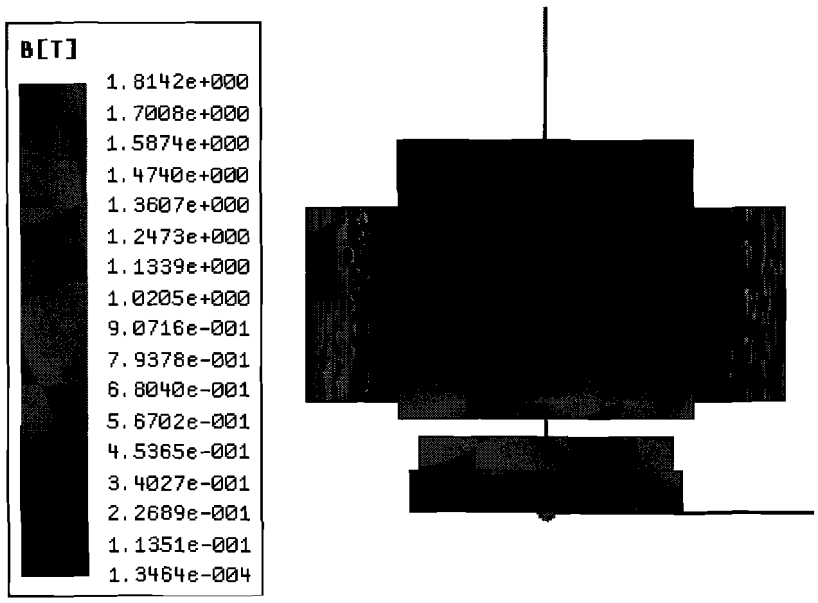

Figure D.3: Front view of flux density in the initial ICLPMA model without coil excitation at starting position.

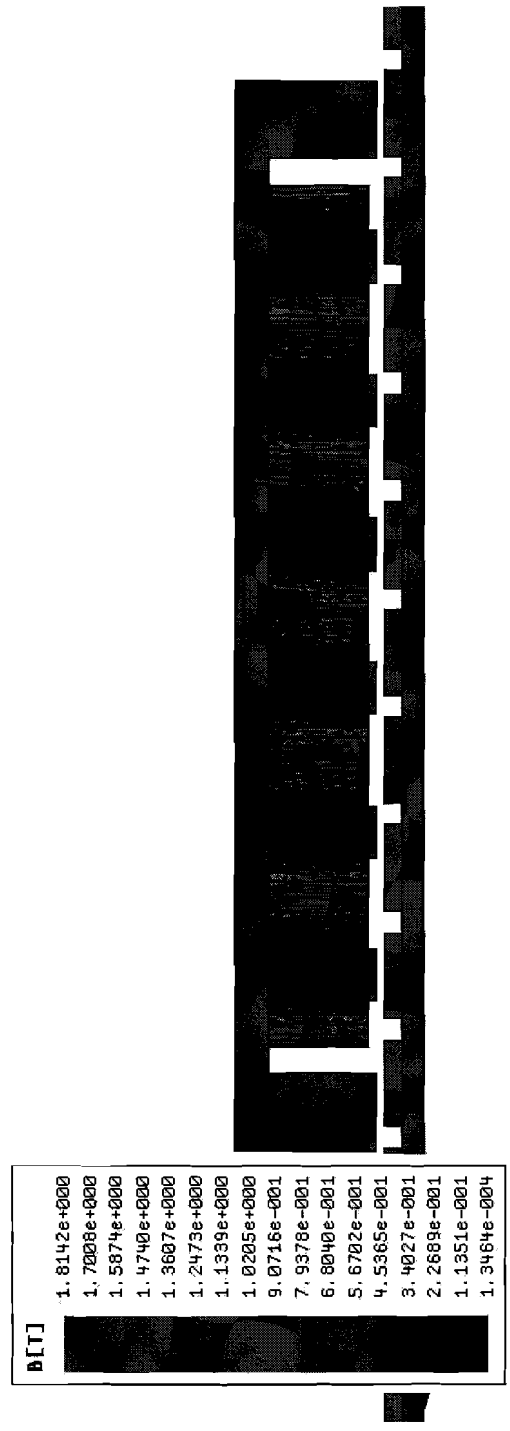

Figure D.4: Side view of flux density in the initial ICLPMA model without coil excitation at starting position.

D.3 Initial Model Neglecting End Teeth Without Current.

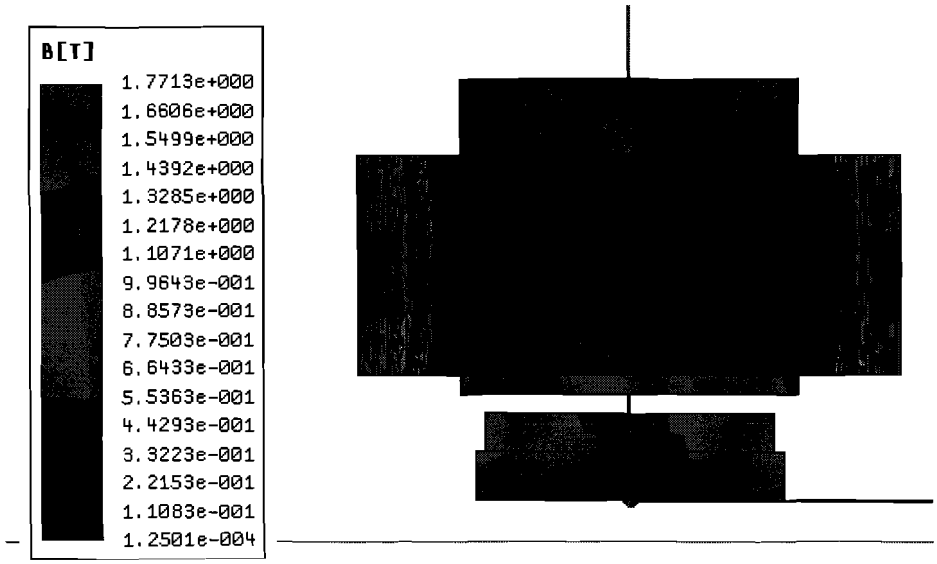

Figure D.5: Front view of flux density in the initial ICLPMA model without coil excitation and end teeth at starting position.

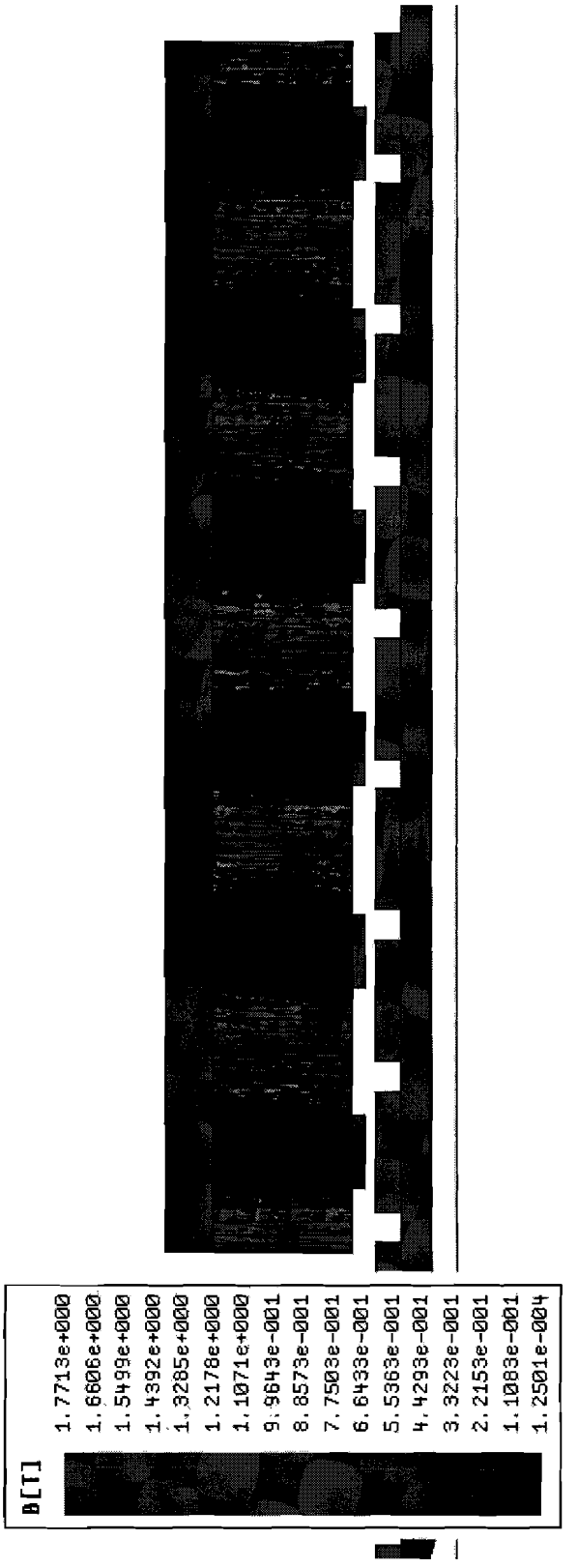

Figure D.6: Side view of flux density in the initial ICLPMA model without coil excitation and end teeth at starting position.

Appendix E

Flux Density Circular Curved Backplate Models.

E.1 Flux Density 28,8 m Diameter Model.

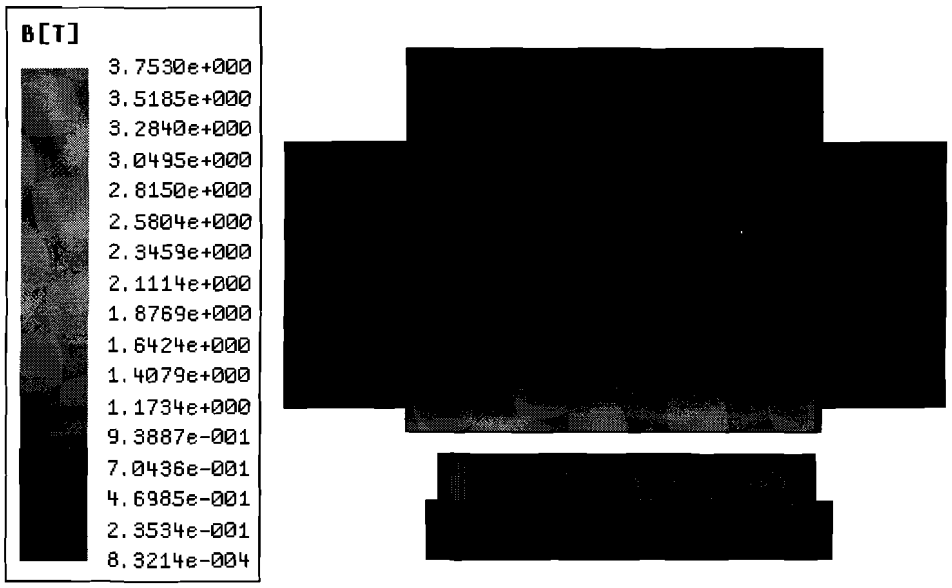

Figure E.1: Front view of flux density in the 28,8 m diameter ICLPMA model at nominal current at starting position.

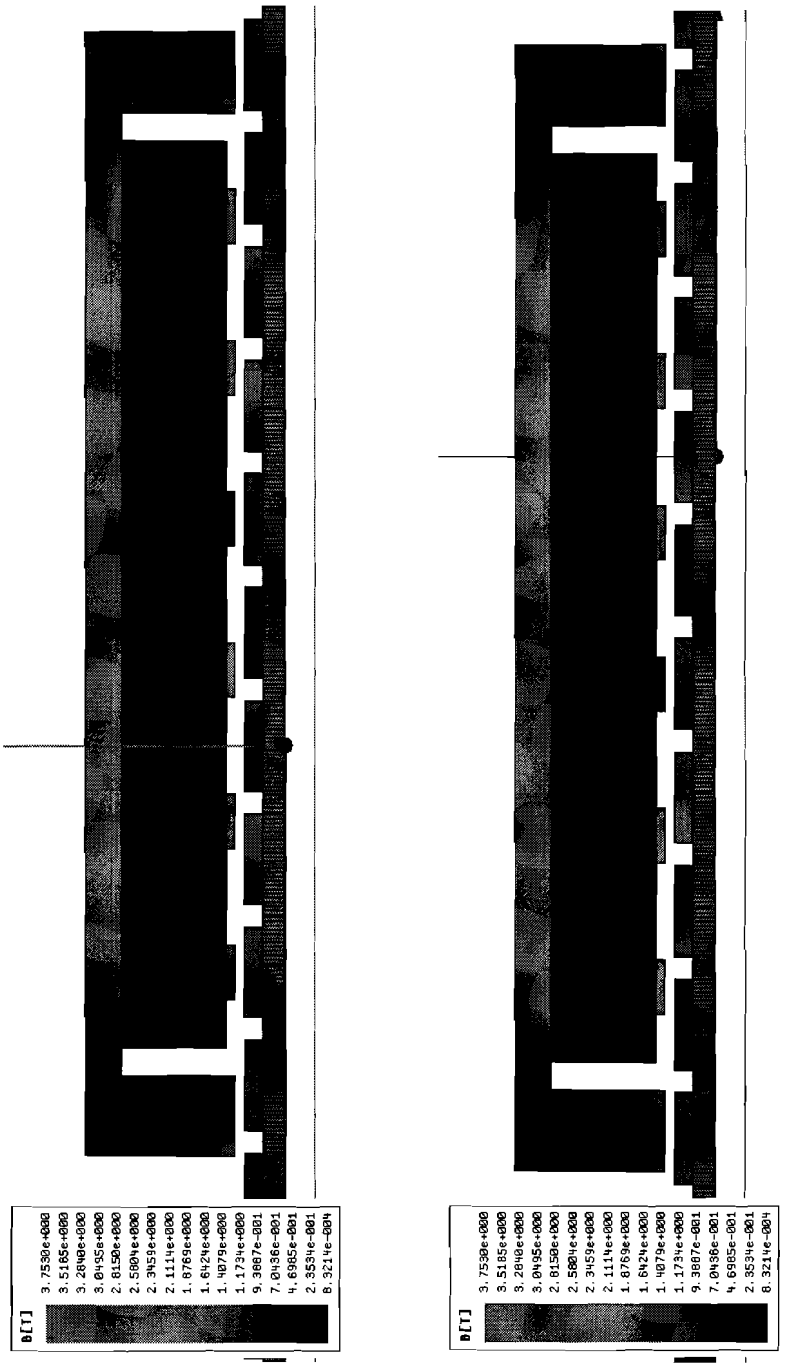

(a) (b)

Figure E.2: Side views of flux density in the 28, 8 m diameter ICLPMA model at nominal current at starting position, Inner edge side E.2(a), Outer edge side E.2(b)

E.2 Flux Density 7,2 m Diameter Model.

Figure E.3: Front view of flux density in the 7,2 m diameter ICLPMA model at nominal current at starting position.

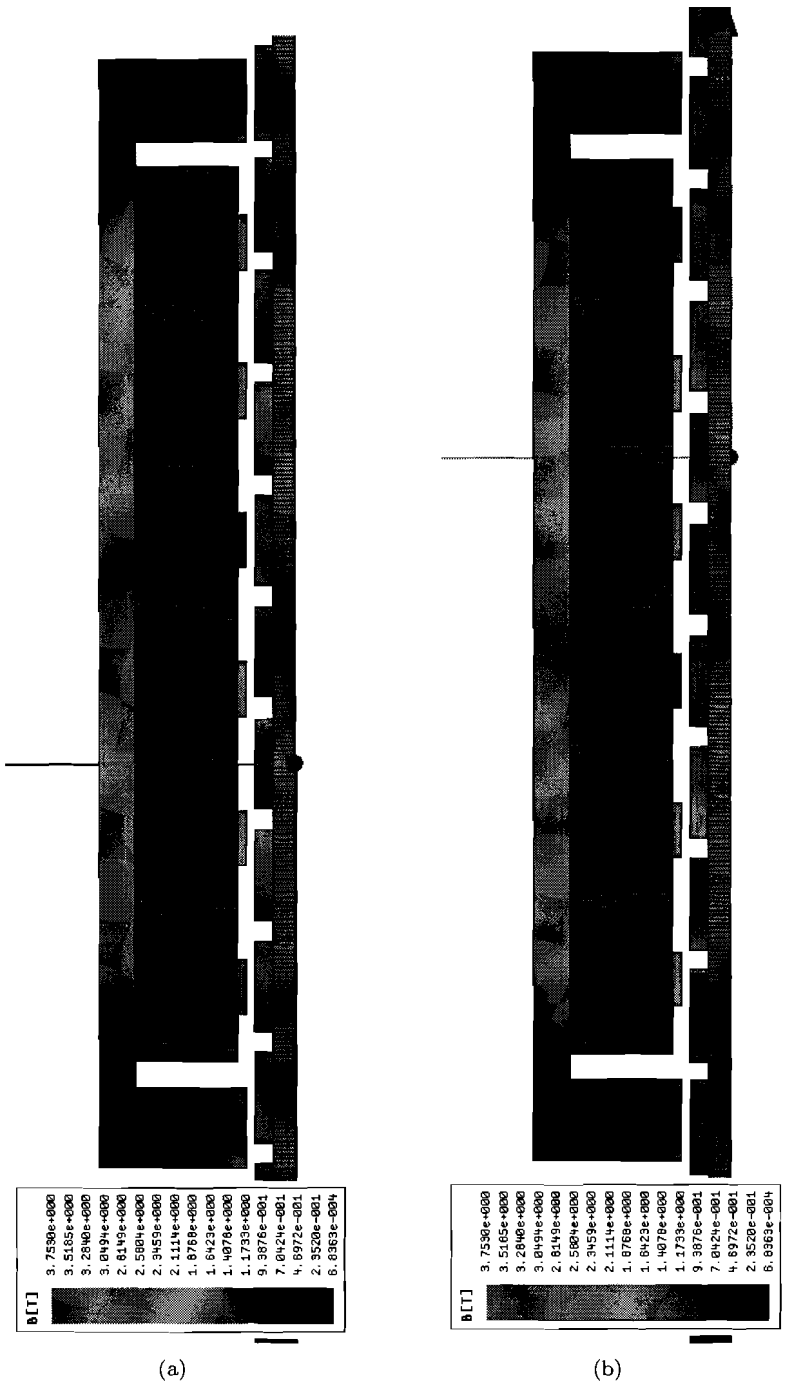

(a) (b)

Figure E.4: Side views of flux density in the 7,2 m diameter ICLPMA model at nominal current at starting position, Inner edge side E.4(a), Outer edge side E.4(b)

E.3 Flux Density 3,6 m Diameter Model.

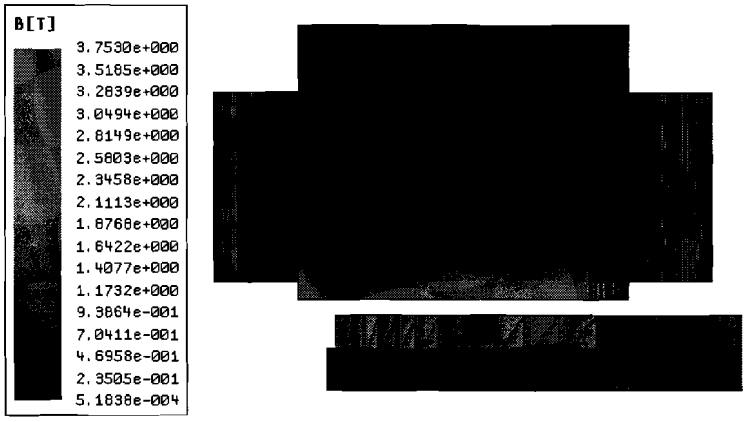

Figure E.5: Front view of flux density in the 3,6 m diameter ICLPMA model at nominal current at starting position.

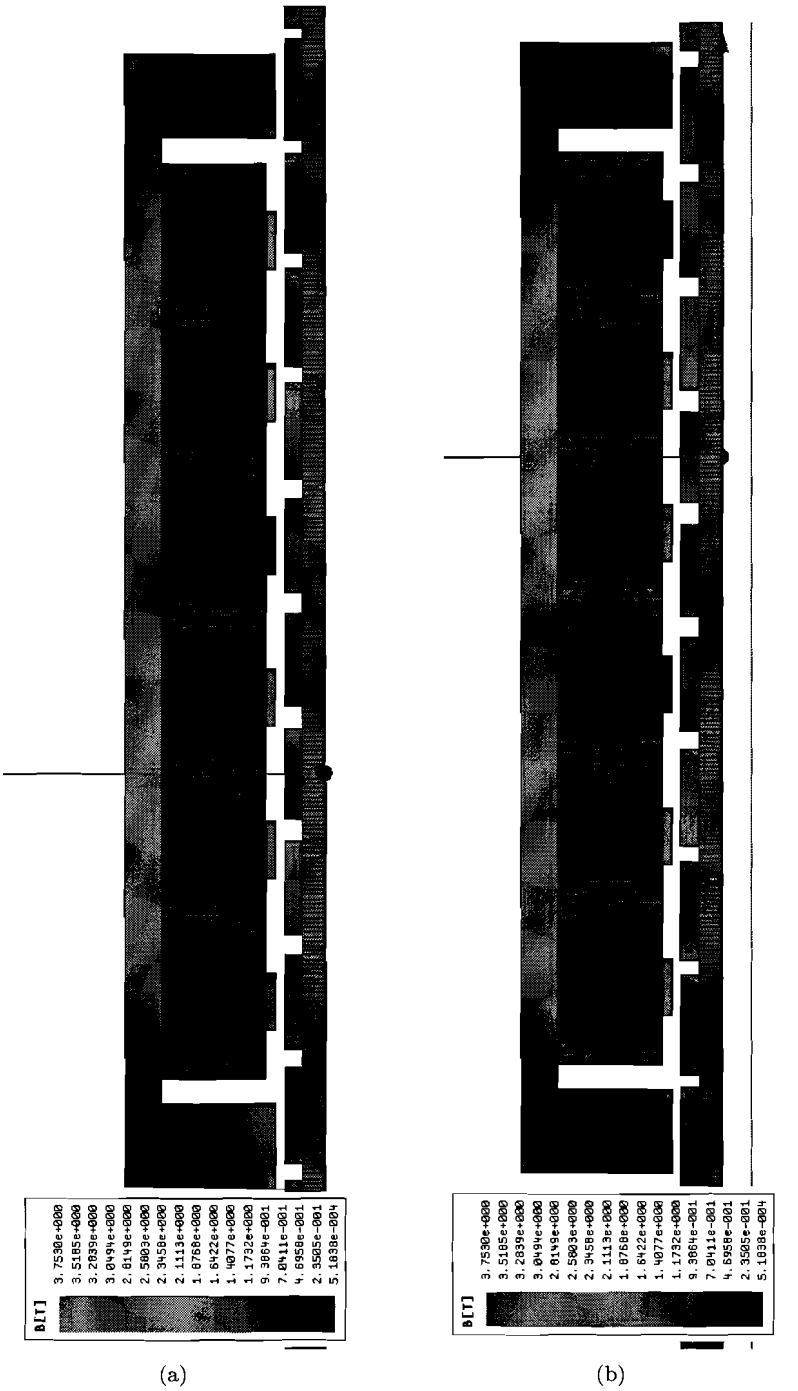

(a) (b)

Figure E.6: Side views of flux density in the 3,6 m diameter ICLPMA model at nominal current at starting position, Inner edge side E.6(a), Outer edge side E.6(b)

E.4 Flux Density 1,8 m Diameter Model.

Figure E.7: Front view of flux density in the 1,8 m diameter ICLPMA model at nominal current at starting position.

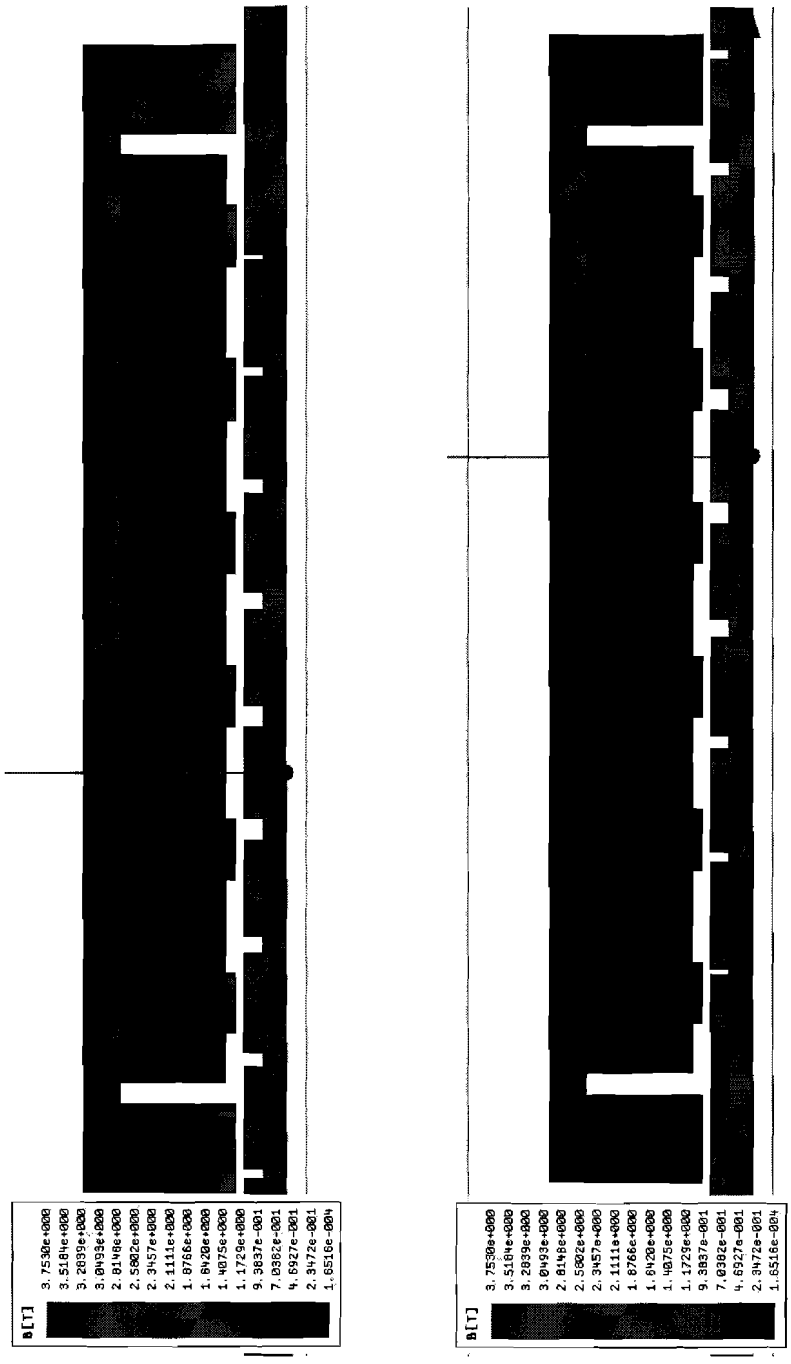

(a) (b)

Figure E.8: Side views of flux density in the 1,8 m diameter ICLPMA model at nominal current at starting position, Inner edge side E.8(a), Outer edge side E.8(b)

E.5 Flux Density 0,9 m Diameter Model.

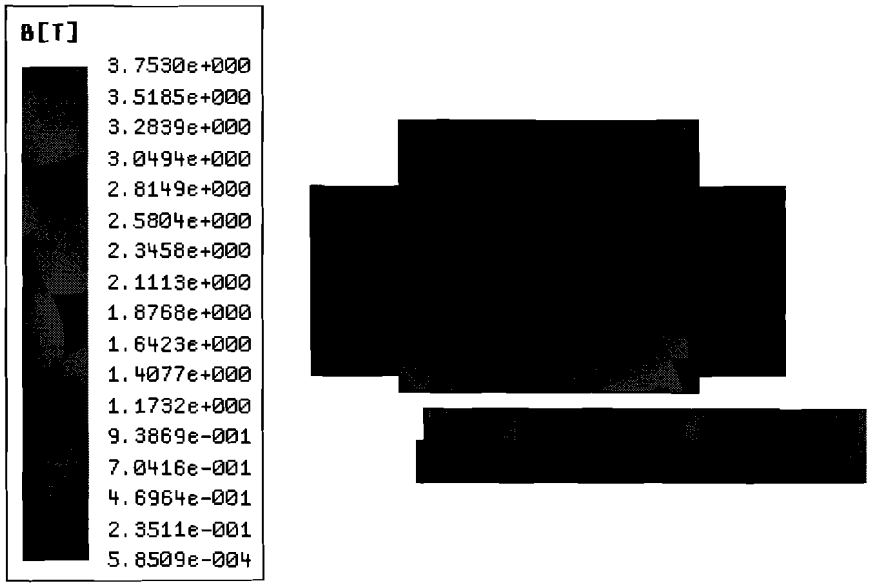

Figure E.9: Front view of flux density in the 0,9 m diameter ICLPMA model at nominal current at starting position.

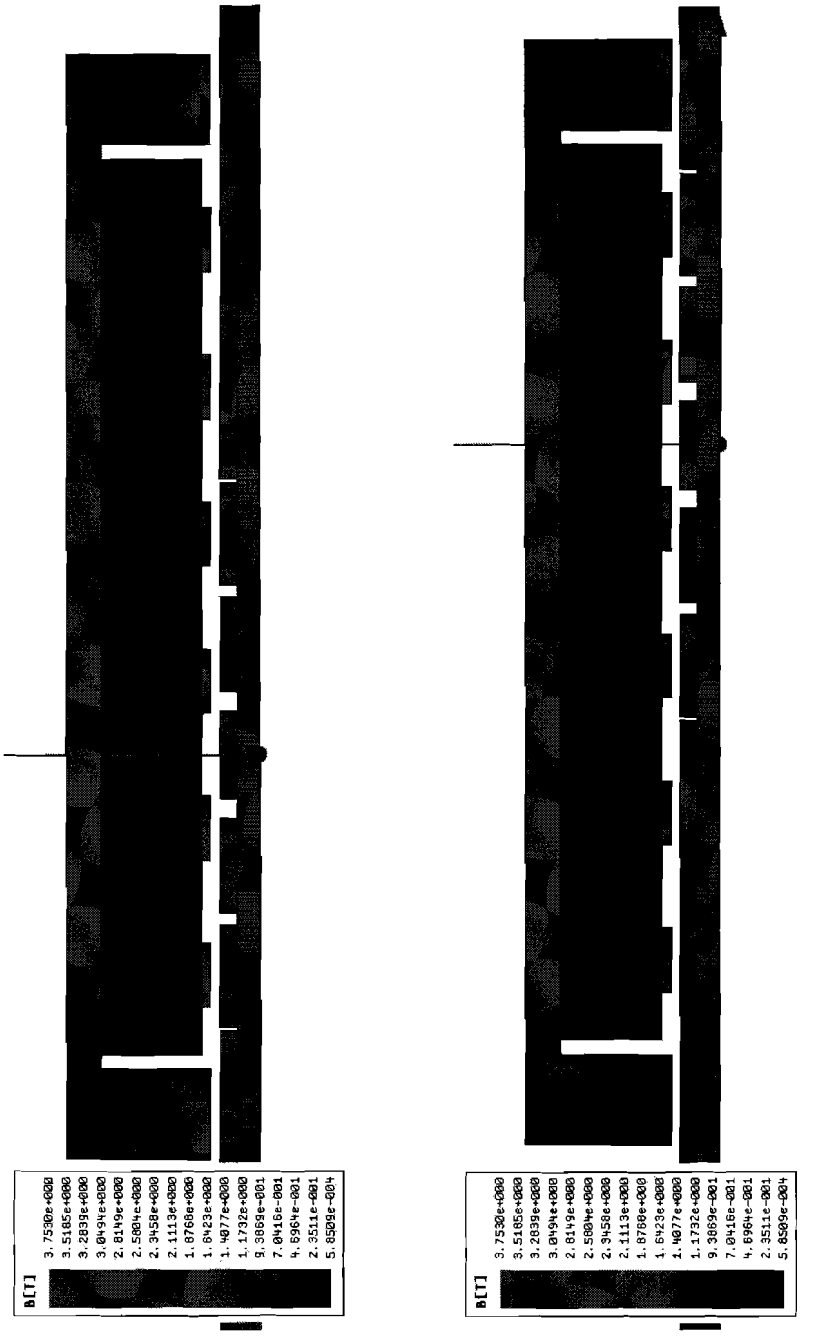

(a) (b)

Figure E.10: Side views of flux density in the 0,9 m diameter ICLPMA model at nominal current at starting position, Inner edge side E.10(a), Outer edge side E.10(b)